SOLID-STATE NANOPORE SENSORS FOR NUCLEIC ACID ANALYSIS

BY

BALA MURALI KRISHNA VENKATESAN

DISSERTATION

Submitted in partial fulfillment of the requirements
for the degree of Doctor of Philosophy in Electrical and Computer Engineering
in the Graduate College of the
University of Illinois at Urbana-Champaign, 2011

Urbana, Illinois

Doctoral Committee:

Professor Rashid Bashir, Chair
Professor Joseph Lyding
Assistant Professor Eric Pop
Assistant Professor Oleksii Aksimentiev

Abstract

Nanopore DNA analysis is an emerging technique that involves electrophoretically driving DNA molecules through a nano-scale pore in solution and monitoring the corresponding change in ionic pore current. This versatile approach permits the label-free, amplification-free analysis of charged polymers (single stranded DNA, double stranded DNA and RNA) ranging in length from single nucleotides to kilobase long genomic DNA fragments with subnanometer resolution. Recent advances in nanopores suggest that this low-cost, highly scalable technology could lend itself to the development of third generation DNA sequencing technologies, promising rapid and reliable sequencing of the human diploid genome for under $1000.

Here, we report the development of versatile, nano-manufactured Al_2O_3 solid-state nanopores and nanopore arrays for rapid, label-free, single-molecule detection and analysis of DNA and protein. This nano-scale technology has proven to be reliable, affordable, and mass producible, and allows for integration with VLSI processes. A detailed characterization of nanopore performance in terms of electrical noise, mechanical robustness and materials analysis is provided, and the functionality of this technology in experimental DNA biophysics is explored. A framework for the application of this technology to medical diagnostics and sequencing is also presented. Specifically, studies involved the detection of DNA-protein complexes, a viable strategy in screening methylation patterns in panels of genes for early cancer detection, and the creation of lipid bilayer coated nanopore sensors, useful in creating hybrid biological/solid-state nanopores for DNA sequencing applications.

The concept of a gated nanopore is also presented with preliminary results. The fabrication of this novel system has been enabled by the recent discovery of graphene, a highly versatile material with remarkable electrical and mechanical properties. Direct modulation of the nanopore conductance was observed through the application of potentials to the graphene gate. These exciting results suggest this technology could potentially be useful in slowing down or trapping a DNA molecule in the pore, thereby enabling solid-state nanopore sequencing.

Acknowledgments

To my lovely wife, Supriya, I thank you for the wonderful love and support through what has been a rewarding yet testing academic journey filled with joy, success and happiness and at times disappointment and failure. Supriya, without your support and love I would not be writing this acknowledgments section today.

To my wonderful adviser, Dr. Bashir, thank you for having the faith and trust in me right from the beginning (old Purdue days). You have helped me and guided me through some of my toughest times and I will forever be grateful. Under your tutelage, I believe I have developed into a free thinking and independent researcher who has the whole world ahead of him.

To my parents and brother, thank you for encouraging me and carrying me though all the times when I could not carry myself. To my dad, thank you for being my inspiration. To my loving mum, thank you for repeatedly asking “So, how much longer before you graduate? Another 6 months? You’ve been saying that for the last two years.” The day you’ve been waiting for is almost here.

Table of Contents

List of Frequently Used Acronyms

5mC	5-Methyl Cytosine
AAO	Anodic Aluminum Oxide
ACS	American Cancer Society
AFM	Atomic Force Microscopy
ALD	Atomic Layer Deposition
APTES	Aminopropyltriethoxysilane
BCD	Bubble Collapse Deposition
BLM	Black Lipid Membrane
DNA	Deoxyribonucleic Acid
dsDNA	Double stranded DNA
ssDNA	Single stranded DNA
EDTA	Ethylenediaminetetraacetic Acid
EELS	Electron Energy Loss Spectroscopy
EFTEM	Energy Filtered Transmission Electron Microscopy
ERα	Estrogen Receptor α
ERE	Estrogen Response Element
FESEM	Field Emission Scanning Electron Microscopy
FRAP	Fluorescence Recovery After Photobleaching
GFET	Graphene Field Effect Transistor
HRTEM	High Resolution Transmission Electron Microscopy
LPCVD	Low Pressure Chemical Vapor Deposition
MBD	Methylated DNA Binding Domain
MBD2	Methylated DNA Binding Protein 2
MWCNT	Multi-walled Carbon Nanotubes
NED	Nanoarea Electron Diffraction
PCR	Polymerase Chain Reaction
qPCR	Quantitative PCR
PAGE	Polyacrylamide Gel Electrophoresis

PDMS	Poly (Dimethyl Siloxane)
PECVD	Plasma Enhanced Chemical Vapor Deposition
PET	Polyethylene Terephthalate
PMMA	Polymethyl Methacrylate
RNA	Ribonucleic Acid
SAM	Self Assembled Monolayer
SEM	Scanning Electron Microscopy
SNP	Single Nucleotide Polymorphism
SPB	Supported Phospholipid Bilayer
SVL	Supported Vesicle Layer
TEM	Transmission Electron Microscopy
VLSI	Very Large Scale Integration
XPS	X-ray Photoelectron Spectroscopy

Introduction 1

The discovery of DNA as the blueprint of life in all living organisms is of fundamental importance in medicine and biology. DNA contains the instruction set that is used to encode RNA and proteins, the machinery that drives all cellular activity. Chemically, DNA consists of two long polymers composed of simple sub-units called nucleotides arranged in a double helix structure. Each nucleotide consists of a sugar-phosphate backbone attached to one of four types of molecules called bases, more specifically adenine, thymine, cytosine and guanine. It is the sequence of these four bases along the DNA backbone that encodes the genetic information that defines the various characteristics of an organism. The structure and function of DNA is discussed in greater detail in chapter 2. Due to the vast information content of DNA and its importance in regulating cellular behavior, widespread research is focused on the development of technologies applicable to DNA analysis and sequencing.

Sequencing the human genome has helped further our understanding of disease, inheritance, and individuality. Genome sequencing has been critical in the identification of Mendelian disorders, genetic risk factors associated with complex human diseases,[1, 2] and continues to play an emerging role in therapeutics and personalized medicine. The growing need for cheaper, faster genome sequencing has prompted the development of new technologies that surpass conventional Sanger chain termination methods in terms of speed and cost.[3, 4] These novel second and third generation sequencing technologies, inspired by the $1000 genome challenge proposed by the National Institute of Health in 2004 (http://www.genome.gov/12513210), are expected to revolutionize genomic medicine. Nanopore DNA sequencing is one such technology that is currently poised to meet this grand challenge.[5]

Nanopore DNA sequencing is attractive as it is a label-free, amplification-free single-molecule approach that can be scaled for high throughput DNA analysis. This technique typically requires low reagent volumes, benefits from relatively low cost and supports long read lengths,

potentially enabling de novo sequencing and long-range haplotype mapping. The principle of nanopore sensing is analogous to that of a Coulter counter. A nano-scale aperture or nanopore is formed in an insulating membrane separating two chambers filled with conductive electrolyte. Charged molecules are electrophoretically driven through the pore under an applied electric potential, thereby modulating the ionic current through the pore. The corresponding electronic signature reveals useful information about the structure and dynamic motion of the translocating molecule. This concept can be extended to sequencing in that if each passing nucleotide in single stranded DNA (ssDNA) yields a characteristic residual ionic current, this current trace can then be used to extract sequence information.

Recent developments in biological nanopores suggest that nanopore sequencing is indeed feasible. Proof-of-principle experiments using biological α-*hemolysin* and *MspA* nanopores have shown significant progress in this direction. This review focuses on recent advances in this area along with new developments in solid-state and hybrid nanopore technology, in particular the incorporation of graphene that could enable single nucleotide discrimination and ultrafast sequencing. Efforts to slow down DNA translocation (figure 1) and novel sensing architectures and modalities that add functionality to the nanopore are also examined (table 1).

Table 1 Nanopore sequencing techniques and potential challenges. Ionic current approaches have shown significant success in proof-of-principle sequencing experiments, particularly sequencing by exonuclease digestion and DI sequencing. Nanopore based optical approaches also show promise but require extensive conversion of DNA. Computational studies (references shown in red) suggest that transverse electron tunneling and capacitive nanopore approaches may also facilitate ultrafast sequencing, though the experimental realization of these techniques is still pending.

Sensing Modality	Description of Technique	Potential Challenges	Ref.
Ionic Current	Hybridization assisted nanopore sequencing	High spatial resolution required, Complex algorithms needed for analysis	[6]
	Sequencing by exonuclease digestion	Requires sequential passage of mononucleotides in order in which they are cleaved	[7,8]
	Sequencing by synthesis	Retaining replicating complexes at the pore, Achieving long read lengths	[9,10]
	Duplex Interrupted (DI) DNA sequencing	Converting large genomic ssDNA fragments to DI structure	[11]
Optical Readout	Optical recognition of converted DNA	Complex and error-prone DNA conversion steps, High density < 2nm nanopore arrays needed	[12]
Transverse electron tunneling	Tunneling detector on a nanopore (Metal, Graphene, Carbon Nanotubes)	Precisely controlling orientation and position of nucleotides in the gap, Slow translocation rates required to sufficiently sample over noise, Nucleotide dependent tunneling currents need to be measured in solution	[13,14]
Capacitive Sensing	Metal-Oxide-Semiconductor nanopore capacitor	Must operate in high ionic strength solution with negligible drift and leakage, DNA translocation rates need to be substantially reduced	[15,16,17]

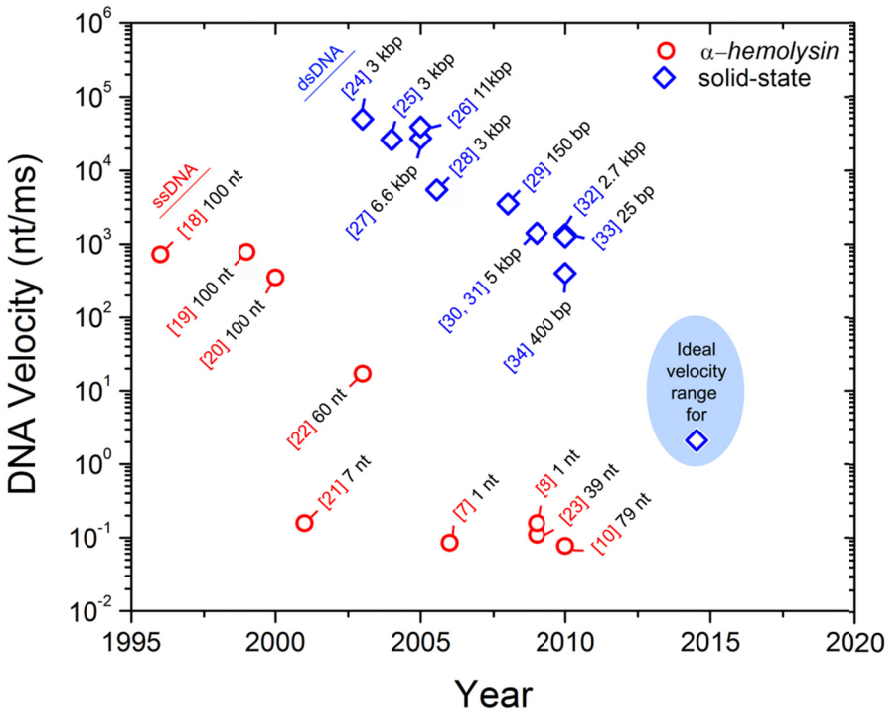

Figure 1 Trends in nanopore DNA analysis. Methods to regulate DNA translocation have resulted in a substantial reduction in DNA translocation velocity each year since the inception of this technology, for both α-*hemolysin* and solid-state nanopores. Recent advances in biological nanopores have resulted in ssDNA transport speeds as low as ~1 nt/10 ms, and improved sensitivity (down to a single nucleotide (nt), refs [7,8]), enabling nanopore DNA sequencing. Similar trends are observed with solid-state nanopores, though further reductions in DNA velocity and substantial improvements to sensitivity are still required. A DNA velocity range of 1– 100 nt/ms should be ideal for the high resolution analysis of DNA using solid-state nanopores, potentially enabling rapid electronic sequencing whilst limiting electrical noise. The development of new sensing modalities and architectures (tunneling junctions, capacitive nanopore structures, graphene gate, chemical functionalization) will be of fundamental importance in working towards this goal, though significant challenges are still faced in the development of such technologies (table 1). This figure contains key nanopore developments targeted at slowing DNA translocation and enhancing sensitivity, but is by no means an exhaustive list. Each data point in this plot contains the reference number and the shortest molecule detected in the referenced study.

The application of these new techniques to sequencing and the associated challenges are briefly presented but are reviewed in more detail by Branton.[5] Finally, the application of nanopores to

areas outside sequencing are discussed, particularly the emerging role of this technology in medical diagnostics. The concept of nanopore DNA sensing is shown in Figure 2.

1.1 Motivation

The motivation for this work is to develop cost-effective, single molecule sensors capable of detecting specific target DNA analytes at ultra-low concentrations in small sample volumes. This technology could serve as a diagnostic tool in clinical applications such as early cancer detection and also contribute to development of next generation sequencing technologies.

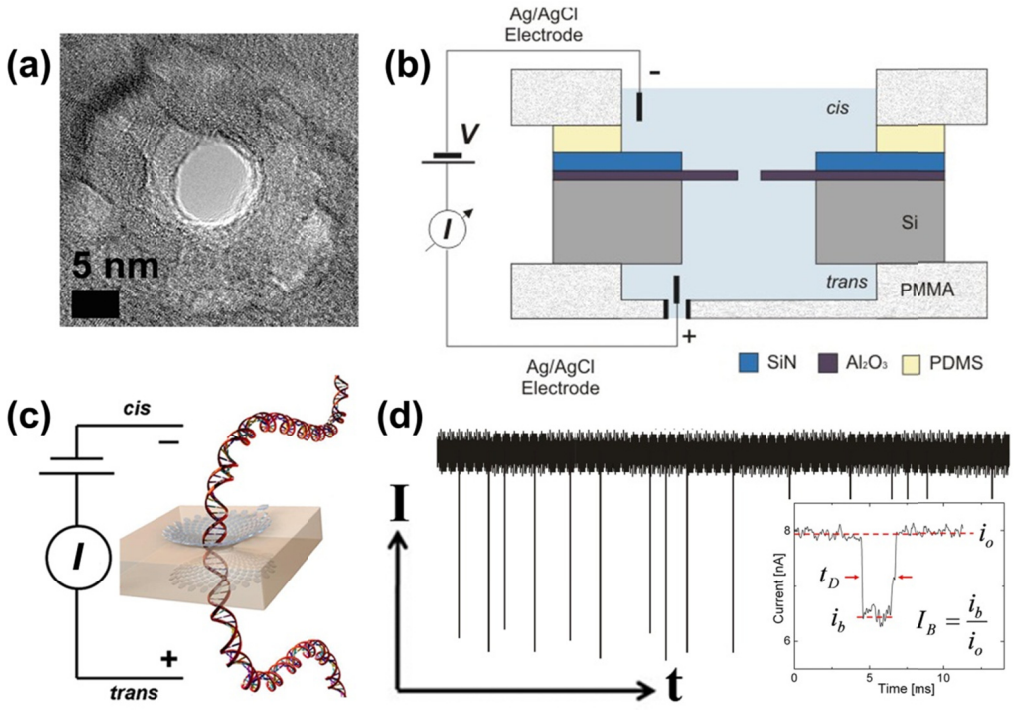

Figure 2 (a) Transmission electron microscope (TEM) image of a 7 nm nanopore. (b) Nanopore fluidic setup showing Si nanopore chip encapsulated between two chambers of a PMMA flow cell filled with conductive electrolyte. (c) Schematic of DNA transport through a nanopore. (d) Characteristic downward current blockades seen during the transport of individual DNA molecules through the pore. (Inset of (d)) Current signature corresponding to a single DNA translocation event showing blockage ratio and translocation time specific to that translocation event.

Nanopore Sensors for Early Cancer Detection

Cancer is a leading cause of death worldwide accounting for approximately 13% of all deaths in 2004. According to estimates by the American Cancer Society (ACS), more than 12 million new cancer cases were expected in 2007 combined with an additional 7.6 million deaths world-wide (about 20,000 cancer related deaths per day). By 2050, the global burden associated with cancer is expected to grow to over 27 million new cases and 17.5 million cancer related deaths. This burgeoning problem is further compounded by inadequate cancer screening procedures. Conventional screening procedures rely on direct palpation, visual detection, imaging and biopsy analysis to detect malignancies. These techniques, however, are only effective after the tumor has reached a detectable size during which time cancerous cells are free to mature, proliferate and potentially metastasize in the body, presenting a danger to patients' health. Also, the late presentation of symptoms in many cancer types further contributes to high cancer related mortality rates. To improve patient survival rates, novel strategies focused on early cancer detection at the genetic and epigenetic levels are needed.

It is becoming more and more apparent that cancer is as much a disease of misdirected epigenetics as it is a disease of genetic mutations. Epigenetic alterations occur in the form of DNA methylation changes, an early and frequently observed event in carcinogenesis.[35] Loss of methylation (hypomethylation) in specific genes and elevated methylation levels (hypermethylation) in others have been associated with cancers of the prostate, breast, lung, head and neck and liver to name a few, and also correlate with disease severity and metastatic potential in many tumor types.[35-39] Interestingly, cancer-specific methylated DNA from most tumor types is present at very low concentrations in bodily fluids and biopsy specimens and also exists in the form of free-floating DNA shed by dead cancer cells.[35] A technology capable of detecting aberrant methylation patterns in specific genes extracted from the serum of cancer patients would be of immense clinical value.

We establish a framework for the detection of robust cancer biomarkers (specifically DNA methylation patterns) using solid-state nanopores. Nanopore technology is well suited for gene

based methylation analysis and could be capable of screening small panels of hypermethylation markers specific to a variety of cancers. The power of this technique over conventional methylation analysis techniques lies in its ability to (1) detect target molecules at extremely low concentrations from minute sample volumes (essential in early cancer detection due to the low concentration of DNA shed by tumor cells in serum), (2) detect a combination of methylation aberrations across a variety of genes (important in monitoring progression and prognosis), (3) provide rapid methylation analysis at relatively low cost (small reagent volumes needed due to single molecule nature of this approach), and (4) eliminate cumbersome and expensive PCR, DNA sequencing and bisulfite conversion steps. Nanopore sensors, therefore, could potentially play an important role in early cancer detection, risk assessment, disease monitoring, chemoprediction and patient prognosis.

1.2 Overview

Chapter 2 is a comprehensive review of biological and solid-state nanopore systems. First, the state-of-the-art in biological nanopores is discussed. An introduction to solid-state nanopores including their fabrication, noise performance and DNA transport characteristics is next provided. Finally, the performance of chemically modified solid-state nanopores is discussed. A summary of this chapter was recently published as a book chapter in *Nanopores, Sensing and Fundamental Biological Interaction* (Springer, 2011).

Chapter 3 presents the development of highly sensitive, mechanically robust, Al_2O_3 nanopores for DNA detection. This work was featured on the cover of *Advanced Materials*.[30] The process described achieves high yield, greatly reduces fabrication complexity and results in structurally robust, low noise platforms for single molecule DNA analysis. Al_2O_3 nanopore sensors have all the advantages of existing SiO_2 and Si_3N_4 architectures (size control with sub-nm precision, chemical modification and attachment of organosilanes) but also exhibit superior noise performance over their solid-state counterparts. This technology serves as a template to further explore the physics governing DNA transport and finds broad application in bio-nanotechnology.

Chapter 4 presents an in-depth study of the dynamics of nanopore formation in metal oxide thin films and the biophysics of single molecule transport through these nanopore channels.[31] The concepts of nanoscale surface charge engineering and nanopore metallization directly through electron beam based decompositional sputtering of Al_2O_3 films are introduced. This in-situ metallization process provides a potential means to create nano-scale metallic contacts in the pore region for manipulating surface charge and pore conductivity. Nano-crystalline surface enhanced DNA transport through these Al_2O_3 nanopores is also discussed.

Chapter 5 presents the development of hybrid biological/solid-state nanopores that seek to combine the stability and top down fabrication of solid-state nanopores with the chemical selectivity of biological nanopores. The integration of stable phospholipid bilayers with large Al_2O_3 nanopores formed using focused ion beam milling processes is discussed. These phospholipid membranes on ALD Al_2O_3 formed high impedance GΩ seals, were stable for over 50 hours, maintained lateral fluidity and may be well suited for the potential integration of biological nanopores.

Chapter 6 summarizes new and unpublished data on the integration of graphene electrodes into an Al_2O_3 nanopore. The stability and pH response of these novel sensors is presented. Applications involving the detection of dsDNA and of estrogen-receptor/DNA complexes are discussed. Finally, preliminary data on the modulation of ionic current through the nanopore using the graphene gate is presented.

Theory and Literature Review 2

2.1 Biological Nanopores

Biological nanopores reconstituted into lipid bilayers present an attractive option for single molecule DNA analysis. Their versatility can be attributed to several factors: X-ray crystallographic information is available revealing pore structure with angstrom level resolution; techniques such as site directed mutagenesis can be used to tailor the physical and chemical properties of a pore; and remarkable heterogeneity is observed among pores in terms of size and composition. The biological cell contains various types of nanopores and nanochannels that regulate the flow of ions and molecules relevant to cellular processes such as intercellular communication and signaling between subcellular structures. Examples include gated, selective ion channels that connect the cell cytosol to the cell exterior; nuclear membrane pores that control the passage of biomolecules such as messenger RNA (mRNA) from the cell nucleus into the cytosol; proteins that are secreted across pores in the membranes of cell organelles; and viruses, which dump their genomes into cells via pores that insert into the cell membrane.[40] An example of a biological nanopore that is frequently used in in-vitro studies is the α-hemolysin channel.

2.1.1 α-hemolysin

α-*hemolysin* is a naturally occurring biological protein complex extracted from the bacterium *Staphylococcus aureus* that, when inserted into a lipid bilayer membrane, forms a ~1.5 nm diameter pore allowing the passage of ions and ssDNA. In vivo, bacterium *Staphylococcus aureus* secretes alpha-hemolysin monomers that bind to the outer membrane of host cells. These monomers self-assemble into seven subunit oligomers to form a water-filled transmembrane channel that facilitates the uncontrolled permeation of water, ions, and small organic molecules in and out of the host cell. The resulting discharge of vital molecules from the host cell, osmotic swelling and a loss in ionic gradient can result in irreversible cell damage and eventually cell

death (apoptosis). Apoptosis induced by the insertion of α-hemolysin into various cell types including rabbit erythrocytes, human erythrocytes, monocytes, and lymphocytes has been reported.[41, 42]

In-vitro studies of DNA transport through biological pores have traditionally focused on α-hemolysin as the transmembrane channel of choice. The structure of the heptameric α-hemolysin pore is shown in figure 3a (i). The total channel length is 10 nm and is comprised of a 5 nm vestibule that protrudes into the *cis* compartment and a 5 nm transmembrane domain embedded in the lipid bilayer[43]. At pH 7-9, α-hemolysin forms a relatively stable and reproducible non-gating channel with less than 2% variation in open pore current under temperature stabilized conditions. The comparable inner channel diameter of α-hemolysin to ssDNA (diameter ~1.3 nm) suggests that less than one Debye length (~3 Å in 1 M KCl) separates the translocating biomolecule from the amino acid residues in the pore. Although dsDNA is too large to translocate through α-hemolysin, up to a 10 bp fragment can reside in the vestibule.[43] This makes α-hemolysin a very powerful tool for examining biomolecular interactions and the binding affinities of individual molecules at the single molecule level.

In a landmark study, Kasianowicz demonstrated the ability to electrically detect individual ssDNA and ssRNA molecules using α-hemolysin nanopores embedded in planar phospholipid bilayers.[44] A plethora of studies have since followed elucidating the biophysics of single molecule transport through proteinaceous α-hemolysin. For example, Meller et al. examined the effects of polymer length on translocation velocity.[45] Polymers longer than the pore length were seen to translocate at constant speed, but short polymers exhibited a length dependent velocity. Studies by Mathe et al. revealed that α-hemolysin nanopore sensors are sensitive enough to differentiate between 3' and 5' threading of ssDNA in the pore with 5' threading resulting in a twofold increase in translocation times relative to 3' threading, attributed to the tilt reorientation of bases towards the 5' end of the molecule.[46] Brun et al. demonstrated that biomolecule flux through proteinaceous α-hemolysin is highly dependent on the applied voltage, with the capture rate of ssDNA[47, 48] and small polyelectrolytes[49] following a simple Van't Hoff-Arrhenius relationship. Henrickson further showed that the asymmetric structure of α-hemolysin promotes biomolecule entry from the *cis* side (side with the vestibule) as opposed to the *trans* side.[50]

Reduced biomolecule flux from the *trans* side was attributed to a combination of factors: (1) the high entropic barrier associated with the highly confined geometry of the β barrel on the *trans* side, and (2) electrostatic repulsion of DNA by the negatively charged asparatic acid residues located on the *trans* side. The unzipping of hair-pin DNA structures using α-hemolysin was observed by Vercoutere et al. for sufficiently short hairpins.[51] The authors demonstrated the ability to discriminate between 3 bp and 8 bp long hairpins with single base resolution.[51] Early results also demonstrated the ability of native α-hemolysin to distinguish between freely translocating RNA homopolymers of cytidylic and adenylic acid,[19] as well as poly(dA) and poly(dC) strands of ssDNA,[47] suggesting the potential emergence of α-hemolysin as a next-generation DNA sequencing tool. The realization of such a tool, however, has proven challenging, primarily due to the remarkably high velocity with which ssDNA moves through the pore under typical experimental conditions (estimated at ~1 nucleotide/μs). At these timescales, as few as ~100 ions are available to correctly identify a translocating nucleotide, a daunting proposition given thermodynamic fluctuations (statistical variations in the number of charge carriers and position of the nucleotide in the pore) and the subtle chemical differences that exist among nucleotides. It has, therefore, proven nearly impossible to sequence freely translocating ssDNA using α-hemolysin.

α-Hemolysin nanopores also hold tremendous value in the field of DNA sequencing. Stoddart recently demonstrated the ability to resolve individual nucleotides located in homopolymeric and heteropolymeric ssDNA immobilized in biological α-hemolysin.[52] Mitchell et al. showed that chemical labels attached to bases could be used to resolve individual bases in a translocating DNA strand.[53] Interestingly, blockage durations and amplitudes could be tuned by varying the chemistry, charge and size of these chemical tags, suggesting the possibility of base discrimination based on peptide labeling with application to DNA sequencing. Another novel nanopore-based sequencing approach was proposed by Cockcroft et al. that exploited the selective, base-by-base activity of DNA polymerase.[9] By anchoring a DNA/DNA-polymerase complex in the nanopore, the authors were able to electrically monitor single nucleotide primer extension events. Primer extensions were controlled by providing each nucleotide set sequentially and sequence information was extracted temporally.[9] The Bayley group recently demonstrated the ability to continuously resolve indigenous single nucleotides (dAMP, dCMP,

dGMP, dTMP) through nanopore based resistive current measurements.[8] Remarkably, individual bases could be discriminated based on current blockade levels without any prior labeling or chemical modification, as shown in figures 3a (ii and iii). Selectivity was achieved by modifying the mutant α-hemolysin pore with a cyclodextrin adapter ($am_6amPDP_1\beta CD$), covalently bound within the β barrel of the transmembrane domain, thereby constricting the nanopore channel while enhancing the chemical specificity of the sensor. Raw bases were read with over 99% confidence under optimal operating conditions.

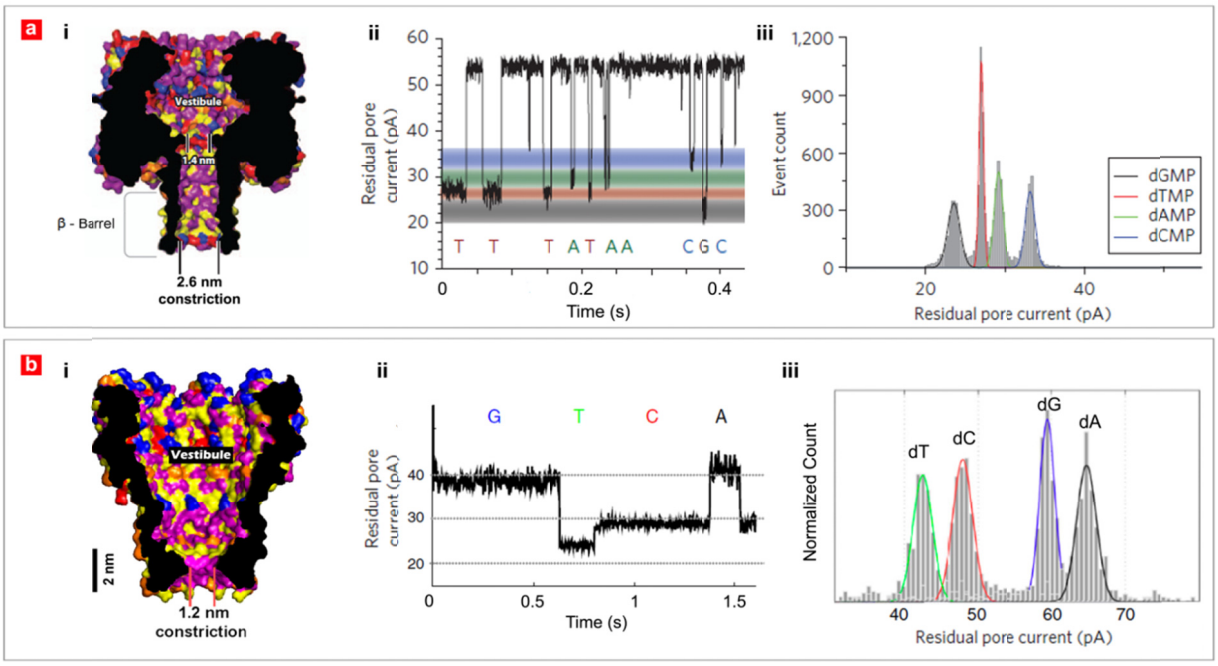

Figure 3 Biological nanopores for DNA sequencing. (a) i. Structual cross-section of α-hemolysin. 1.4 nm constriction permits the passage of ssDNA but not dsDNA. ii. Typical current blockade levels induced by individual nucleotides as they traverse a aminocyclodextrin modified α-hemolysin nanopore. iii. Nucleotide separation efficiency of α-hemolysin under optimized conditions. Coupled with an exonuclease, a sequencing by digestion approach is likely feasible. (b) i. Structural cross-section of MspA. ii. Typical current blockades induced by the translocation of duplex interrupted DNA through MspA. Unique current levels are observed for each nucleotide in a duplex interrupted molecule. iii. Histogram showing the enhanced nucleotide separation efficiency of MspA over α-hemolysin.

By integrating this base identification platform with a highly processive exonuclease through chemical attachment, or genetic fusion, a single molecule sequencing by digestion approach may

be feasible. Another interesting side note from this study was the ability to distinguish 5-methylcytosine from the four other bases. This result holds tremendous value as it provides a rapid and cost-effective method to identify DNA methylation patterns in specific genes with broad application in epigenetics and cancer diagnostics.

Although α-hemolysin has by far dominated the nanopore sequencing landscape, it is plausible that more efficient nanopore sequencing architectures will emerge. A structural drawback with α-hemolysin pertains to its ~5nm long cylindrical β barrel that accommodates up to ~10 nucleotides at a time. The current modulation induced by these nucleotides dilutes the ionic signature specific to a single nucleotide in the 1.4 nm constriction. This limitation is overcome by a relatively new candidate in the nanopore sequencing arena, the channel protein Mycobacterium smegmatis porin A (MspA). MspA is an octameric protein channel that contains a single constriction of diameter ~1.2 nm with a channel length of ~0.5 nm, forming a funnel shape as shown in the structural cross section of figure 3b. Derrington et al. demonstrated the ability of genetically engineered MspA to discriminate between individual nucleotides with an impressive 3.5-fold enhancement in nucleotide separation efficiency over native α-hemolysin.[11] Interestingly, in experiments involving immobilized DNA, as few as three nucleotides within or near the constriction of MspA were seen to contribute to the pore current, a significant improvement over native α-hemolysin. The authors hypothesize that this could be further improved to perhaps a single nucleotide through site-specific mutagenesis, an obvious goal of future mutants. The application of MspA to *de novo* sequencing is not without challenges either. The speed of unimpeded ssDNA translocation through MspA still remains too fast to sequence ssDNA 'on the fly.' Strategies such as duplex interrupted (DI) nanopore sequencing which involves arresting the translocation of a molecule in the pore using DNA duplexes prior to nucleotide identification has shown preliminary success,[11] but the ability to convert and read large genomic fragments with high fidelity still remains to be seen.

2.1.2 Bacteriophage *phi*29 Connector

Another biological nanopore that is receiving much interest of late is the connector protein from the bacteriophage *phi29* DNA packaging motor.[54] In bacteriophage *phi29*, linear dsDNA is

packaged into a viral capsid through an entropically unfavorable process that requires the hydrolysis of ATP. During packaging, the linear DNA passes through a narrow channel of inner diameter ~3.6 nm, termed the connector as shown in figure 4a. The connector is comprised of twelve GP10 protein subunits that readily self-assemble in solution to form a stable, repeatable do-decameric structure. The dimensions of the *phi29* connector channel are shown in figures 4b and 4c. As the crystal structure of this biological nanopore channel has been resolved, explicit site engineering is indeed possible.[55] Wendell et al. modified the *phi*29 connector protein to include hydrophilic sites on the crown and base, thereby allowing for integration into liposomes.[54] The insertion of the *phi*29 connector into preformed lipid bilayers was achieved through vesicle fusion resulting in steady, repeatable pore conductances. Pore conductances were ~5 times higher than that observed in α-hemolysin under similar conditions and did not show any voltage gating effects.[54] *Phi*29 has one distinct advantage over α-hemolysin. The larger barrel allows the translocation of dsDNA and a variety of proteins that are simply too large to pass through α-hemolysin. Thus, the *phi*29 connector system allows the experimentalist to examine a broader spectrum of biomolecule interactions at the single molecule level. Wendell et al. demonstrated the successful detection of 5.5kbp dsDNA and 35 bp dsDNA using this novel biological nanopore platform.

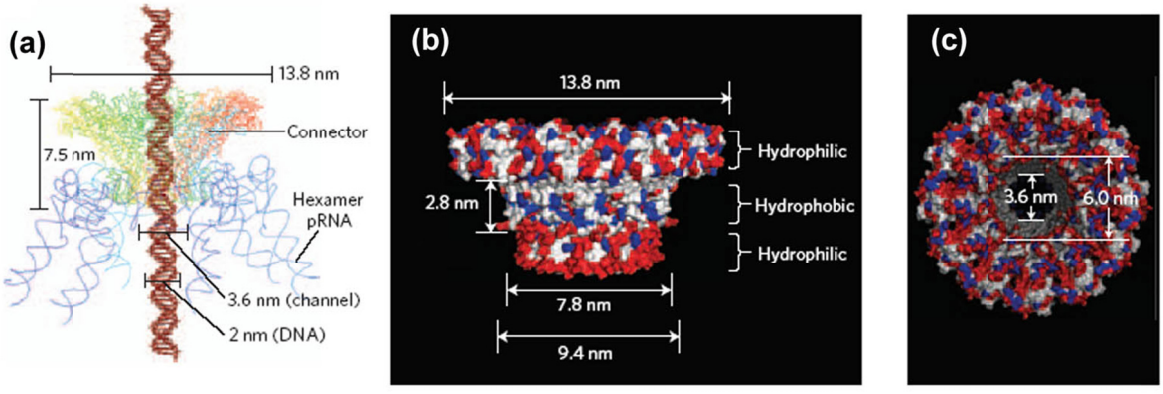

Figure 4 (a) Illustration of the entire *phi*29 DNA packaging motor showing DNA translocation through the connector. (b) Side view of the *phi*29 connector, showing the acidic (red), basic (blue) and other (white) amino acids. (c) Top view of the connector showing the diameter of the narrow and wide part of the channel.[54]

2.2 Solid-State Nanopores

Despite the heterogeneity and remarkable sensitivity of biological nanopores, these sensors do exhibit some disadvantages. The delicate nature of the mechanically supporting lipid bilayer, the sensitivity of biological pores to experimental conditions (pH, temperature, salt concentration), and challenges associated with large scale array integration for high throughput DNA analysis/sequencing make the solid-state approach quite attractive. With advances in microfabrication techniques, solid-state nanopores are fast becoming an inexpensive and highly versatile alternative. Solid-state nanopores exhibit superior chemical, thermal, and mechanical stability over their biological counterparts and can be mass fabricated with sub-nanometer precision. The first reports of DNA sensing using solid-state nanopores emerged from the Golovchenko lab in early 2001. Nanopores were formed in thin SiN membranes using a custom built feedback controlled ion beam sculpting tool, a process that yielded true nanometer control over pore size.[56] Today, most groups prefer to use a focused convergent electron beam from a field emission gun (FEG) TEM to decompositionally sputter nanopores in thin insulating membranes, a technique that has evolved since the 1980s.[57] A review on the fabrication of solid-state nanopores and their applications in single molecule biophysics is provided by Dekker.[40]

SiN has traditionally been the nanopore membrane material of choice due to its high chemical resistance and low mechanical stress, deposited via an optimized low pressure chemical vapor deposition process. This process, however, lacks thickness control in the sub-nanometer regime. To effectively probe the local structure of DNA with the resolution of an individual nucleotide, insulating membranes of sub-nanometer thickness are required. In working towards this goal, our group proposed forming nanopores in ultra-thin insulating Al_2O_3 membranes deposited via atomic layer deposition (ALD). The process conceived by Venkatesan et al. combined the atomic precision of ALD with the high chemical etch selectivity of Al_2O_3 to form mechanically robust membranes anchored on Si.[30] Nanopores were formed in 15 - 60 nm thick Al_2O_3 membranes using a focused convergent electron beam with sub-nanometer control over pore diameter. Two interesting phenomena were observed during pore formation: the dose-dependent conversion of Al_2O_3 to metallic Al, applicable to the direct 'write' of nanoscale electrodes in the pore, and the

controlled formation of α and γ nanocrystalline domains, permitting nano-scale surface charge engineering at the pore/fluid interface.[31] Controlling pore stoichiometry and surface charge density is important given the impact of these parameters on 1/f noise and DNA transport velocities. In line with these findings, slower DNA translocation was observed in Al_2O_3 nanopores relative to SiN, attributed to strong electrostatic interactions between the positively charged Al_2O_3 surface and negatively charged DNA. This ALD based technique has been extended to form nanopores in membranes of thickness ≈5 nm, below which significant ion permeation through the membrane was observed. To achieve true atomic membrane thicknesses, a novel material system/approach is likely needed. These results will be reviewed in detail in chapters 3 and 4.

Graphene perhaps is the solution. Graphene, an atomically thin sheet of carbon atoms densely packed into a two-dimensional honeycomb lattice, possesses remarkable mechanical, electrical and thermal properties.[58] The comparable thickness of a graphene monolayer to the 0.32-0.52 nm spacing between nucleotides in ssDNA makes this material particularly attractive for electronic DNA sequencing. The incorporation of graphene into nanopores was recently demonstrated by three groups.[59-61] In separate studies, the Golovchenko, Dekker, and Drndic labs reported on the electron-beam based fabrication of 5-25 nm diameter nanopores in suspended graphene films, prepared through either chemical vapor deposition (CVD) or exfoliation from graphite.[59-61]

Nanopores were formed in as few as 1-2 monolayers of grapheme as shown in figure 5, these membranes exhibiting remarkable durability and insulating properties in high ionic strength solution.[59] Pore conductance was seen to scale linearly with pore diameter, indicative of pores formed in near infinitesimally thin membranes. An effective membrane thickness of ~0.6 nm was extracted. The translocation of dsDNA through graphene pores was demonstrated in all three studies with subtle fluctuations in the ionic current marking the transport of both folded and unfolded DNA structures.[59-61] DNA translocation velocities ranged anywhere from 10 to 100 nts/μs, too fast for the electronic measurement of individual nucleotides. As a result, Garaj probed the theoretical spatial and geometric resolution of a graphene nanopore using computational analysis.[59] Pseudo-static simulations of dsDNA in a 2.4-nm diameter graphene

pore of thickness ~0.6 nm revealed a resolution of ~0.35 nm, identical to the size of an individual DNA nucleotide. This intriguing result suggests that if DNA translocation could be sufficiently slowed in a graphene pore to say ~1 nt/ms, single nucleotide detection is theoretically possible, potentially enabling electronic sequencing. Despite these exciting developments, a number of fundamental questions still remain. Is it experimentally possible to resolve a single nucleotide in a graphene pore given thermodynamic fluctuations and electrical noise? Can graphene alone electrically discriminate between nucleotides given the chemical and structural similarity among purines and pyrimidines? Is graphene surface functionalization required to impart nucleotide specificity and does this surface modification compromise the resolution of the pore due to membrane thickening? Though the immediate route to sequencing using graphene nanopores is unclear, this exciting yet preliminary work is certain to be the precursor for many future studies. A detailed review of solid-state nanopore technology is presented next.

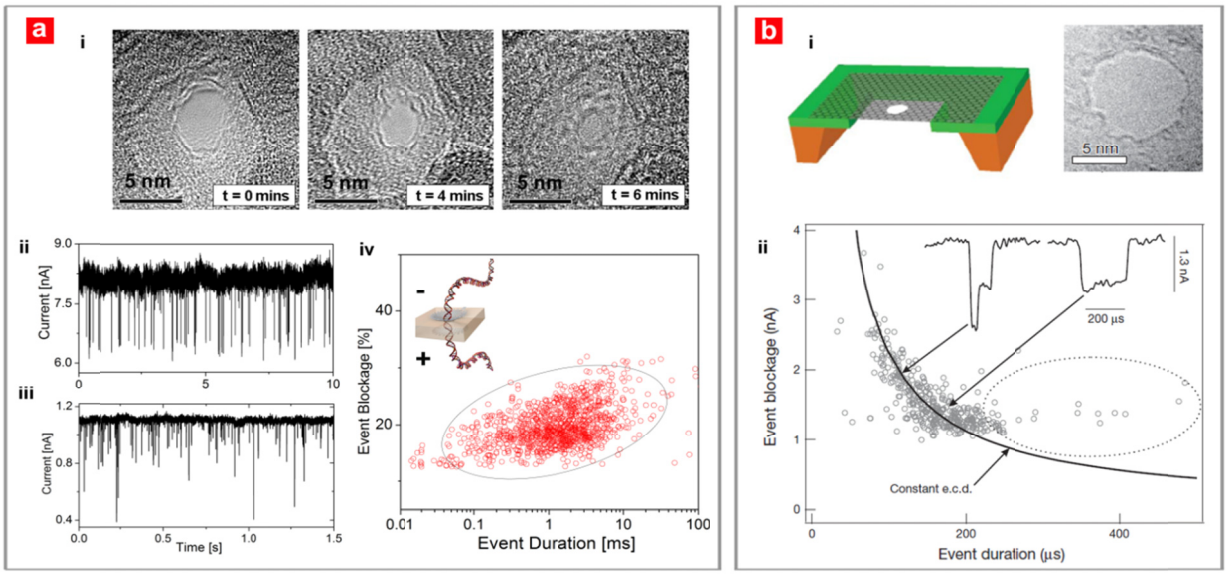

Figure 5 Solid-state nanopore architectures for DNA anaysis. (a) Al_2O_3 nanopores. i. Formation and controlled contraction of nanopores in ALD Al_2O_3 membranes using a focused electron beam. Subnanometer precision is achievable. The introduction of 5 kbp dsDNA resulted in definitive downward current blockades at both. (ii). high salt (1M KCl) and (iii). low salt (100mM KCl) concentrations. iv. Scatter plot of 5kbp dsDNA translocation through a 5 nm Al_2O_3 pore showed a single blockage level (20% of the open pore current) corresponding to linear dsDNA transport.[30] (b) Graphene nanopores. i. TEM based formation of nanopores in 1-2 monolayers of graphene. ii. Scatter plot shows unique conductance signatures that are representative of different DNA conformations translocating through the pore (folded and unfolded DNA).

2.2.1 Nanopore Fabrication

2.2.1.1 Fabrication of Single Nanopores

There are four primary techniques available for the fabrication of single solid-state nanopores in thin Si_3N_4, SiO_2 or polymer membranes. They are surface tension driven oxide reflow, ion beam sculpting, the track-etch method and electron beam based decompositional sputtering. Other direct fabrication techniques include focused ion beam (FIB) milling to achieve pore sizes as low as 10nm[62] and laser ablation methods capable of achieving sub 100nm pore diameters.[63, 64]

Electron Beam Induced Oxide Reflow

The oxide reflow technique involves the use of electron beam lithography to pattern large 40-100nm holes in micro-machined silicon membranes. These pores are subsequently oxidized and shrunk to the sub-10nm range using a TEM. The TEM shrinking process, discovered by Storm et al.,[65] uses the high energy electron beam to locally fluidize the oxide surface in the vicinity of the nanopore causing the oxide to reflow in the direction that minimizes interstitial surface energy. For nanopores with diameter $d < t$, where t is the membrane thickness, nanopore shrinking was repeatedly observed. Schenkel et al. attributed this shrinking phenomenon to the build-up of a low-Z hydrocarbon layer in the nanopore during electron-beam irradiation.[66] Electron energy loss spectra (EELS) from the localized nanopore region, however, revealed the presence of only Si and O and the absence of C,[65] thereby confirming that oxide reflow is indeed the mechanism responsible for nanopore contraction.

Ion Beam Sculpting

The ion-beam sculpting process first developed by Li et al.[56] uses an energetic beam of Ar^+ ions to form nanopores with dimensions as low as 1.5 nm in thin Si_3N_4 membranes. Contrary to what one would expect, a 3 keV Ar^+ ion beam rastered continuously over a Si_3N_4 sample at room temperature resulted in ion assisted diffusion of atoms into the pore region resulting in nanopore shrinking as opposed to expansion. The flow of matter to the developing nanopore cite showed temperature dependence with a transition between pore opening and closing being consistently observed at ~5°C, under the ion-beam conditions used. Pore expansion was attributed to ion

sputter erosion at the pore edge, the dominant mechanism at low temperature and high ion flux. Pore closure was accredited to the formation of a stressed viscous surface layer at the lip of the nanopore. The reduced viscosity and/or enhanced stress owing to implantation or surface tension effects cause this layer to relax, thereby filling the nanopore. Feedback control was used to precisely sculpt nanopores of various sizes using this process.

Track-Etch Method

Conical nanopores are typically formed in micron-thick polymer films using the track etch method.[67-69] The fabrication process involves first bombarding a thin sheet of polymer material (polyethylene terephthalate, polyimide or polycarbonate) with a high energy beam of nuclear fission fragments or with a high energy ion beam from a MeV accelerator at normal or near normal incidence angle to the polymer substrate. The irradiated polymer membrane is then placed between two chambers of a conductivity cell and etched chemically from one side. Chemical etching of the damage track is done in a strong alkaline solution (pH ≈13) with high chlorine content at elevated temperatures (~ 50°C) using a solution such as sodium hypochlorite (NaOCl).[68] The other compartment of the conductivity cell is filled with 1M potassium iodide (KI) solution as a stopping medium for the OCl^- ions of the etchant. As soon as the etchant completely penetrates the polymer film, iodide ions reduce OCl^- to Cl^- ions, thereby halting the etch process. The result is a tapered individual conical nanopore with pore diameter as low as ~10 nm in the polymer membrane.

Electron Beam Induced Sputtering

Electron beam induced sputtering offers a rapid and reliable method to prototype nanometer sized pores using a TEM. This method involves the use of a focused convergent electron beam with sufficiently high current density to decompositionally sputter nanometer-sized pores in thin oxide or nitride membranes (thickness ≤ 60nm). An added benefit of this method is that it allows for the direct fabrication of nanopores and avoids the need for electron beam lithography steps. Kim et al. used high-resolution TEM to explain nanopore formation kinetics in Si_3N_4 as a balance between two competing processes: (a) material sputtering and (b) surface-tension-induced shrinking.[70] Nanopores 4 to 8 nm in diameter were directly drilled using a JEOL 2010F field emission TEM with an accelerating voltage of 200 keV and a beam current density of 10^8 –

10^9 e nm^{-2}. Kim et al. demonstrated that nanopore contraction could be achieved by slightly defocusing the e-beam, effectively reducing the beam intensity to ~10^6 e nm^{-2}.[70] TEM tomography was used to map the three-dimensional structure of these solid-state nanopores. It was observed that the sidewalls of the sputtered pores were angled (approximately 65° to the horizontal), attributed to the intensity distribution of the e-beam around its focal point. Post-drilling, pores formed an 'hourglass' structure with pore width being represented by the width of the narrowest constriction.[70, 71] Similarly, Heng et al. used a focused convergent electron beam to form nanopores in ultra-thin 10 nm Si_3N_4 membranes. The nanopore structure resembled a double cone structure with a cone angle of 10°.[72] Smeets et al. observed a cone angle of 45° for nanopores sputtered in composite SiO_2/SiN/SiO_2 membranes.[73] In all cases, nanopores formed directly through electron beam induced sputtering exhibited the ability to contract under a defocused electron beam.

2.2.1.2 Fabrication of Nanopore Arrays

Multiple methods exist for the formation of nanopore arrays. The track-etch method is one which has been used to produce commercially available nanopore arrays with diameters as low as ~10nm and packing densities as high as 6x10^8 pores/cm^2.[74] Nanopore arrays can also be fabricated through an anodization process of thin aluminum films. In one such process that we have previously explored, aluminum foil is first anodized in a 0.3 M oxalic acid solution at 5°C at a constant applied voltage of 40 V for 20 h.[75] The anodized aluminum is then etched in an aqueous mixture of phosphoric/chromic acid at 60°C. Any remaining Al in the pore region is dissolved using a saturated $HgCl_2$ solution. We used this process to produce anodized aluminum oxide (AAO) membranes with a highly ordered network of nanopores (diameters = 75 nm, center-to-center distance = 105 nm), as shown in figure 6a. These nanopores can be further reduced in size through atomic layer deposition (ALD). Figure 6b shows an array of nanopores with final diameters of 15 ± 1 nm formed using a combination of anodization and ALD processes. Nanopore arrays with pore sizes as low as ~20nm have also been formed in SiO_2 using electron beam lithography processes.[76] Kim et al. demonstrated that nanopore arrays could be fabricated by stepping a focused electron probe formed in a TEM over the sample surface.[71] Though the

process was time intensive, arrays with pore diameters as low as ~ 5nm could be produced this way.

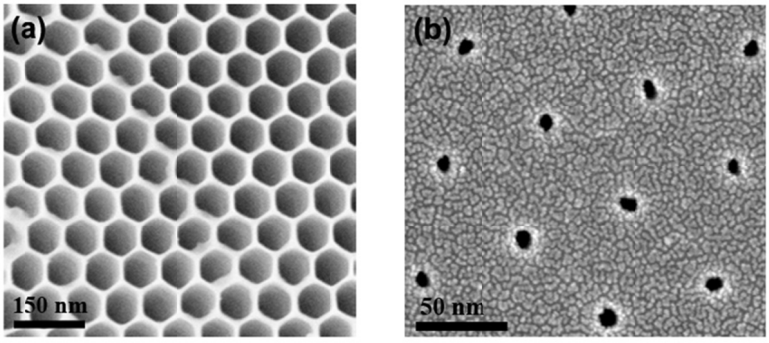

Figure 6 (a) SEM image of an AAO nanopore array. (b) AAO nanopores shrunk using the ALD process[77].

2.2.2 Ionic Conduction through Solid-State Nanopores

2.2.2.1 Nanopore Conductance

The conductance of the nanopore can be measured in monovalent electrolyte, typically KCl, by placing the nanopore between two electrically isolated, fluidic reservoirs. The experimental setup was previously illustrated in figure 2. Typically, high salt solutions well in excess of physiological conditions are used (~ 1 M KCl, 10 mM Tris-HCl, pH 7.5) to obtain sufficiently high baseline current levels that can be monitored using a picoammeter. Faradaic Ag/AgCl electrodes are placed in each reservoir allowing for a localized redox based exchange reaction to occur at each electrode. Linear current-voltage (IV) characteristics are typically observed for nanopores in SiO_2 and Si_3N_4 membranes, formed using TEM based decompositional sputtering processes, suggesting a symmetric nanopore structure.[72, 73] TEM tomograms taken by Wu et al. and Kim et al. on SiO_2/ SiN/ SiO_2 and Si_3N_4 nanopores further confirmed this double cone, symmetric structure.[70, 78]

Asymmetric IV characteristics have also been reported in synthetic nanopores formed in polyethylene terephthalate (PET) polymer membranes[79, 80] attributed to the asymmetric, conical geometries resulting from the track etch method. This conically shaped, highly charged nanopore

is cation selective, exhibiting diode-like behavior in fluid with a preferential direction for the cation flow from the narrow entrance towards the wide opening of the pore. Siwy et al. further demonstrated some of the novel characteristics of this architecture by pumping ions against a concentration gradient using a fluctuating electric field applied across the membrane in the form of an AC voltage signal.[79]

2.2.2.2 Nanopore Surface Charge Effects

The effects of surface charge on pore conductance were investigated by Ho et al. using nanopores formed in 10 nm thick Si_3N_4 membranes.[81] At low electrolyte concentrations (≤10 mM), pore conductivity was found to be much larger than bulk approximations calculated using the pore geometry. This conductance deviation was attributed to Debye layer overlap in the pore where the Debye length is comparable to or larger than the pore radius. Multiscale simulations of ion transport through these pores, coupled with experimental observations, confirmed the presence of fixed negative charges on the pore walls resulting in reduced ion mobility at the pore surface.

Consistent with Ho's results, Smeets et al.[73] found that for ~10 nm diameter SiO_2 pores, the negative surface charge lining the pore walls dominates pore conductivity at salt concentrations below 100 mM KCl. Interestingly, a variable surface charge density in the pore was extracted as a function of electrolyte concentration in these experiments. In contrast, TiO_2 nanopore conductance saturated at much lower electrolyte concentrations.[82, 83] Nam et al. extracted a surface charge density of ~0.005 mC/m^2 in TiO_2 pores, significantly lower than the charge density observed in SiO_2 pores which is estimated at ~25-50 mC/m^2.[82] The author suggested that this low charge density may be responsible for the extremely low KCl concentrations at which ionic conductance saturated. The surface charge characteristics of Si_3N_4 nanopores have also been studied by Wanunu and Meller and revealed only small changes in pore conductance with varying pH.[84]

2.2.2.3 Manipulating Surface Charge in Nanopores

Electrodes positioned in a nanopore may provide a novel method to manipulate pore conductance and surface charge characteristics. Nam et al. embedded a TiN gate electrode

directly in the nanopore and showed current rectification by applying potentials to the gate electrode.[82] This gating behavior was only observed at very low salt concentrations ($<10^{-3}$ M) where the effects of surface charge are dominant and Debye layer overlap in the nanopore is indeed expected. P-type unipolar behavior was observed suggesting that K^+ ions are the majority carriers in these TiO_2 based gated nanopores. Studies by Kalman et al. focused on integrating an Au electrode into a conical nanopore.[85] By modulating the electric potential applied to the gate, one alters the distribution of ions in the overlapping Debye layer in the pore and thus the potential distribution across the pore. Using this approach Kalman et al. were able to manipulate the current through the device from the rectifying behavior synonymous with conical nanopores, to a near linear type behavior as seen in structurally symmetric nanopores. The mechanism for this change in transport behavior was accredited to the enhancement of concentration polarization induced by the gate. The manipulation of surface charge through the chemical modification nanopores will be discussed in subsequent sections.

2.2.2.4 Noise in Solid State Nanopores

Electrical noise in ionic current measurements limits the utility of solid-state nanopore systems in widespread nucleic acid based diagnostics. Two dominant sources of noise have been documented in the literature: a low frequency current fluctuation with 1/*f* characteristics (flicker noise) and a high-frequency background noise component associated with the capacitance of the Si support chip (dielectric noise).[86-91] Minimizing these respective noise components is integral to improving the sensitivity and signal-to-noise ratio of nanopore sensors.

1/f Noise in Solid-State Nanopores

1/f noise has been observed in many physical and biological systems. 1/f noise has been observed as fluctuations in the voltages or currents of semiconductors, the voltage across nerve membranes and synthetic membranes and in the resistance of aqueous ionic solutions.[92] The power spectrum, denoted by *S(f)*, is proportional to the reciprocal of the frequency in a narrow bandwidth as illustrated in equation 1.

$$S(f) = \frac{cons\ \tan t}{|f|^{\alpha}} \qquad where\ 0 < \alpha < 2 \tag{1}$$

Hoogerheide et al. studied the 1/f noise characteristics of Si_3N_4 nanopores as a function of pH and electrolyte ionic strength and concluded that 1/f noise originates from surface charge fluctuations at the nanopore surface.[87] The model presented was based on protonization of surface functional groups and was sensitive to a few tens of active surface groups in the nanopore. In contrast, Smeets et al. concluded that low frequency noise was predominantly due to the total number of charge carriers in the nanopore thereby following Hooge's phenomenological relation, rather than on surface charge characteristics.[88, 89] Surface modifications, however, have been shown to significantly improve the 1/f noise characteristics of nanopores. Chen et al. used an atomic layer deposition process to coat Si_3N_4 nanopores with Al_2O_3 and saw significant reductions in 1/f noise.[93] Tabard-Cossa et al. demonstrated a significant reduction in 1/f noise by treating nanopore chips with piranha solution.[90] It is therefore likely that 1/f noise in nanopores is a combination of the two mechanisms described previously, that is, fluctuations in the total number of charge carriers in the nanopore coupled with a fluctuation in their mobilities due to trapping at surface states. By addressing the surface properties of solid-state nanopores, through either chemical surface treatment or material choice, improved noise performance may be achieved.

Dielectric Noise

Dielectric noise in nanopores is associated with the capacitance of the nanopore chip and scales linearly with frequency. Nanopores are typically fabricated in dielectric thin films such as SiO_2 or Si_3N_4, anchored on a conductive Si substrate. These dielectric materials are typically lossy and have a dissipation factor, *D*, associated with them. Smeets et al. extracted a dissipation factor of 0.27 ± 0.07 for Si_3N_4 pores, strongly deviating from $D = 0$ for an ideal capacitor. The dielectric noise can be reduced by minimizing the capacitance of the substrate. To achieve this, the thickness of insulating layers on the Si substrate can be increased or the fluidic contact area on the chip can be minimized. Tabard-Cossa et al. selectively patterned PDMS on Si_3N_4 chips to reduce the fluidic contact area and thereby minimize dielectric noise.[90]

2.2.3 DNA Transport through Solid-State Nanopores

2.2.3.1 DNA Structure and Function

DNA, or deoxyribonucleic acid, encodes the architecture and function of cells in all living organisms. DNA consists of two polynucleotide strands wound together to form a double helix structure. Watson and Crick concluded that DNA was a complementary double helix consisting of certain pairs of complementary bases, namely adenine (A) and thymine (T), followed by guanine (G) and cytosine (C),[14] the two strands being held together by weak hydrogen bonds as illustrated in figure 7a and 7b. Each nucleotide contains a phosphate group, a 2'-deoxyribose (5 Carbon sugar) and a nitrogenous base. Within the nucleotide, the 5' and 3' carbons are the ones attached to the phosphate group on either side through phosphodiester links. Hydrolysis of phosphodiester bonds can be catalyzed by the action of certain enzymes such as Exonuclease I which are commonly used to cleave or digest DNA base by base. DNA is negatively charged when the ambient pH value is around 7, due to the phosphate groups that make up the DNA backbone. The pK_a of these phosphate groups is near one which gives them a negative charge in aqueous solutions. In dsDNA, the backbone charge is partially neutralized or shielded by counterions in the solution. The net negative backbone charge is what drives DNA migration in an electric field, the basis for DNA electrophoresis.

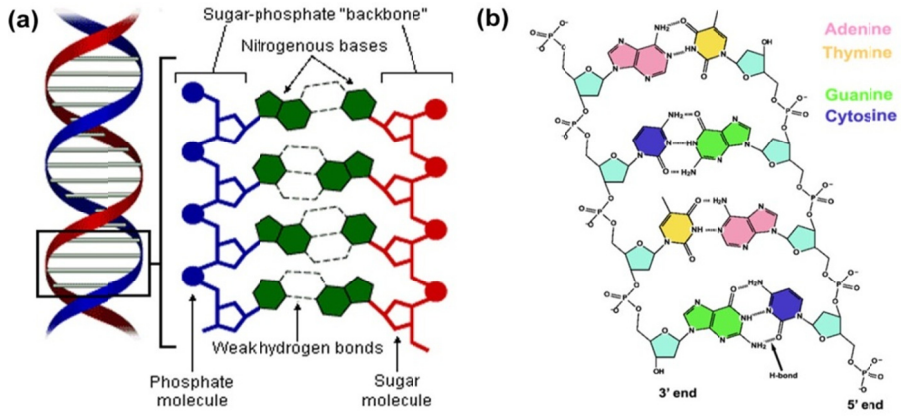

Figure 7 (a) Structure of DNA double helix illustrating the sugar phosphate backbone and hydrogen bonds between bases. (b) Complementary base pairing of dsDNA, adenine paired with thymine and guanine matched with cytosine. dsDNA has a cross-sectional diameter of 2.2 nm.

2.2.3.2 DNA Transport Studies

The first demonstrations of DNA translocation through a solid-state nanopore were shown by Li et al.[56] Deep current blockades were observed as dsDNA was electrophoretically driven through nanopores formed in thin Si_3N_4 membranes using the ion beam sculpting process described earlier in chapter 2. Further studies confirmed the dependence of dsDNA transport kinetics on bias voltage, DNA length and DNA conformation.[24] Li et al. further showed that by reducing the bias voltage by a factor of two, the dwell time of a DNA molecule in the nanopore could be approximately doubled.[24] Multiple configurations of the translocating molecule in the nanopore were also observed in these experiments attributed to dsDNA folding, a phenomenon observed primarily in large nanopores. Smaller ~3 nm pores, however, were shown to restrict the passage of folded molecules and promoted only the linear passage of unfolded molecules. Heng et al. demonstrated that by reducing nanopore diameter to below that of dsDNA, the electrophoretic separation of ssDNA from dsDNA could be achieved using a solid state nanopore.[94] Narrow ~2 nm pores were seen to block the passage of dsDNA, permitting the passage of only ssDNA. Only by applying very high fields was dsDNA permeation through these narrow pores possible, attributed to stretching transitions that occur in dsDNA at forces exceeding 60 pN. Comer et al. further demonstrated that very narrow < 1.6 nm diameter synthetic nanopores could be effectively used to unzip hairpin DNA.[95] Different modes of hairpin DNA transport were observed in these experiments, the first mode referring to the unzipping of the double helix structure to form ssDNA and the second mode referring to the stretching/distortion of the double helix itself.

Chang et al. studied the effect of buffer concentration on DNA translocation dynamics.[96] Current enhancements were observed in large SiO_2 nanopores at low salt concentrations (100mM KCl) as opposed to the typical blockades that were observed at higher salt concentrations. A more rigorous study by Smeets et al. suggested that these current enhancements are due to counterion condensation on the DNA backbone, thereby locally increasing the concentration of counterions in the pore during DNA transport.[73] Current enhancements were observed at concentrations below 0.4 M, a phenomenon that seems localized to only large SiO_2 nanopores. In biological alpha-hemolysin, Benner et al. demonstrated that current blockades were still

observed at low salt concentrations (300mM KCl) during the entry of dsDNA into the lumen of alpha-hemolysin.[97] Current blockades were also observed during the transport of dsDNA through Al_2O_3 nanopores in 100mM KCl salt.[31]

Polymer velocity in the nanopore is also a key topic of interest. Translocation velocities of up to ~30 bases/μs have been reported at relatively low bias voltages in Si_3N_4 nanopores.[28] Chen et al. observed similar translocation velocities in large Al_2O_3 coated Si_3N_4 nanopores estimated at ~27 bases/μs.[25] Such high translocation velocities limit the utility of conventional nanopore technologies in high end DNA sensing and analysis applications including single nucleotide detection. Fologea demonstrated that by increasing electrolyte viscosity using glycerol and by decreasing temperature and bias voltage, an order of magnitude reduction in translocation velocity could be achieved.[28] Remarkably, even with these improvements, the translocation velocities through a solid state nanopore are still more than an order of magnitude faster than that in biological α-hemolysin.[25] Lubensky and Nelson accredited the slow translocation rates in α-hemolysin to strong polymer interactions with the pore walls.[98] Storm showed that the dwell time, τ, of dsDNA molecules in a large ~10 nm SiO_2 nanopore did not scale linearly with polymer length, *L*. In fact, τ scaled according to a simple power law where $\tau \sim L^{1.27}$.[27] This work suggested even with the high translocation velocities observed in nanopore experiments, it may indeed be possible to size long dsDNA using solid-state nanopores in a rapid and label-free manner. In contrast to bulk gel-electrophoresis methods, length separation using solid state nanopores allows each molecule to be screened individually.

The kinetics of DNA transport through solid-state nanopores is also of interest from a polymer physics stand point. Storm suggested that the majority of events in larger nanopores were fast translocation events where the dwell time, t_D, is significantly less than the characteristic relaxation time or *Zimm* time of the polymer.[27] The *Zimm* time, t_Z, is an upper bound on the time taken by a polymer to reach an entropically and sterically favored state. For events where $t_D < t_Z$, the molecule was said to exhibit a *frozen* polymer configuration during transport hindered by only the hydrodynamic drag on the part of the molecule outside the pore.[27] The effects of specific polymer-pore interactions were unaccounted for in these studies. Wanunu et al. discussed the importance of surface interactions on dsDNA transport through Si_3N_4 nanopores.[29]

Studies performed using small 2.7 – 5 nm pores revealed an order of magnitude increase in dwell times as pore diameter was decreased from 5 to 2.7 nm. In addition, strong temperature dependence was observed confirming that surface interactions play an important role in polymer transport.

2.3 Nanopore Applications outside DNA Sequencing

The more immediate application for solid-state nanopores is likely in medical diagnostics. A nanopore based diagnostic tool could (1) detect target molecules at extremely low concentrations from minute sample volumes (perhaps shed DNA from tumor cells in patient serum), (2) simultaneously screen panels of biomarkers/genes (important in diagnosis, monitoring progression and prognosis), (3) provide rapid analysis at relatively low cost and, (4) eliminate cumbersome amplification and conversion steps such as PCR, bisulfite conversion, and Sanger sequencing. MicroRNA (miRNA) expression profiling is one application where solid-state nanopore technology could excel. The detection and accurate quantification of these cancer biomarkers will likely have important clinical implications, facilitating disease diagnosis, staging, progression, prognosis, and treatment response.[99, 100] Wanunu et al. recently demonstrated a nanopore based approach for the detection of specific microRNA sequences enriched from cellular tissue with sensitivities surpassing conventional micro-array technologies (figure 8a).[33] Another exciting prospect is the use of solid-state nanopores for epigenetic analysis, more specifically the detection of aberrant DNA methylation, an early and frequently observed event in carcinogenesis.[38] Hypo- and hypermethylation in the promoter sequences of specific genes serve as both robust cancer biomarkers (e.g. GSTP1 promoter hypermethylation observed in over 90% of prostate cancer cases),[101] as well as indicators of disease severity and metastatic potential in many tumor types.[35, 38] Preliminary progress towards nanopore based methylation analysis has been demonstrated by the Timp and Drndic labs involving the detection of methylated[102] and hydroxymethylated DNA,[103] though this application is still in its infancy.

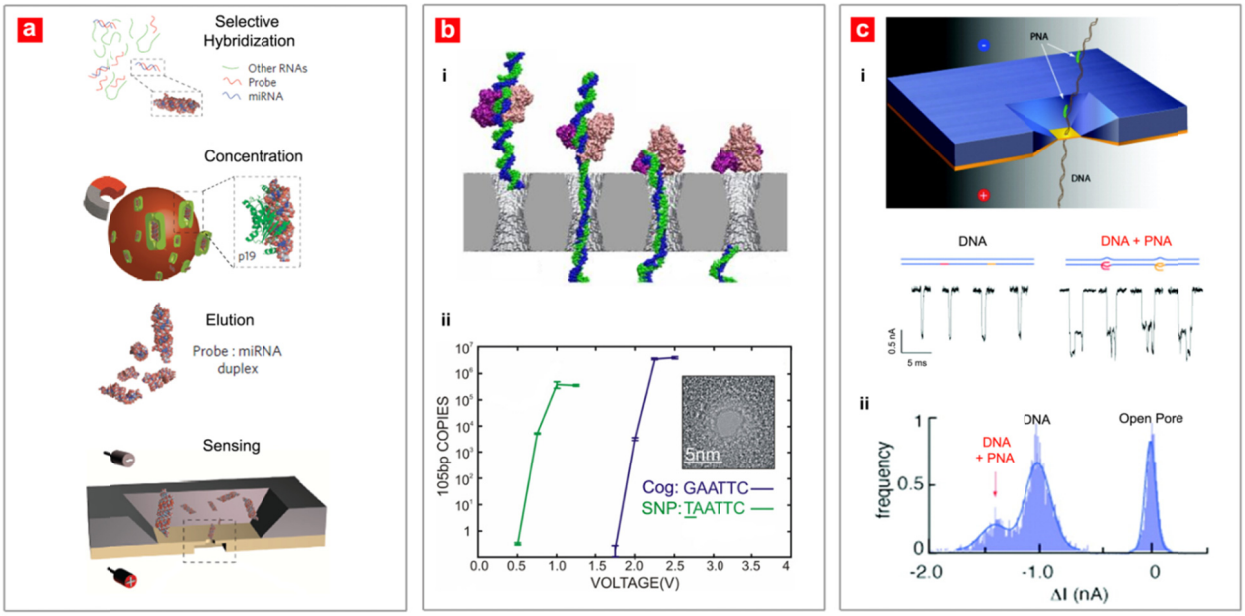

Figure 8 Nanopore applications outside sequencing. (a) Detection of sequence-specific miRNAs from tissue: Probe-specific hybridization used to separate and concentrate specific miRNAs from tissue samples followed by nanopore based quantification. This technique offers enhanced sensitivity over conventional microarray techniques. (b) Detection of SNPs: Protein (EcoR1) bound dsDNA complexes were electrophoretically driven to a ~2nm nanopore and then sheared as shown in i. The introduction of a SNP into the protein binding sequence resulted in a large shift in the shearing threshold voltage as confirmed by quantitative PCR (ii), thereby allowing for the sensitive detection of SNPs. (c) Genotyping and genomic profiling: PNA tagged dsDNA products produced unique current transients in nanopore measurements as shown in i. The number of PNA tags per molecule could be easily quantified, facilitiating rapid electrical profiling of DNA molecules.

Genetic analysis involving the detection of single nucleotide polymorphisms (SNPs) is another important diagnostic application tailored for nanopores. SNPs and point mutations have been linked to a variety of Mendelian diseases such as cystic fibrosis and Huntington's disease as well as more complex disease phenotypes.[104] In proof-of-principle experiments, Zhao and coworkers demonstrated the sensitive detection of SNPs using ~2 nm SiN nanopores (figure 8b).[105] Using the nanopore as a local force actuator, the binding energies of a DNA binding protein and its cognate sequence relative to a SNP sequence could be discriminated. This approach could be extended to screen mutations in the cognate sequences of various DNA binding proteins, including transcription factors, nucleases and histones. The Meller lab, using solid-state nanopores, is actively pursuing another direction: the rapid genotyping of viruses and human

pathogens. An innovative approach involving the introduction of highly invasive peptide nucleic acid (PNA) probes was used to label target genomes with high affinity and sequence specificity, creating local bulges (P-loops) in the molecule (figure 8c).[106] Translocation of this labeled molecule resulted in secondary DNA-PNA blockade levels, effectively barcoding a target genome. While further studies are needed to determine the ultimate spatial resolution of this technique, this methodology could potentially enable the rapid, accurate, and amplification-free identification of small 5-10 kb viral genomes including hepatitis C, dengue and West Nile virus.

2.4 Hybrid Biological/Solid-State Nanopores

A major drawback of solid-state nanopore technology at present is the inability to chemically differentiate analytes of the same approximate size. This lack of chemical specificity can be overcome through surface modification of the pore via the attachment of specific recognition sequences and receptors, in essence forming a hybrid structure. Selective transport through functionalized solid-state nanopore arrays was previously demonstrated by restricting biomolecule passage based on molecular weight,[107] surface charge[108] and polarity.[109] More recently, focus has shifted to the attachment of specific recognition sequences or tethered receptors in the nanopore for target-specific molecular recognition. In drug screening and medicine, such a technique provides a means for label-free, real-time kinetic analysis of biomolecular interactions at the single molecule level including protein-protein, protein-DNA and receptor-ligand interactions. In fact, Lee et al. demonstrated that enantiomeric drug separations could be achieved using an antibody functionalized nanoporous array.[110] Functionalized nanopore channels can also help elucidate the mechanisms driving biological processes, including cell signaling and regulation and protein secretion across cellular membranes. Jovanovic-Talisman demonstrated that functionalized polycarbonate nanoporous arrays can reproduce the selectivity of nuclear pore complexes (NPCs), essential for trafficking specific macromolecules between the cell nucleus and cytoplasm.[111] Proteins referred to as phenylalanine-glycine (FG)-nucleoporins line the walls of these NPCs and facilitate the transient binding and passing of transport factors and their cargo-bound complexes while restricting the passage of proteins that fail to specifically bind to FG-nucleoporins.[112] Using nanopore

channels of the correct dimensions coated with FG-nucleoporins, Jovanovic-Talisman et al. were able to reproduce key features of nucleocytoplasmic transport, selectively discriminating against control proteins in favor of transport factors and transport factor cargo complexes. Kohli demonstrated that selective permeation through synthetic nanoporous membranes could be achieved using DNA hybridization as the selective transport mechanism.[113] In this specific example, a gold nanoporous array was functionalized using hairpin DNA with a thiol substituent at the 5' end allowing it to be covalently attached to the inside walls of the array. The analyte of interest was 18 base long ssDNA which was either a perfect complement to the loop of the hairpin or contained a single base mismatch. Using optical bulk absorbance methods, Kohli demonstrated that single nucleotide polymorphisms could be detected using this chemically modified nanopore platform under optimal conditions.

Various strategies have been implemented to chemically modify solid-state nanopores. Covalent attachment chemistries are generally preferred due to the stability and high packing density of self-assembled monolayers (SAM's) on well prepared surfaces. A very common SAM preparation involves the reaction of molecules with a sulfhydryl termination group (-SH) with Au surfaces to form S-Au attachments to the surface. An extensive review on the formation of SAM's on Au surfaces of varying curvatures is given Love et al.[114] In many cases, however, the surface of the nanopore may be an insulating oxide or nitride (SiO_2, Si_3N_4, Al_2O_3). In these cases a covalent attachment chemistry specific to this insulating surface is required. Liquid phase silane based chemistries are the most commonly used technique to functionalize individual nanopores in such insulating membranes.[84, 115] While these surface chemistries have been characterized in detail on planar surfaces, questions still remain as to the exact packing density, molecular orientation and thickness of SAM's in a highly confined environment that is a nanopore. In addition, nanopores formed via TEM decompositional sputtering processes typically exhibit high surface roughness, high surface curvature and a non-stoichiometric material composition due to selective material sputtering, as observed in SiO_2 and Si_3N_4 nanopores,[78, 116] further complicating the nanopore functionalization process. In these cases it is vital to thoroughly oxidize the surface through an extensive O_2 plasma treatment or a liquid based treatment in 1:3 H_2O_2:H_2SO_4. Using such a process, Wanunu and Meller showed significant changes in the pH response of Si_3N_4 nanopores functionalized with various amine

terminated silane chemistries.[84] Ionic conductance measurements were used to monitor in-situ the formation of the SAM in the nanopore and to calculate the thickness of the molecular layer directly attached to the internal surface of nanopore. The calculated values suggested the upright orientation of the attached molecules on the nanopore surface. Note that, in this specific example, the entire membrane containing the nanopore was functionalized with the silane chemistry.

For certain applications, however, it may be desirable to functionalize only the nanopore region itself. For example, in applications where the analyte of interest is present only at very low concentrations, a functionalized membrane may reduce the detection limits of the nanopore due to delocalized binding events on the membrane surface between immobilized receptors and the target species that do not translate to detectable changes in the output signal.[117] In addition, receptors immobilized on the membrane may also modulate the conductance of the nanopore even in the absence of the target species. Hofler et al. showed via coarse-grained molecular dynamics simulations that DNA anchored on the membrane surface can electrically gate the nanopore if bound sufficiently close to the pore opening.[118] Thus a localized nanopore functionalization process is expected to be extremely useful. One such method involves the localized deposition of a tetraethylorthosilicate (TEOS) based oxide ring around the nanopore.[115] A focused ion beam was used to decompose the TEOS precursor near the Si nanopore surface, thereby reducing the diameter of the pore to a final diameter of between 25 and 30 nm. DNA probes were immobilized in the nanopore via a silane based chemistry thereby introducing local chemical functionality at the entrance of the nanopore without functionalizing the remainder of the membrane. SAM coatings may also help to reduce the speed of polymer translocation through nanopores. Kim et al. derivatized Al_2O_3 nanopore surfaces with aminopropyltriethoxysilane (APTES) resulting in a positively charged surface in pH 6.0 buffer, attractive to anionic dsDNA.[119] The resulting strong electrostatic polymer-pore interactions enabled the detection of short dsDNA molecules, typically under the detection limits of conventional solid state nanopore sensors.

Chemical functionalization and its effect on the electrical properties of polymer nanopores was previously reported by Siwy and Howorka.[120] More recently, the impact of surface functionalization on the translocation dynamics of ssDNA through solid-state nanopores was

demonstrated.[121] A DNA hairpin functionalized SiO_2 nanopore showed higher flux and smaller translocation times for the passage of perfect complementary (PC) ssDNA versus single base mismatch probes (1MM), a highly sensitive strategy for the detection of SNPs. Altering the surface chemistry of a pore can also facilitate the sensitive detection of proteins. Drawing inspiration from the lipid coated olfactory sensilla of insect antennae, the Mayer lab recently demonstrated the identification of proteins using fluid lipid bilayer coated SiN nanopores.[122] The incorporation of mobile ligands in the bilayer coating introduced chemical specificity into the pore, slowed the translocation of target proteins, prevented pores from clogging and eliminated non-specific binding, thereby resolving many issues inherent to solid-state nanopores. A lipid bilayer coated nanopore architecture (in either SiN[122] or Al_2O_3[123]) also permits future integration with biological nanopores to form robust nanopore sequencing elements.

The concept of a hybrid biological solid-state nanopore was recently advanced by Dekker and co-workers, through the direct insertion of genetically engineered α-hemolysin into 2.4-3.6 nm diameter SiN nanopores.[124] A simple yet elegant strategy was devised to control the orientation of α-hemolysin in the solid-state pore. By chemically linking a long dsDNA tail to α-hemolysin as shown in figure 9c, the entry of this engineered α-hemolysin channel into a SiN nanopore could be electrophoretically guided to form a coaxially aligned structure. Hybrid pore conductance and ssDNA translocation event durations were in good agreement with α-hemolysin embedded in lipid bilayers.[51] Interestingly, ssDNA blockage amplitudes through hybrid pores were significantly less than in α-hemolysin-bilayer systems, attributed to leakage currents around the body of the protein pore. Also, significant electrical noise was observed in hybrid structures. These parameters will likely need to be optimized in order to match the single nucleotide sensitivity of aminocyclodextrin modified α-hemolysin.[8] Nevertheless, this hybrid architecture opens up the exciting possibility of high throughput sequencing by coupling the single nucleotide recognition capabilities of either α-hemolysin or *MspA*, with wafer-scale arrays of individually addressed solid-state nanopores.

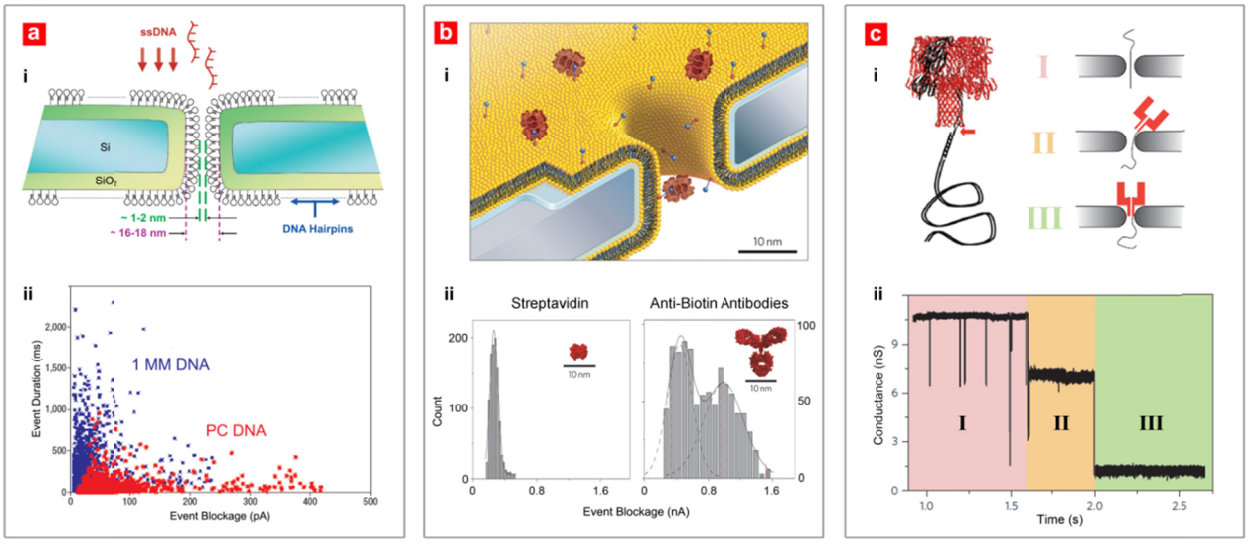

Figure 9 Hybrid biological solid-state nanopores. (a) Hairpin DNA functionalized SiO_2 nanopores. ii. The translocation of perfect complementary ssDNA (complementary to the hairpin sequence) versus a single base mis-match sequence (1MM) resulted in a bimodal distribution as shown, thereby allowing for the sensitive detection of SNPs. (b) Lipid bilayer coated SiN nanopores with fluid lipid side walls function as highly sensitive protein detection elements. ii. Current blockage histograms could be used to detect and differentiate various protein analytes using this surface functionalized nanopore. (c) Direct insertion of α-hemolysin into a SiN pore. i. Schematic of α-hemolysin chemically modified with a dsDNA tail. ii. The three stages of hybrid pore formation are shown, finally resulting in a conductance level (III) consistent with α-hemolysin in a lipid bilayer.

Nanopore Platform Development 3

Understanding the biophysics of single molecule transport through solid-state nanopores is of fundamental importance in working towards the goal of DNA detection and genome sequencing using nanopore based sensors. Though solid-state nanopore technology shows much promise, the development of robust, reusable nanopore sensors that operate with the selectivity and elegance of biological nanopore systems still remains an elusive goal. At present, fabrication challenges (stress induced membrane deformation and mechanical failure in SiO_2 structures),[96] limited nanopore lifetime, electrical noise[89, 90] and a lack of chemical specificity, limit the feasibility of solid-state nanopore technology in high end applications such as single nucleotide detection and DNA sequencing. Thus, there is a need for highly sensitive, mechanically robust nanopore sensors with well-defined surface charge properties for the detection of specific biological molecules (ssDNA, dsDNA, mRNA).

3.1 SiO_2 Nanopore Fabrication

Our initial nanopore fabrication process involved first forming free-standing Si membranes (1500-2200 Å in thickness, cross sectional area of 60 x 60 μm^2) in silicon-on-insulator wafers using optical lithography and tetra methyl ammonium hydroxide wet etch processes.[96] Next, ~80 nm holes were formed in these pure 100 Si membranes using a focused ion beam with beam current set to 10 pA and a spot size of 10 nm. Examples of nanopores formed using this FIB based milling process are illustrated in figure 10. The ion milling process was monitored in real time using the end point monitor on the FIB tool; a sudden drop in the specimen current signified beam *punch-through*.

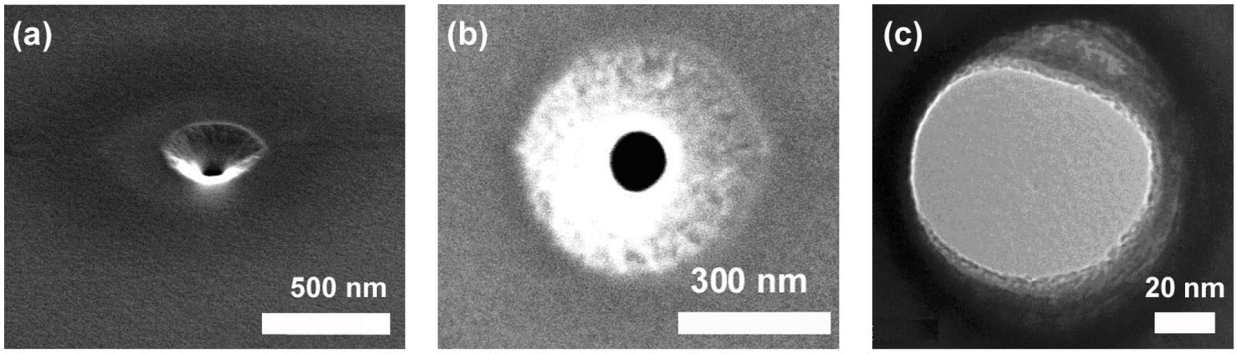

Figure 10 Nanopores formed using the FIB process in 100 Si membranes. (a) Tilted SEM image of a ~80 nm pore. (b) SEM image of a ~80 nm pore. (c) TEM image of a FIB formed nanopore.

After milling, sub-40nm diameter nanopores were formed through wet oxidation of the Si membrane containing the nanopore. The wet oxidation process was conducted at 900˚C for 20 - 25 minutes resulting in the growth of an oxide of approximate thickness ~ 600 Å. The oxidized nanopores were shrunk to size using the electron beam induced oxide reflow process documented in chapter 2. The temporal contraction of a ~40 nm nanopore is illustrated in figure 11. The low intensity electron beam locally fluidizes the oxide around the nanopore resulting in material reflow into the pore region. A final nanopore diameter of ~10 nm was obtained using this process and was well suited for bio-sensing experiments. Upon removal of the electron beam, nanopores retained their shape and size.

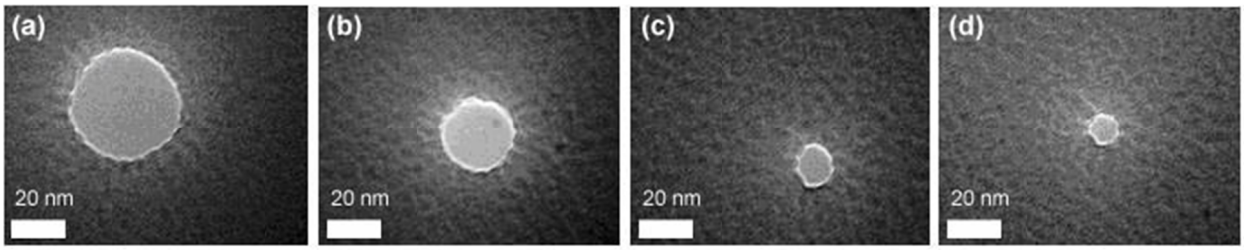

Figure 11 Temporal contraction of a SiO_2 nanopore using the electron beam induced oxide reflow process in the TEM. TEM image of the pore at time (a) t = 0 min, (b) t = 10 min, (c) t = 20 min, (d) t = 30 min.

Fabrication Challenges: The main drawback associated with the SiO_2 nanopore formation process outlined in figures 10 and 11 is low yield. Surface-tension-driven contraction is known

to occur when the pore radius, r, is less than half the membrane thickness, h (i.e. $r < h/2$).[65] Tailoring the pore radius to exploit this TEM based shrinking phenomena has proven to be very challenging due to the variability in pore diameter obtained using the FIB tool. The ion beam is focused several millimeters away from the edge of the membrane region to prevent damaging/milling the thin Si membrane during the ion beam focusing procedure. Traversing the beam to the membrane center often introduced a slight defocusing effect and in turn affected pore reproducibility. Due to these factors, pores are at times milled with radii greater than the critical radius, resulting in pores that expand rather than contract during TEM observation.

Oxidation is also a critical step that precedes TEM based shrinking. Pores underwent wet oxidation at 900ºC for 20-25 minutes. This oxide layer acts as an insulating barrier shielding the electrolyte solution from the underlying conductive Si surface in DNA translocation experiments. Tilted SEM images of Si membranes after oxidation are illustrated in figures 12a and 12b. Membrane buckling is clearly evident in these images (4μm vertical displacement over a 60 μm span), suggesting that significant compressive stress is present in these thermally grown SiO_2 membranes. The result is extremely fragile, highly stressed membranes that frequently rupture. Fitch et al. studied the intrinsic stress and strain in thin films of SiO_2 prepared by the thermal oxidation of crystalline silicon[125] and concluded that large intrinsic stress gradients exist in the layers of SiO_2 in the vicinity of the Si/SiO_2 interface. The residual intrinsic interfacial stress was calculated at 460 MPa and was independent of the growth temperature. This intrinsic stress was the result of mismatches in the molar volumes of Si and SiO_2 at the interface. It was observed that overall compressive stress increases with decreasing temperature as shown in figure 12c. Thus, the buckling seen in our membranes is understandable and highlights the need for a low stress film deposition process. An Al_2O_3 membrane system, deposited using atomic layer deposition (ALD), is one of the options that we explored.

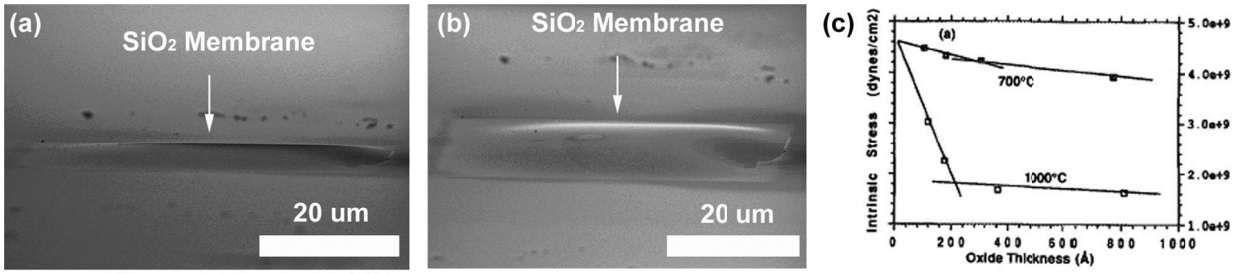

Figure 12 SEM images of SiO_2 membrane region after oxidation shown at tilt angles of (a) 5° and (b) 10°. Wet oxidation induces membrane buckling due to high compressive stress in the grown film. 4 μm vertical displacement was observed over the 60 μm membrane span. (c) Intrinsic compressive stress in Si/SiO_2 films at different oxidation temperatures.[125]

3.2 Al_2O_3 Nanopores

3.2.1 Nanopore Fabrication

To overcome these limitations, we devised a new process for forming Al_2O_3 nanopores. The following sections report the development and characterization of a new solid-state nanopore sensor for the detection of single DNA molecules. The Al_2O_3 structures reported here exhibit enhanced mechanical properties (increased hardness, decreased stress) and improved electrical performance (low noise, high signal-to-noise ratio) over their SiO_2 and Si_3N_4 counterparts. The fabrication process described results in high device yield and a ten-fold reduction in process time/complexity relative to techniques demonstrated previously in SiO_2. High temperature process steps, wet etch steps, FIB and electron beam lithography (EBL) were eliminated. Al_2O_3 nanopore sensors fabricated using this process have all the advantages of existing SiO_2 and Si_3N_4 architectures (size control with sub-nanometer precision, controlled contraction/expansion, chemical modification with biomolecules) but also exhibit superior noise performance over their solid-state counterparts. Interestingly, the formation of nanopores in Al_2O_3 membranes resulted in the localized crystallization and facetted grain growth of hexagonal γ-Al_2O_3 nanocrystallites in the vicinity of the pore, attributed to nanoscale thermal annealing and electron beam assisted diffusion. This phenomenon has not been reported in Si_3N_4 and SiO_2 topologies and could potentially enhance the mechanical hardness and localized structure of the nanopore. Bulk membrane properties (crystallinity, composition and thickness) were studied using TEM, X-ray

photoelectron spectroscopy (XPS) and Auger electron spectroscopy (AES). A 3D symmetric double cone structure for the nanopore was extracted from conductance measurements, supported by thickness mappings constructed using energy filtering transmission electron microscope (EFTEM) methods. The high frequency (f > 10 kHz) noise performance of Al_2O_3 nanopores shows an order of magnitude improvement over existing Si_3N_4 structures,[15] resulting in high sensitivity and exceptional signal-to-noise performance. Finally, the functionality of these Al_2O_3 nanopore sensors is demonstrated through the detection of 5 kbp dsDNA in 1 M KCl by monitoring biomolecule transport under an applied bias.

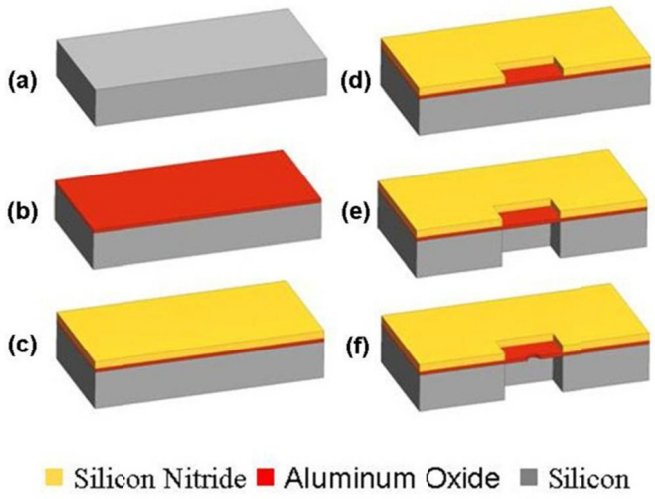

Figure 13 Process flow for the formation of Al_2O_3 nanopores. (a) Start with double-side polished 300 μm thick silicon wafer. (b) Deposit 70 nm of Al_2O_3 by ALD. (c) Deposit 500 nm low stress SiN using PECVD process. (d) Pattern 30 x 30 μm windows on the wafer front side via optical lithography and RIE. (e) Pattern 30 x 30 μm windows on the wafer backside and etch using DRIE ($SF_6 + O_2$) and stop on the Al_2O_3 layer creating a membrane. (f) Use a tightly focused electron beam to form the nanopore.[30]

The process flow for the fabrication of Al_2O_3 nanopores is outlined in figure 13. A detailed description is provided in Appendix 1. Atomic layer deposition (ALD) was used to deposit 700 Å of Al_2O_3, confirmed using single wavelength and spectroscopic ellipsometry. The self-limiting growth characteristic of ALD enables excellent uniformity over large areas, accurate control of film composition and thickness, conformal coating and high reproducibility making it ideal for membrane applications.[126] Plasma enhanced chemical vapor deposition (PECVD) was next

used to deposit 500 nm of low stress silicon nitride (SiN) as a passivation layer to help reduce device capacitance and electrical noise. Optical lithography and RIE were used to pattern 30 μm square membrane regions. A CF_4 based etch recipe yielded very high SiN:Al_2O_3 etch selectivity (60:1). 300 μm deep, high aspect ratio (10:1) Si trenches were next formed on the wafer back side using the Bosch process (deep reactive ion etching tool), with very high etch selectivity to Al_2O_3 (Si:Al_2O_3 of 3000:1)[127, 128] as shown in figure 14a.

Even with a significant over-etch in the DRIE, less than 10 nm of Al_2O_3 was removed resulting in a final membrane thickness of 60 nm. Nanopores of varying diameter (1 nm to 16 nm) were formed in free-standing Al_2O_3 membranes using a tightly focused electron beam from a JEOL 2010F field emission gun transmission electron microscope (FEG-TEM) operated at 200kV. Decompositional sputtering has been demonstrated in SiO_2[129] and Si_3N_4[71, 81] membranes but has not previously been reported in Al_2O_3 material systems. The precise thickness control and the high etch selectivities achieved using this fabrication process can potentially allow for the formation of ultra-thin membranes (thickness < 100 A). This is particularly useful in forming a solid state analog to the lipid bilayer (thickness ≈ 4-5 nm),[44] an important tool in better understanding the kinetics governing biomolecule transport through proteinaceous pores in cellular membranes. Our low temperature fabrication process is also compatible with metallization steps and is applicable to the formation of metal-oxide-semiconductor (MOS) capacitors. Simulation work by Gracheva et al.[16] on nanopores formed in MOS capacitors with thin SiO_2 membranes (< 5 nm) reported the possibility of single nucleotide resolution with potential application to next generation DNA sequencing systems. This fabrication technique could help enable the possible realization of such structures.

Mechanical stress in the fabricated structures was calculated using Stoney's law.[130] Thermal annealing at 500˚C (30 minutes) was performed to help relax residual tensile film stress and to improve characteristic film strength.[131] Annealing temperatures were kept well below 800˚C, the transition temperature at which sharp increases in film stress were observed for t_{film} > 60 nm, attributed to phase transitions from the amorphous to the polycrystalline state.[130] Katamreddy demonstrated that annealing ALD alumina films at 600ºC did not significantly change the amorphous properties of the film.[132] The amorphous structure of these Al_2O_3 membranes after

annealing was confirmed by TEM electron diffraction imaging. A low tensile film stress of 148 ± 20 MPa was measured for the composite Al_2O_3/SiN film stack. Figure 14b is a tilted SEM image of a 30 μm square Al_2O_3 membrane at a tilt angle of 5˚ surrounded by a 500 nm thick low stress SiN support layer, imaged using the Hitachi S-4800 SEM. The low tensile film stress results in a flat, mechanically hard membrane region. Figure 14c is a tilted SEM image of a SiO_2 membrane tilted by 5˚ after oxidation. The image illustrates high compressive stress as previously discussed, resulting from the thermal oxidation process. Thermally induced compressive stress resulted in mechanically brittle SiO_2 membranes that were prone to frequent rupture/failure during DNA translocation experiments, nanopore functionalization and nanopore cleaning processes. Al_2O_3 membranes were mechanically more robust then their SiO_2 counterparts.

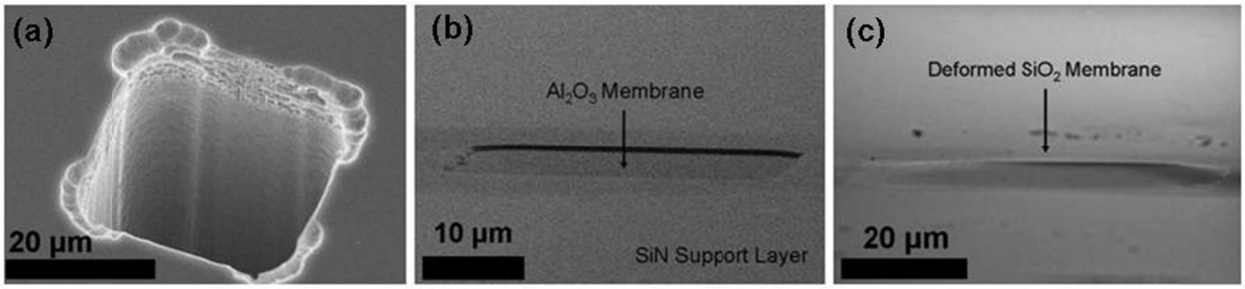

Figure 14 (a) SEM image of the backside trench formed using DRIE. (b) Tilted SEM image (5˚ tilt) of Al_2O_3 membrane with supporting SiN layer. Membrane is under low tensile stress and appears flat. (c) Tilted SEM image (5˚ tilt) of SiO_2 membrane post oxidation showing ~ 4 μm vertical deflection over 60 μm span due to high compressive stress. Membrane is significantly deformed resulting in frequent failure.[30]

Bulk membrane composition was determined using X-ray photoelectron spectroscopy (XPS). Strong peaks were seen at binding energies corresponding with core electron ejections from Al 2s, Al 2p, O 1s and O 2s orbitals, suggesting that the deposited film contained only Al and O. Ar peaks were attributed to Ar based sputtering to remove surface carbon contamination prior to analysis. Compositional analysis revealed 37% Al and 63% O, in good agreement with the expected stoichiometric film ratio of 40% Al and 60% O (Al_2O_3). The XPS spectrum is illustrated in Figure 15a. Auger electron spectroscopy (AES) was also used to confirm membrane composition and thickness. The inset of figure 15a is an Auger differential spectrum showing strong peaks at kinetic energies of 1378 eV and 503 eV associated with *kll* shell transitions for

Al and O in the compound Al_2O_3 form. Auger results confirm that all residual Si and SiN in the membrane regions were removed by RIE and DRIE processes. This eliminates the possibility that the observed pore crystallinity is the result of unetched, residual Si nanocrystals in the vicinity of the pore. Membrane depth profiling involving decompositional sputtering and in-situ Auger analysis was next done to estimate membrane thickness. 17 Å of material was removed per sputtering cycle using an Ar ion beam, followed by Auger point mode analysis on the membrane region. Peak intensities associated with *kll* transitions for Al, O, N (378 eV) and *lmm* transitions for Si (92 eV) were measured. Figure 15b illustrates the results of depth profiling. The peak intensities for Si and N are negligible at the collection spot suggesting the absence of Si and N in or on the membrane. The peak intensities for elemental Al and O are initially very high but decay rapidly to zero after 35 cycles corresponding to a sputter depth/membrane thickness of 60 ± 2nm. XPS and AES therefore confirmed the thickness and composition of the membranes in which individual Al_2O_3 nanopores were successfully formed.

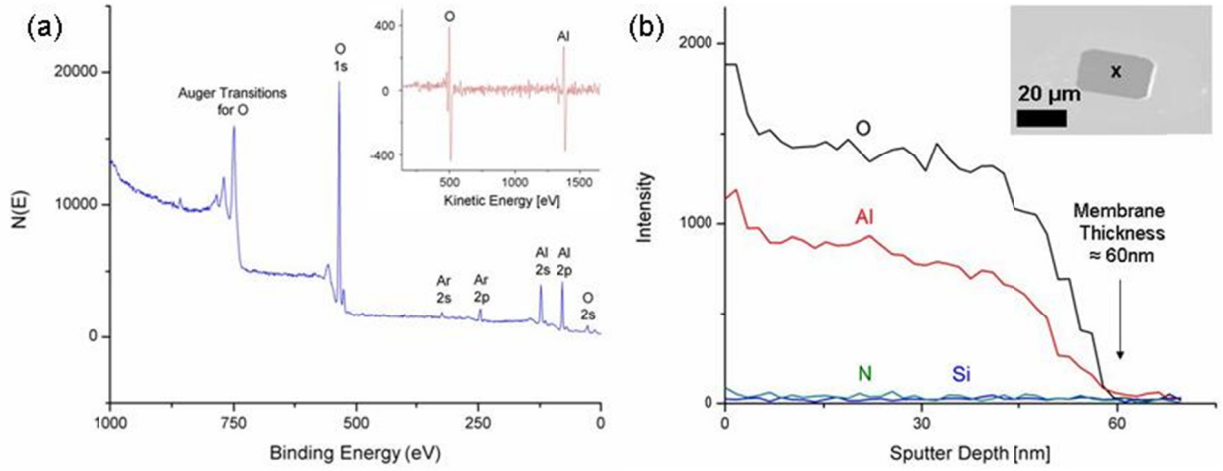

Figure 15 (a) XPS results on Al_2O_3 films. (Inset) Auger differential spectra of membrane region after release illustrating presence of only Al and O. (b) Depth profiling using AES to extract membrane thickness of 60 ± 2 nm. (Inset) Tilted SEM image of membrane with marked region indicating Auger electron collection region.[30]

Nanopores were formed in these thin Al_2O_3 membranes using the electron beam induced sputtering process documented in chapter 2. Nanopore contraction kinetics depended on initial pore diameter, d_{pore}, membrane thickness, *h,* and electron beam intensity. Nanopore contraction was consistently observed upon defocusing the electron beam to an intensity of ~10^6 e-nm^{-2} for

$d_{pore} < h$. Figures 16a-d show a series of high resolution TEM (HRTEM) phase contrast images illustrating the temporal contraction of an Al_2O_3 nanopore from an initial diameter of 4 nm to a final diameter of 1 nm. The shot noise in the pore region confirms that the electron beam has completely sputtered through the membrane. The pore quenches in size upon removal of the electron beam. This technique thereby allows for precise tunability and nanometer control over pore dimensions in Al_2O_3 membranes. In SiO_2 and Si_3N_4 material systems, nanopore contraction is attributed to thermal decomposition and surface tension driven reflow of the amorphous material surrounding the pore.[129] Crystallinity is not observed after pore formation as confirmed by the fast Fourier transform (FFT) of a 4 nm Si_3N_4 nanopore (figure 16f). In contrast, polycrystalline regions are clearly evident after the formation of Al_2O_3 nanopores. Facetted grain growth and the formation of 5-10nm hexagonal nanocrystallites (i,ii,iii,iv) in the vicinity of Al_2O_3 pores are seen in HRTEM images figures 16g and pairs of diffraction spots are clearly visible in the corresponding FFT (figure 16h).

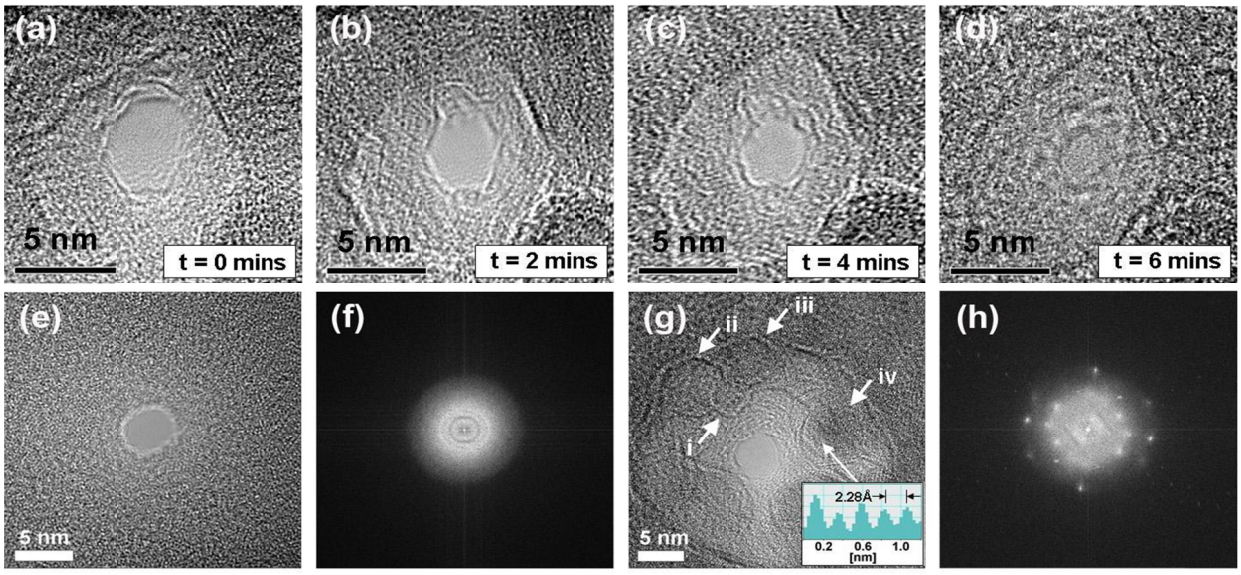

Figure 16 (a)-(d) TEM phase contrast images illustrating temporal contraction of an Al_2O_3 nanopore from an initial pore size of ~ 4 nm to a final pore size of ~ 1 nm. (e) TEM phase contrast image of 4nm SiN pore. (f) Corresponding FFT showing amorphous structure of SiN pore. (g) TEM phase contrast image of a 4 nm Al_2O_3 pore. Hexagonal Al_2O_3 nanocrystallites are shown by i,ii,iii,iv. iv is partially aligned with the zone axis with 2.28 Å atomic spacing corresponding to γ-Al_2O_3 in its <222> crystal orientation. (h) Corresponding FFT showing polycrystalline structure of the pore.[30]

The hexagonal nanocrystallites labeled i,ii,iii are not oriented with the zone axis and thus crystal periodicity is not observed. In contrast, the nanocrystallite labeled iv shows regions of periodicity and clear lattice structure due to its partial alignment with the zone axis. Further examination of these regions revealed a lattice spacing of 2.28 Å (see electron intensity plot in inset of figure 16g) corresponding to γ-Al_2O_3 in its <111> crystal orientation. The damage mechanism in alumina during pore formation is attributed to the Knotek-Feibelman oxygen ion desorption mechanism.[133, 134] Oxygen is preferentially desorbed from the surface by core-level ionization processes during electron irradiation, forming high Al content regions and facetted metal Al clusters in the vicinity of the pore.[135] In ultra-high vacuum environments, the reoxidation of these facets is quenched allowing reactive aluminum to remain in its metallic state, thereby forming stable Al crystals. Metallic Al has a lattice spacing of 2.33 Å in its <111> crystal form. In low vacuum environments, however, as observed in these experiments, the high reactivity of metallic aluminum combined with chamber contamination (molecular oxygen and hydrocarbons) results in reoxidation and the formation of γ-Al_2O_3 nanocrystallites.[134] The nucleation and growth of γ-Al_2O_3 nanocrystallites is likely due to a combination of thermal annealing and electron beam assisted diffusion processes. Al_2O_3 nanocrystallites in the more thermostable α phase (corundum) were not observed. Zywitzki et al. showed that intense ion bombardment can hinder the nucleation of the α phase.[136] Therefore, it is plausible that the use of a high energy, tightly focused electron beam may also hinder α phase nucleation in Al_2O_3 thin films. The presence of γ phase nanocrystallites significantly enhances the mechanical hardness of the local pore region with hardness values expected to range between 20-22 GPa.[136] This is significantly higher than the mechanical hardness of amorphous SiO_2 and Si_3N_4 pores, thus resulting in mechanically stable Al_2O_3 nanopore sensors suitable for a variety of applications.

3.2.2 Fabrication of Al_2O_3 Nanopore Arrays

Nanopore arrays can also be formed in thin, mechanically robust Al_2O_3 membranes using FIB based milling processes. Arrays were formed using a FEI DB235 FIB system at an accelerating potential of 30 keV and 10 pA beam current. Figures 17a and 17b show ~200 nm diameter

nanopore arrays with 1 μm pitch, formed in ~ 45 nm thick Al_2O_3 membranes using a FIB tool employing a high energy Ga^+ beam. This process can be used to achieve pore diameters as low as ~50 nm by controlling the ion dose, accelerating potential and beam current. Figure 17c is an AFM image of a single ~200 nm Al_2O_3 nanopore formed using the FIB milling process.

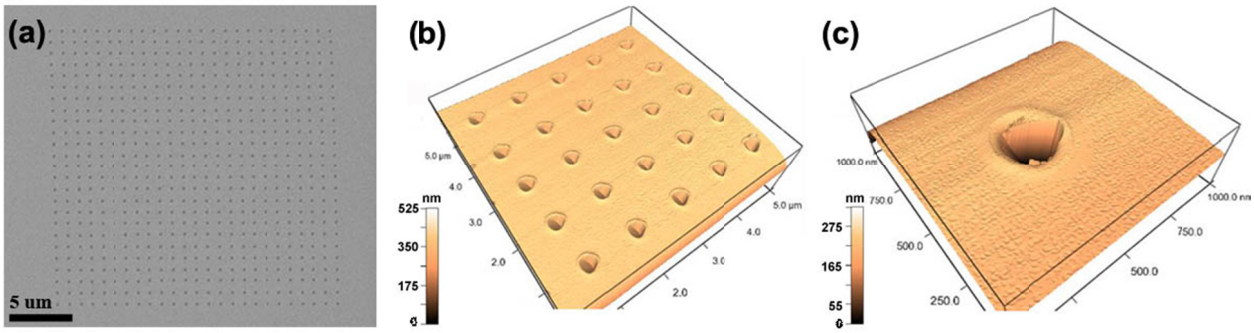

Figure 17 (a) 25 x 25 array of ~200 nm nanopores formed in free-standing Al_2O_3 membranes using FIB based milling. (b) AFM image of a 5 x 5 array of ~200 nm nanopores. (c) AFM of a single ~200 nm nanopore formed using the FIB milling process.

3.2.3 Electrical Characterization of Al_2O_3 Nanopores

The electrical conductance, *G*, of individual nanopores formed using the electron beam induced sputtering process were measured using current-voltage (IV) measurements at different ionic concentrations, typically 10 mM, 100 mM and 1 M KCl. Linear IV characteristics were seen at each of these molarities in 11 nm diameter pores as illustrated in figure 18a. *G* scaled linearly at high salt concentrations (≥ 100 mM), as expected, and current rectification was not seen in voltage sweeps suggesting that pore geometry is symmetric. To further probe the performance of Al_2O_3 nanopores in electrolyte, the conductance of 11 different nanopores of varying diameter (4 nm to 16 nm) were measured in 1 M KCl as shown in figure 18b. Two geometric models were proposed to fit *G*.[70, 73] The effects of surface charge were neglected in these models as the Debye screening length given by $\kappa^{-1} << d_{pore}$ (where $\kappa^2 = 2e^2 n_{KCl}/k_B T \varepsilon \varepsilon_o$ in 1 M KCl). At these high salt concentrations, charge carriers in the bulk were expected to dominate current flow.

Electroosmotic flows resulting from counterion condensation on the charged pore surface should be negligible. The first model[73] assumed a purely cylindrical channel of length L_{pore} = 60 nm with a cross sectional diameter equal to the pore diameter, d_{pore} (blue curve of figure 18b). The second conductance model assumed a double cone structure and accounted for cone angle, α, and effective channel length, h_{eff}.[70] Assuming $\alpha = 30^{\circ}$ and $h_{eff} = h/3$,[70] an upper conductance bound can be derived (red curve of figure 18b). Applying a least squares fit to the measured data (black curve of figure 18b), an effective length of $h_{eff} \approx 26.5$ nm and cone angle of $\alpha \approx 24^{\circ}$ were extracted for Al_2O_3 pores, suggesting a double cone structure. Plasmon imaging using EFTEM confirmed this finding. Plasmons are low energy loss events (< 50 eV) occurring due to the longitudinal wave-like oscillations of weakly bound electrons. Most materials produce broad (≈ 20 eV) plasmon peaks and this low loss region of the energy loss spectrum is sensitive to specimen thickness.[137] Plasmon imaging of the pore region was conducted using a JEOL 2010F TEM equipped with a post-column imaging filter (GIF by Gatan). A low-loss alumina plasmon peak centered at 30 eV was identified using electron energy loss spectroscopy (EELS). The relative thickness profiles of numerous pores were formed by plasmon imaging using an energy loss of 30 eV, energy slit width of 20 eV at an energy resolution of 1 eV. A plasmon image of an 11.1 nm pore is illustrated in the left inset of figure 18b.

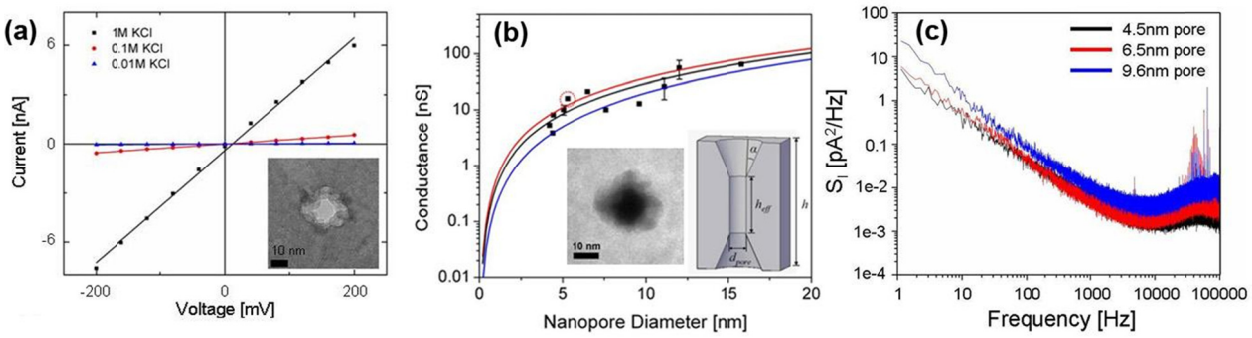

Figure 18 (a) Current-voltage (IV) characteristics of an 11.1 nm diameter pore measured in 10 mM KCl, 100 mM KCl and 1 M KCl. Linear IV characteristics suggest symmetric pore geometry. (b) Pore conductance of 11 nanopores ranging in diameter from 4 nm to 16 nm. Red and blue lines represent conductance models from literature. Black line is a least squares fit to the measured data. Predicted geometry of pore from conductance measurements. (Left Inset) Thickness mapping of an 11.1 nm pore constructed using EFTEM. (c) Power spectra of 3 different Al_2O_3 nanopores in 1 M KCl at 120 mV. Spectral components at high frequencies (f > 1 kHz) are significantly attenuated relative to Si_3N_4 and SiO_2 systems.[30]

This thickness dependent mapping shows a tapering towards the pore center which appears dark as electrons traversing the center of the pore undergo minimal inelastic scattering events (corresponds to zero loss peak in EELS spectra). In contrast, thick regions induce more inelastic scattering, appearing light in the EFTEM image. Assuming the pore is symmetric based on IV characteristics, the thickness tapering observed strongly suggests an angled double cone structure. Note in particular that pore geometry and conductance are heavily dependent on material systems, membrane thicknesses and TEM sputtering conditions (spot size and electron dose) as observed by Ho et al. and Smeets et al., extracting a wide range of cone angles (10˚ in 10 nm thick Si_3N_4 pores[81] and 45˚ in 60 nm SiO_2/SiN/SiO_2 stacks[73]) for different topologies.

The high frequency noise performance of Al_2O_3 nanopores shows significant improvements over existing Si_3N_4 technologies. Noise power spectra (1 M KCl, 120 mV) for three Al_2O_3 nanopores of varying diameter (4.5 nm, 6.5 nm, 9.6 nm) are shown in Figure 18c. The low frequency noise performance of these nanopores is consistent with that observed in Al_2O_3 coated Si_3N_4 structures.[93] 1/f noise reduction in Al_2O_3 coated structures relative to Si_3N_4 nanopores was attributed to the passivation of non-ideal surface properties including surface charge.[93] The process reported here allows for the fabrication of low 1/f noise structures in a simple and highly integrated manner. More importantly, high frequency (f >10 kHz) spectral noise components were attenuated by an order of magnitude relative to Si_3N_4 and Al_2O_3 coated Si_3N_4 structures.[89, 93] The noise performance is on par with the state of the art in Si_3N_4 technology reported by Tabard-Cossa et al.[90] Noise reduction was attributed to a decrease in device capacitance (measured at 20 ± 5 pF, as compared to device capacitance in Si_3N_4 structures, which were measured in excess of 300 pF[89]), a direct advantage of our reported fabrication process. The result is decreased high frequency noise, high signal-to-noise ratio and enhanced sensitivity during DNA translocation experiments. Further enhancements to noise performance could be achieved through device optimization coupled with fluidic isolation techniques using PDMS.[90] Noise reduction and characterization is the subject of a future publication. With ongoing research in the reduction of 1/f flicker noise through surface passivation techniques, the possibility of single base resolution using solid state nanopores could become a reality. Coupled with

techniques for imparting chemical selectivity in the nanopore, this could be the first step towards a nanopore based sequencing device.

3.2.4 Preliminary DNA Transport Studies

To demonstrate the functionality of Al_2O_3 nanopores as biomolecule sensors, dsDNA translocation experiments were performed using 5kbp dsDNA through 5-5.5 nm diameter nanopores in 1 M KCl at 500 mV. Open pore conductance was measured through a series of I-V sweeps prior to the introduction of dsDNA and results were in good agreement with the proposed conductance model. No translocation events/current blockades were seen prior to the introduction of dsDNA as shown by the negative control experiment (left inset of figure 19a). Upon introduction of 5 kbp dsDNA at a concentration of 6 nM into the *cis* chamber, deep current blockades were observed with excellent signal-to-noise ratio. Figure 16a shows unadjusted current blockade data low-pass filtered at 100 kHz. The right inset of figure 19a represents a typical event observed during translocation experiments. The event dwell-time, t_D, the open pore current, i_o, and the blocked pore current level, i_b, are all indicated in the inset. Blockage ratio, B_r, as a function of the cross sectional diameter of B-form dsDNA (d_{DNA} = 2.2 nm) and pore diameter is given by equation 1.

$$B_r(d_{pore}) = \left(\frac{d_{DNA}}{d_{pore}} \right)^2 \tag{2}$$

Measured blockage ratios, $B_r = i_b/i_o$, versus event dwell-times for n = 1178 events are plotted in figure 19b. A single blockade level is observed, $B_r = 0.20 \pm 0.04$, with a mode value of 0.17. The results are in excellent agreement with simple geometric arguments that predict $B_r = 0.17$ (17% of open pore current blocked) for dsDNA translocating through a 5.3 nm pore.

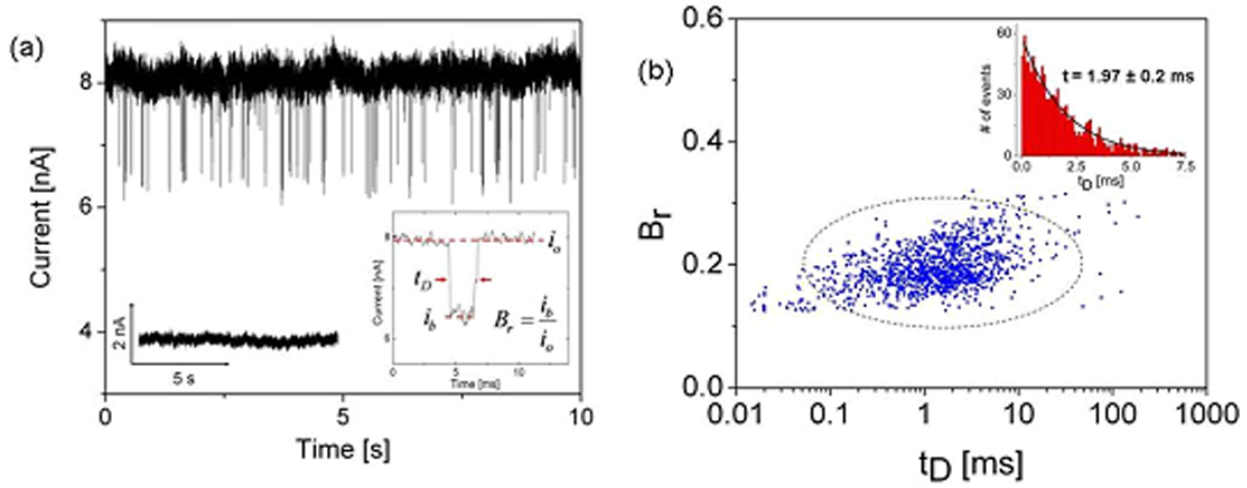

Figure 19 (a) Typical current blockades seen in a 5.3 nm Al_2O_3 pore after the addition of 5 kbp dsDNA at a concentration of 6 nM at 500 mV. (Left Inset) Negative control: pore current prior to the introduction of DNA is steady, no blockades are seen. (Right Inset) Typical current blockade with annotations. (b) Blockage ratio (B_r) vs. event dwell time (t_D) for n = 1178 events. Primarily a single blockade level with B_r = 0.17 is seen. (Inset) Corresponding event dwell time histogram with time constant t = 1.97 ± 0.2 ms. Broad dwell time distribution with large time constant suggests that events are indeed DNA translocations.[30]

Pore size was chosen to promote unfolded DNA entry into the pore and the absence of secondary populations at higher blockage ratios suggests that the folding of linear 5 kbp dsDNA fragments may not be significant in Al_2O_3 pores of diameter ≈ 5 nm. Wanunu et al. demonstrated the existence of only a single blockade level in Si_3N_4 pores of diameter 4 nm using 8 kbp dsDNA.[29] The inset of figure 19b is a dwell time histogram with t_P denoting the peak location (most probable translocation time), where t_P = 200 μs. A mono-exponential decay function with a time constant of t = 1.97 ± 0.2 ms is fitted to the dwell time distribution. As the vast majority of events are spread over the tail of the distribution, the mean dwell time (μ = 3.73 ms) is heavily weighted by the time-constant t rather than short events ($t_D < t_P$). The fitted time constant is in good agreement with time scales associated with DNA translocation in Si_3N_4 pores of similar size (~4 nm) using 6 kbp dsDNA fragments in 1 M KCl.[29] These slow time scales suggest that the majority of current blockades observed are indeed DNA translocation events involving significant interactions with the pore surface as opposed to DNA collisions (rapid interaction

without translocation) which typically have been shown to occur on much faster time scales of the order of $\tau \approx 100\ \mu s$.[29]

3.3 Chapter Summary

In summary, this chapter presented the development and characterization of highly sensitive, mechanically robust, Al_2O_3 nanopores for DNA detection. The process described achieves high yield, greatly reduces fabrication complexity and results in structurally robust, low noise platforms for single molecule analysis. Al_2O_3 nanopore sensors have all the advantages of existing SiO_2 and Si_3N_4 architectures (size control with sub-nm precision, chemical modification and attachment of organosilanes) but also exhibit superior noise performance over their solid-state counterparts. An order of magnitude reduction in high frequency noise (f >10 kHz) was observed relative to Si_3N_4 structures. Interestingly, a new phenomenon was witnessed during nanopore formation, i.e., the localized crystallization and facetted grain growth of hexagonal γ-Al_2O_3 nanocrystallites in the vicinity of the nanopore. The nucleation and growth of γ phase nanocrystallites was attributed to thermal annealing and electron beam assisted diffusion, thereby enhancing the local hardness of the nanopore. This phenomenon will be discussed in more detail in chapter 4. Finally, the detection of single molecules using this new architecture was demonstrated (5 kbp dsDNA) with signal-to-noise performance being on par with the state of the art in solid-state nanopore technology. Results suggest that nanopores in high *k*-dielectric materials such as Al_2O_3, with unique surface properties indeed function as highly sensitive biomolecule detection platforms, an alternative to well established SiO_2 and Si_3N_4 systems. This technology serves as a template to further explore the physics governing DNA transport. Such studies provide fundamental insight into the mechanisms driving biological processes including cell signaling and regulation using gated, selective ion channels, RNA translation using nuclear membrane pores, protein secretion across cellular membranes and viral infection by phages. This technology finds broad application in bio-nanotechnology.

Surface Enhanced Al_2O_3 Nanopore Sensors for DNA Analysis

4

In this chapter, we discuss the impact of material selection on the kinetics of DNA transport and present a qualitative model describing the nanopore formation process in Al_2O_3. Drastic changes in the material properties of the nanopore were observed during its nucleation and expansion, significantly impacting the sensitivity of these nano-scale single molecule sensors. Prolonged electron beam irradiation resulted in changes in the local stoichiometry and morphology of the pore from an amorphous, stoichiometric structure (O to Al ratio of 1.5 as expected in stoichiometric Al_2O_3) to a hetero-phase, crystalline, structure with a nonstoichiometric O to Al ratio of ~0.6. Preferential phase transformations from γ, α, κ and δ-Al_2O_3 nanocystallites to purely γ and α-phases were observed with increasing electron dose. Precise control over phase transformations in Al_2O_3 systems by varying electron dose provides a novel method to engineer surface charge at the nanopore/fluid interface. Direct metallization of the irradiated region was also observed with prolonged electron beam exposure, attributed to the preferential desorption of O and the aggregation of metallic Al clusters as confirmed through nanoarea electron diffraction (NED) and electron energy loss spectroscopy (EELS) in the TEM. This in-situ metallization process can possibly be used to fabricate a single nano-scale metallic contact directly in the nanopore. An applied potential to this contact would allow the direct manipulation of localized electric field gradients thereby affecting surface charge and pore conductivity, perhaps even enabling the electrostatic capture of charged biomolecules in the nanopore.

The translocation of dsDNA through these nanometer sized alumina pores revealed average translocation velocities that were an order of magnitude less than that observed in Si_3N_4 and SiO_2 systems under similar conditions, attributed to strong DNA-nanopore interactions. At present, high DNA translocation velocities (~30 bases/μs)[25] limit the utility of conventional SiO_2 and Si_3N_4 based nanopore technologies in high end DNA sensing and analysis applications including single nucleotide detection. In addition, the detection of these fast translocation events requires high bandwidth measurements which in turn reduces the signal-to-noise ratio in DNA detection

experiments. Thus, a nanopore architecture with an intrinsic ability to interact with DNA to reduce biomolecule transport velocities is highly desirable. Electron beam irradiated Al_2O_3 nanopore sensors provide such a capability. Two distinct polymer-pore interaction mechanisms influenced DNA translocation kinetics: electrostatic binding of anionic DNA to the positively charged nanopore surface enhanced by γ and α-Al_2O_3 nanocrystallite formation, and hydrophobic polymer-pore interactions promoted by the relatively high surface roughness of electron beam irradiated Al_2O_3. Our results confirm that nanopores formed in metal-oxide systems indeed provide a viable and highly functional alternative to conventional nanopore sensors, serving as effective tools for high-throughput single-molecule DNA analysis.

4.1 Device Characterization and Overview

The solid-state nanopore fabrication process used herein builds on prior work.[30] Low stress, mechanically stable, 45 ± 5 nm thick, amorphous Al_2O_3 membranes were formed using standard micro and nanofabrication processes as described in chapter 3. The inset of Figure 20a is a TEM cross section of a ~40 nm membrane after release (Region 3). Metal was sputtered on both sides of the membrane during TEM sample preparation as shown by regions 1, 2, 4, 5 for stability during cross sectioning. Energy dispersive x-ray spectroscopy (EDS) confirmed that the membrane contained only Al and O as shown in Figure 20a. Figure 20b is a TEM image of a 7 nm nanopore formed in this 45 ± 5 nm thick membrane using TEM decompositional sputtering process. The shot noise in the pore region confirmed that the electron beam has completely sputtered through the membrane. After fabrication, nanopore chips were O_2 plasma treated and immediately mounted between two compartments of a Delrin flow cell into which 1 M KCl with 10 mM Tris-HCl, pH 7.5 was introduced. Immediate wetting and ionic conduction through the pore was observed. In addition, linear current-voltage (IV) characteristics at different electrolyte concentrations (1 M, 100 mM and 10 mM) were observed for all pores measured. The linear IV characteristics of a 5 nm pore in 1 M, 100 mM and 10 mM KCl electrolyte are shown in Figure 20c. Figure 20d is a schematic representation of DNA translocation through a nanopore under an applied bias. DNA translocation studies involved the use of 5 kbp dsDNA (NoLimits™) from Fermantas Inc. with dsDNA being inserted into the chamber containing the anode (negative terminal) at a final concentration of 6 nM in 100 mM KCl, 10 mM Tris-HCl, pH 7.5 electrolyte.

Prior to the introduction of dsDNA, steady, blockade-free open pore currents were observed as shown in the inset of Figure 20e. After DNA insertion, characteristic current blockades/ translocation events were seen as shown in Figure 20e.

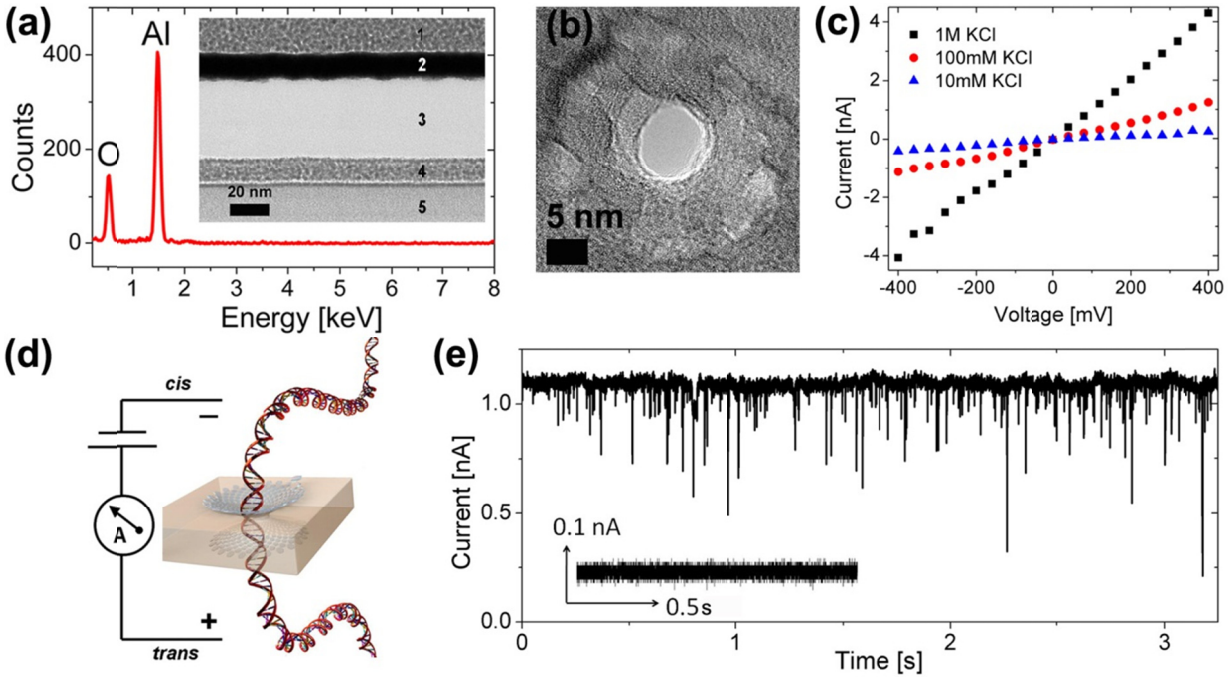

Figure 20 (a) EDS spectrum from an Al_2O_3 membrane confirming the presence of only Al and O. (Inset) TEM cross section of 40 nm thick Al_2O_3 membrane (Region 3) in which nanopores were formed. (b) TEM phase contrast image of a 7 nm pore formed using a focused convergent electron beam. (c) Linear IV characteristics from a 5 nm Al_2O_3 nanopore at KCl concentrations of 10 mM, 100 mM and 1 M. (d) Schematic of DNA transport through a nanopore under an applied bias. (e) Characteristic current blockades observed during DNA translocation of 5 kbp dsDNA through 7 nm pore at 500 mV. (Inset) Control prior to the insertion of dsDNA does not shows steady, blockade free current.[31]

4.2 Nanopore Nucleation

Focused electron probes in the TEM with diameters of 2.3 nm, 2.7 nm, 3.2 nm and 3.9 nm full width at half maximum (FWHM) corresponding to beam current densities of 2.6×10^6 A/m^2, 4.2×10^6 A/m^2, 6.1×10^6 A/m^2 and 1.2×10^7 A/m^2 respectively were used to sputter nanopores of

varying diameter. The sputtering process in Al_2O_3 is attributed to the Coulomb explosion displacement of atoms based on the Knotek-Feibelman electron-stimulated desorption mechanism.[133] The generation of positively charged oxygen ions results in a repulsive lattice potential forcing O^+ ions to either desorb from the surface (surface dissociated mechanisms) or to move to interstitial sites, thereby creating Frenkel pairs within the bulk of the material (volume dissociated mechanisms). This decompositional sputtering process was used to form nanopores ranging in diameter from 2 to 30 nm. The intensity profiles of the various electron probes used in these experiments are illustrated in figure 21a normalized with respect to the maximum peak intensity of the 3.9 nm probe. The inset of figure 21a is a TEM image of a 3.2 nm probe, light areas indicating regions of maximum electron intensity located at the center of the probe and darker areas indicating less intense regions located in the tail of the probe. Comparative probe analysis revealed that larger probe sizes exhibited higher peak intensities and a broader Gaussian-Lorentzian profile and were more suited for forming larger nanopores with diameters in the range of 10 – 30 nm. Such platforms are applicable for single molecule protein analysis and the detection of large analytes. In contrast, smaller probes (2.7 nm and 3.2 nm) exhibited lower peak intensity and a narrower profile, ideal for the high precision fabrication of 2 – 10 nm pores in Al_2O_3. These structures were well suited for ssDNA, dsDNA and RNA single molecule analysis.

Figure 21b is a plot of pore diameter versus electron beam exposure time for over 50 nanopores formed in 45 ± 5 nm thick Al_2O_3 membranes. Three stages were identified during nanopore formation: I, Pore Nucleation, II, Rapid Expansion and III, Controlled Growth. A critical beam current density in excess of 2.6×10^6 A/m^2 was required for nanopore nucleation in these membranes as shown in figure 21b. This is in good agreement with threshold current densities extracted by Salisbury et al. in experiments involving electron beam sputtered anodized alumina.[57] Below this threshold, topographical damage corresponding to the cleaving of Al-O bonds (bond dissociation energy of 513 kJ/mol)[31] was observed but electron momentum was insufficient to induce an embryonic nanopore structure. Pore contraction mechanisms were also seen to dominate at low beam current densities, possibly due to surface tension driven oxide reflow, generation/recombination of closely spaced Frenkel pairs[138] and mass transport of

mobile atoms into the nucleation site. This is consistent with the 'nanopore shrinking' phenomenon observed previously in SiO_2,[96, 129] and Al_2O_3 systems.[30]

Two distinct sputter rates were observed during pore formation (stages II and III of figure 21b) at current densities in excess of the threshold. The sputter rate transition observed cannot be attributed purely to the radial tapering in probe intensity seen in figure 21a. Intensity profiles of the probe reveal a differentiable Gaussian-Lorentzian function with no abrupt discontinuities, which in turn should translate to a gradual tapering in nanopore size with increasing electron beam exposure, unlike the sudden rate transition observed in these experiments. Thus, an additional mechanism is expected to contribute to the material removal process in Al_2O_3. We attribute this result to electron beam induced crystallization coupled with direct metallization of the nanopore region.

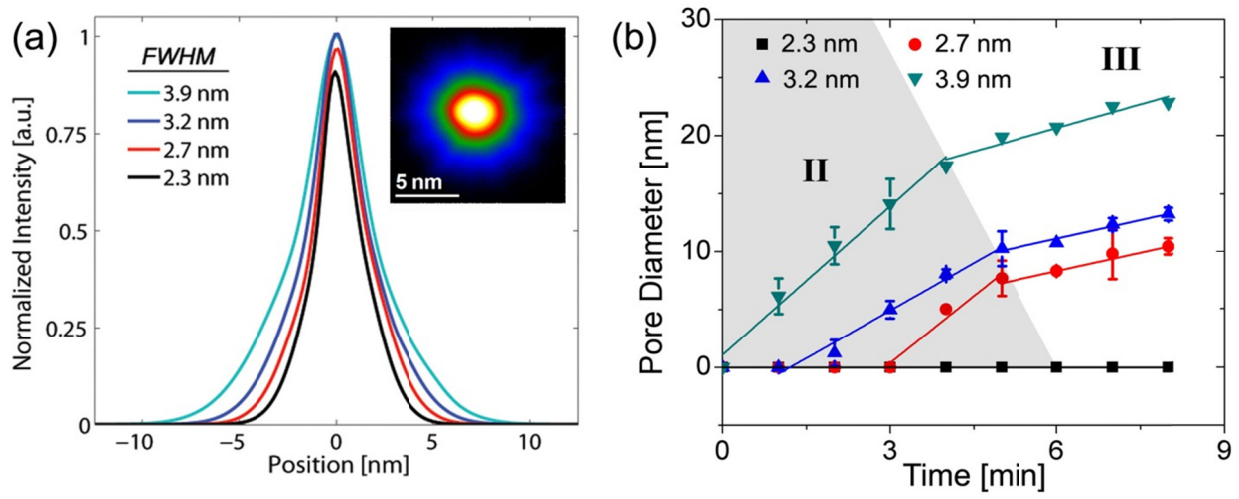

Figure 21 (a) Intensity profiles of the focused electron probes used during nanopore formation constructed from TEM images. Intensity is normalized with respect to peak intensity of the 3.9 nm *FWHM* probe. (Inset) TEM image of a 3.2 nm probe showing spatial intensity distribution. (b) Nanopore sputtering kinetics illustrating pore diameter .vs. time for the various probes examined. Distinct expansion rates were observed delineating the three stages of pore formation: I Pore Nucleation (not shown), II Rapid Expansion and III Controlled Growth.[31]

4.3 Electron Beam Induced Crystallization

4.3.1 Electron Diffraction

NED was used to understand the structural phase transformation of the membrane material around the pore. Figure 22 shows the evolution of the structure of the amorphous membrane during the three stages of pore formation. Figure 22a shows a NED pattern from the amorphous membrane prior to exposure to the intense convergent electron beam. The inset shows the 50 nm coherent parallel electron probe with probe intensity set sufficiently low as to not alter the morphology of the nanopore. Beam current density in NED mode was ~5.4×10^3 A/m^2, more than three orders of magnitude less than in convergent beam mode. The presence of diffuse rings and the absence of distinct rings or discrete spot reflections in figure 22a confirms the lack of crystalline phase in the amorphous alumina membrane.

Figure 22b shows an indexed NED pattern from a ~14 nm pore formed after 3 minutes of sputtering with a 3.9 nm convergent electron probe. The NED pattern is typical of pore formation in stage II of figure 22b. Discrete spot reflections of α and/or γ phase Al_2O_3 are visible, confirming the formation of nanocrystalline clusters of preferred phases. Reflection 1 (marked by green circle) exhibits six-fold symmetry and a d-spacing of 1.16 Å, which is indicative of either α or γ-Al_2O_3. Reflections 2 (marked by blue circle) and 3 (marked by red circle) have d-spacings of 0.67 Å and 0.58 Å respectively which again matches both α and γ-phase Al_2O_3. In α-Al_2O_3, Al^{3+} cations are octahedrally coordinated with average Al-O bond lengths of 1.92 Å.[139] γ-Al_2O_3 typically exhibits a cubic defect-spinel type structure with average Al-O bond lengths of 1.89 Å.[140] Reflections 4 and 5 (marked with squares) were significantly weaker and correspond to the nucleation of δ and/or κ phase nanocrystallites. The presence of multiple heterogeneous phases with varying bond lengths and co-ordinations indicates that an irregular density of exposed Al-O groups exist at the pore surface which in turn corresponds to an irregular surface charge distribution in a hydrated nanopore. This irregular charge distribution is expected to strongly impact DNA translocation kinetics. The diffraction pattern of figure 19b confirms that initial electron beam exposure to the amorphous material nucleates several crystal phases.

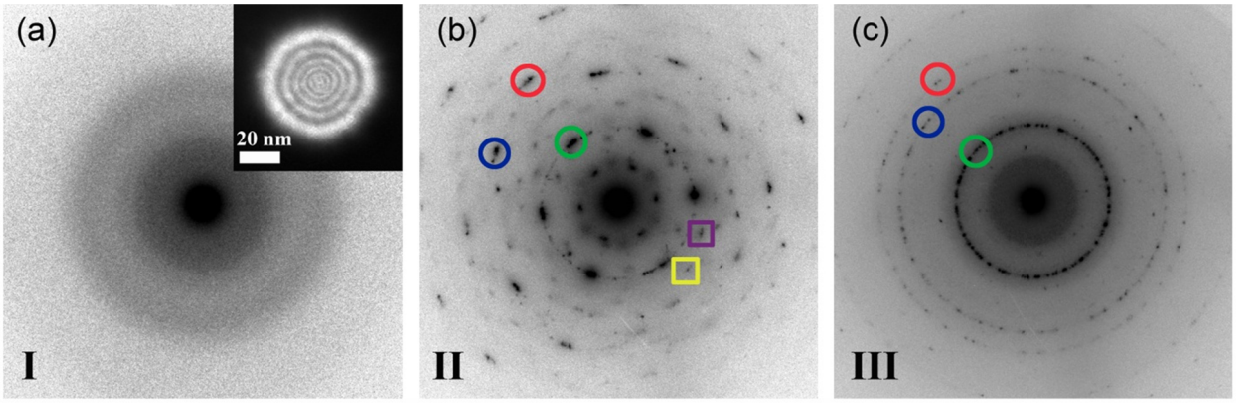

Figure 22 Nano-area diffraction images taken using a ~50 nm parallel electron probe as shown in the inset. (a) NED image of the Al_2O_3 support prior to pore formation shows that the membrane is amorphous. (b) NED pattern obtained by placing parallel electron probe over pore located in stage II of Figure 18b. Distinct spot reflections marked with circles are observed corresponding to formation of γ and α-Al_2O_3 nanocrystallites. Additional reflections marked by squares are from δ and κ phases. (c) NED pattern obtained by placing parallel electron probe over pore located in stage III of Figure 18b. Continuous rings are observed confirming that a polycrystalline material with preferred phases (γ and α) is formed by prolonged exposure to the convergent beam.[31]

Figure 22c is a NED pattern from a ~22 nm pore formed after 8 minutes of sputtering using a 3.9 nm probe (stage III in figure 21b). The NED pattern shows that prolonged exposure to the convergent beam results in a polycrystalline structure with preferred α and/or γ phases. A comparison to figure 19b shows that initial electron beam irradiation nucleates large, multi-phase crystals indicated by the many discrete reflections of different d-spacings in figure 22b. Prolonged exposure, however, generates many smaller crystals of preferred phase, indicated by polycrystalline rings with distinct yet fewer d-spacings (figure 22c). These results provide evidence that the surface charge at the pore can be engineered based on critical electron doses. It is important to note that surface charge density in this case is dependent on both the coordination of the phases and the pore size which are not independent of each other. Therefore, only certain surface charge densities are likely possible. Surprisingly, there are no strong reflections

corresponding to elemental Al in the NED patterns of stage II or III. Metallic Al would be expected as O is preferentially sputtered during prolonged electron beam irradiation.

4.3.2 Electron Energy Loss Spectroscopy

EELS analysis provided further insight into the mechanisms driving pore formation and nanocrystallite nucleation. Figure 23 shows low loss (plasmon) and core loss EELS spectra taken before pore formation and after stage III of pore formation. Figure 23a shows the evolution of the low loss region of the spectrum with prolonged electron beam irradiation. Before exposure to the CBED beam, there is a broad, nearly symmetric plasmon peak located at ~24 eV that corresponds to the bulk Al_2O_3 plasmon excitation. The plasmon peak measures longitudinal wave-like scattering of incident beam electrons by delocalized valence electrons in the specimen and is sensitive to specimen bonding and thickness. Thicker specimens exhibit a taller plasmon peak due to a higher scattering probability.

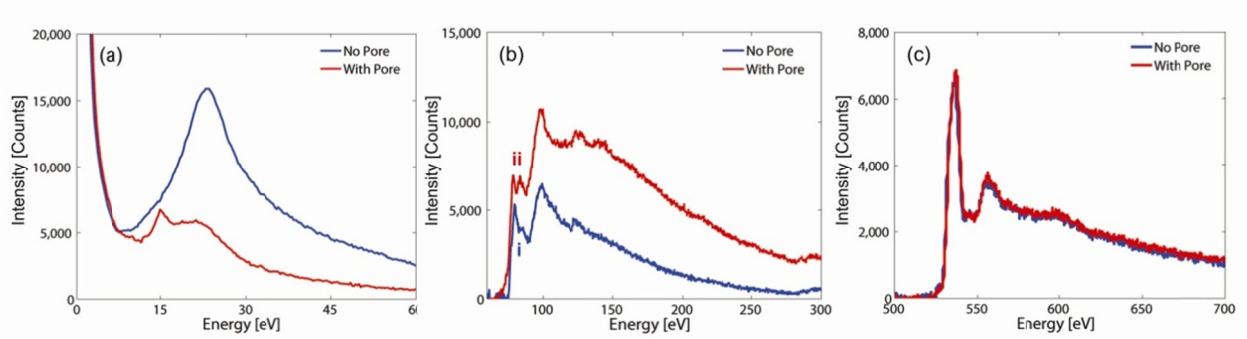

Figure 23 EELS spectra before (blue) and after (red) pore formation. (a) Low-loss region shows attenuation of alumina plasmon peak located at ~24 eV and the formation of a sharp peak at ~15 eV corresponding to the bulk Al Plasmon. (b) Background subtracted Al L-edge. Prior to pore formation, the Al L-edge resembles that of Al in Al_2O_3 form. (i) Al $L_{2,3}$ edge. After sputtering the Al L-edge consists of the superposition of L edges from metallic Al and Al in Al_2O_3 form. (ii) Splitting of the Al $L_{2,3}$ edge. Results confirm the formation of metallic Al in the pore region. (c) Background subtracted O K-edge. O to Al ratio in the pore region is reduced from 1.5 to ~0.6 due to preferential sputtering of oxygen.[31]

After pore formation via electron beam-induced sputtering, the plasmon peak at ~24 eV decays significantly and a secondary peak at ~15 eV is formed. The total area under the low loss

spectrum decreases due to material removal at the pore nucleation site resulting in fewer scattering events. The formation of this plasmon peak at ~15 eV corresponds to plasmon excitations in metallic Al. Comparison to references shows no Al oxides have plasmon peaks at 15 eV.[141] This result confirms that Al-rich regions are formed at and near the pore edge due to the preferential desorption of O.

To confirm the presence of Al rich nanocrystals, core loss edge EELS was acquired before and after pore formation as shown in figure 20b. Prior to pore formation, the Al $L_{2,3}$ edge exhibits a sharp L_3 peak at 75 eV while the L_2 peak appears as a small shoulder (shown by i). Following the edge, there is a broad peak located at 99 eV. This is consistent with Al L-edges acquired from amorphous Al_2O_3.[140] After pore formation, the $L_{2,3}$ edge appears more intense indicating that there are more unoccupied states in the Al 3d band. In addition, the Al $L_{2,3}$ edge is chemically shifted to 72 eV and the L_3 / L_2 splitting is more distinct with both edges displaying similar intensity (shown by ii). The post-edge is rounder and the magnitude of the slope is greater. A comparison of the post-edge to references shows that the EELS spectrum after pore formation is a linear combination of spectra acquired from metallic Al and γ-Al_2O_3.[133, 140] Berger et al. obtained similar EELS spectra during the formation of trenches and slots in amorphous Al_2O_3 and Na-β Al_2O_3 systems.[133] The O K edge located at 537 eV did not change significantly after sputtering the pore as seen in figure 23c. Compositional variations were calculated by the *k-factor*[142] method and revealed that the O to Al ratio in the local nanopore region decreased from 1.5 before pore formation to ~0.6 after pore formation. This result confirms that the sputtering process preferentially desorbs oxygen, leaving behind Al-rich nanocrystals resulting in a partially metalized nanopore. Similar phenomena were observed in electron-beam hole drilling experiments conducted in Na-β Al_2O_3.[142] Coupled with studies by Berger et al. demonstrating the formation of continuous Al regions and "plugs" in electron-beam irradiated metal β-aluminas,[133] in theory it should be possible to form a single nano-scale metallic contact within the nanopore using the method outlined in this work. Interfacing with electrodes patterned using electron beam lithography techniques is also possible by rastering the focused electron probe over regions adjacent to and overlapping the metal contacts and the pore. A nanopore with an embedded electrode could be used to manipulate electric field gradients in the pore and actively modulate surface charge and pore conductivity. Simulation work by Lagerqvist et al.

demonstrated the ability to achieve single nucleotide resolution by employing a nanopore sensor with embedded transverse sensing electrodes, with potential application to nanopore-based DNA sequencing.[14] With further characterization, the nano-scale metallization process reported here could help enable the possible realization of such a structure.

4.4 Nanopore Expansion Kinetics

The morphological transition of the pore from amorphous Al_2O_3 to a hetero-phase, Al rich structure as confirmed through NED and EELS in turn affects subsequent pore expansion kinetics. Amorphous Al_2O_3 is sputtered primarily via volume dissociated mechanisms exhibiting rapid and abrupt mass-loss, attributed to the displacement of metallic Al and the formation of oxygen gas bubbles due to anion aggregation.[143], [144] This mechanism explains the rapid pore expansion initially observed (stage II of figure 21b). With continued electron beam irradiation, the amorphous Al_2O_3 support transitions into a hybrid polycrystalline-metallic structure (O to Al ratio of ~0.6). Mass loss in this Al-rich, polycrystalline system (stage III of figure 21b) is consistent with the Coulomb explosion displacement of atoms in Na-β Al_2O_3 systems. These hybrid systems are typically sputtered through surface dissociated sputter mechanisms characterized by steady and continuous loss of material from the surface, resulting in lower sputter rates, Al aggregation and the absence of O_2 bubble formation.[133, 143] The decreased yet constant expansion rate observed in stage III of figure 21b is consistent with this result. Mochel et al. also reported steady, constant growth rates during the formation of nanometer sized holes in metal β-aluminas.[145] The absence of a sharp pre-peak at ~532 eV in the O K edge spectrum of figure 23c furthermore confirms that O_2 bubble formation and volume dissociated mechanisms are less dominant in stage III. These results provide further insight into the lithographic properties of self-developing materials such as metal halides and metal oxides and are applicable to the rapid development of high precision nanopore arrays in these material systems for the detection of ssDNA, dsDNA, RNA and small proteins.

4.5 Surface Enhanced DNA Detection

Surface enhanced DNA detection was characterized through electronic measurements. DNA translocation experiments involved the electrophoretic transport of 5 kbp dsDNA through ~7 nm diameter nanocrystalline Al_2O_3 nanopores at voltages of 100 mV, 300 mV and 500 mV, as shown in figures 24 a, b and c respectively. Figure 24 illustrates characteristic current blockades observed at each voltage during DNA translocation. The insets of figure 24 illustrate the blockade free open pore current at each voltage prior to the introduction of dsDNA.

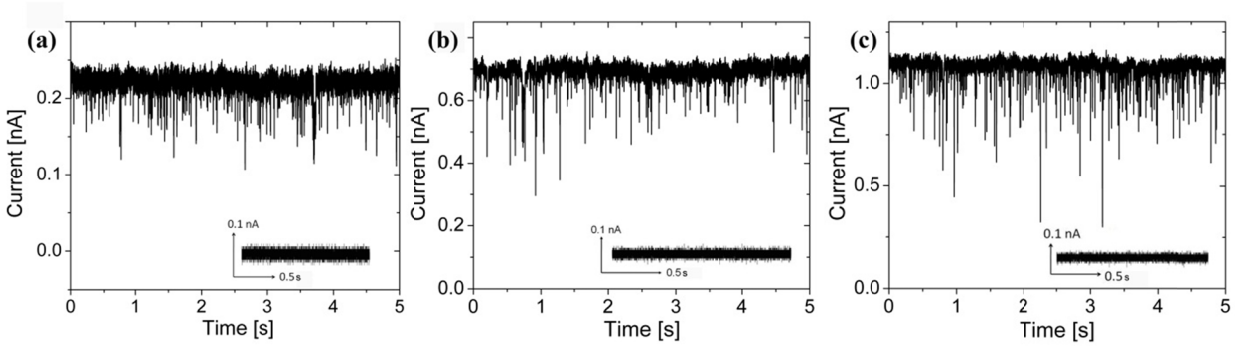

Figure 24 Typical current traces from a ~7 nm nanocrystalline Al_2O_3 pore after the addition of 5 kbp dsDNA at a concentration of 6 nM to the *cis* side (anode) of the setup at applied voltages of (a) 100 mV, (b) 300 mV, (c) 500 mV. Distinct downward current blockades were observed. (Insets) Negative controls at each voltage: Pore current is steady prior to the introduction of dsDNA, no blockades were seen.[31]

Table 2 summarizes experimental results including open pore current, *I*, average dwell times, $\mu(t_D)$, t_1 and t_2 timescales associated with translocation, average blockage ratios, $\mu(B_r)$, total number of events, *n*, and capture rates, *R,* at these respective voltages (see Table 1 for definitions of these terms).

Table 2 Summary of results involving electrical sensing of 5 kbp dsDNA through a ~7 nm nanopore at voltages of 100 mV, 300 mV and 500 mV. t_D: Dwell time (time biomolecule resides in the pore), B_r: Blockage ratio (percentage of open pore current that blocked during DNA translocation), n: Biomolecule flux (total number of events during 5 minutes of recording), R: Capture rate (average number of translocation events per second) .

V [mV]	**100**	**300**	**500**
I (open pore) [nA]	0.23	0.7	1.2
$\mu(t_D)$ [ms]	3.5 ± 10.8	1.3 ± 4.3	0.8 ± 1.9
t_1 [ms]	0.48 ± 0.05	0.35 ± 0.01	0.28 ± 0.02
t_2 [ms]	2.0 ± 0.7	2.9 ± 1.3	2.6 ± 2.2
$\mu(B_r)$ [%]	0.42	0.32	0.28
n [events]	1421	1954	5351
R [Hz]	4.7	6.5	17.9

The results clearly indicate that average dwell times decrease with increasing voltage. As expected, an increase in the applied voltage results in an increase in the electrophoretic driving force experienced by the DNA molecule during transit, resulting in higher translocation velocities and shorter dwell times. This voltage dependent behavior has been independently observed in biological α-hemolysin nanopores[45] and Si_3N_4[25] systems and serves as a complementary method to gel-electrophoresis to verify DNA transport through nanometer sized pores. A threshold voltage of 70 mV was observed in translocation experiments below which current blockades were not observed, suggesting the presence of a significant activation/entropic barrier associated with dsDNA transport through nanopores formed in Al_2O_3 membranes. In addition, biomolecule flux, *n*, and capture rate, *R*, increased exponentially with increasing voltage. Brun et al. also observed exponential increases in capture rate with increasing voltage during the transport of small polyelectrolytes through proteinaceous pores with capture rates following a simple Van't Hoff-Arrhenius relationship.[49] Similar trends were observed in experiments involving ssDNA passage through α-hemolysin.[47, 48]

Interestingly, mean dwell-times at an applied bias of 100 mV yielded a translocation velocity of ~1.4 nucleotides/μs, more than an order of magnitude slower than dsDNA translocation through Si_3N_4 nanopores (~30 nucleotides/μs) at similar biases,[28] but an order of magnitude faster than single stranded DNA translocation through α-hemolysin.[25] Lubensky and Nelson accredited the

slow translocation rates in α-hemolysin to strong polymer interactions with the pore walls.[146] We theorize that DNA-pore interactions also play an important role in slowing the rate of DNA transport through nanocrystalline Al_2O_3 nanopores. To verify this, a more in-depth examination of the translocation kinetics through these solid-state nanopores is needed. Figures 25 a, b, c are dwell-time histograms at applied voltages of 100 mV, 300 mV and 500 mV. The insets of figures 25 a, b, c are event density plots of blockage ratio (B_r) versus dwell time (t_D) at these applied voltages. The red regions represent high event densities corresponding to the most probable event characteristics in terms of blockage ratios and translocation times. The most probable translocation characteristics are bounded by the arrows in the insets.

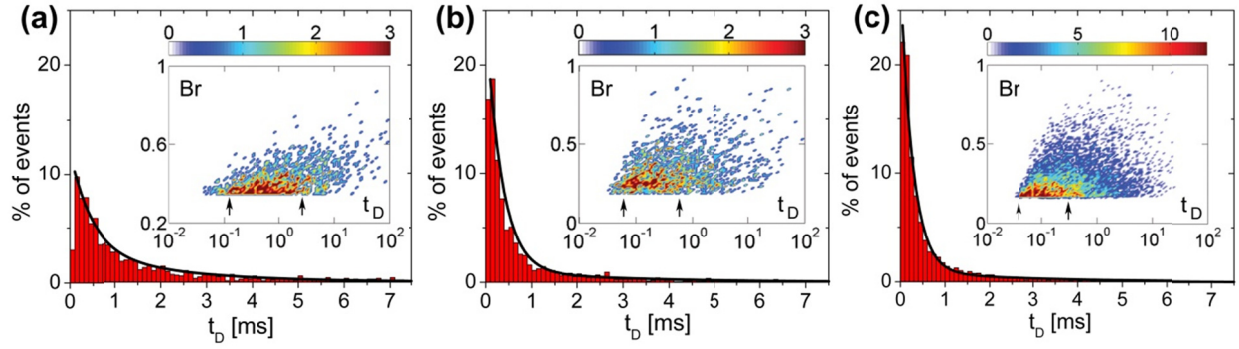

Figure 25 Dwell time histograms at applied voltages of (a) 100 mV, (b) 300 mV, (c) 500 mV. Each distribution is fitted with a bi-exponential function (black line) with two time constants, t_1 and t_2, indicating the two types of polymer transport, fast translocation governed by polymer hydrodynamics and slow translocation regulated by polymer-pore interactions. (Insets) Blockage ratio (B_r) vs. Dwell time (t_D) [ms] at these respective voltages. Color bar represents number of events. At higher voltages, a greater percentage of events exhibit fast translocation dynamics bounded by the arrows in the insets. Translocation events exhibit clear voltage dependence.[31]

The dwell-time histograms of figure 25 exhibit broad biexponential tails fitted using two time constants, t_1 and t_2, as summarized in table 1. The results suggest that there are two distinct timescales associated with DNA transport through ~7 nm Al_2O_3 nanopores. The shorter timescale, t_1, is associated with fast polymer transport through the pore with minimal DNA-pore interactions. t_1 timescales exhibit strong voltage dependence suggesting that these events are indeed due to polymer transport through the pore as opposed to rapid, diffusion driven collisions

without translocation.[147] Such fast translocations are probable in larger ~7 nm pores via translocation through the central pore region where the effects of surface binding sites and surface charge are significantly screened. Fast translocation events were not observed in smaller ~5 nm Al_2O_3 nanopores suggesting that pore size and Debye layer thickness indeed play an important role in regulating the velocity of DNA transport.[30] t_1 timescales are also significantly faster than the characteristic relaxation time or Zimm time of 5 kbp dsDNA in 100 mM salt. The Zimm time, t_Z, is an upper bound on the time taken by a polymer to reach an entropically and sterically favored state and is given by $t_z \approx 0.4\eta R_g^{\,3} / k_B T$. [27] Given solvent viscosity $\eta = 1$ mPas and polymer radius of gyration $R_g = \sqrt{2 l_p L} \approx 0.4$ μm at a persistence length of $l_p = 50$ nm for dsDNA in 100 mM KCl buffer, we calculate $t_z \approx 7$ ms. As $t_1 << t_Z$, polymers exhibit a rigid or "frozen" polymer configuration in the pore during t_1 translocation events and thus interact minimally with the pore walls. This rigid rod-like behavior is consistent with modeling results by Berezhkovskii et al. that predict decreasing dwell-times and narrower event distributions with increasing applied force for the transport of rod-like macromolecules through nanochannels.[148] To reach a configuration that permits such fast translocations, polymers likely undergo coil-stretch transitions prior to entering the pore. In a positively charged nanopore as is the case here at pH 7.5 (isoelectric point of Al_2O_3 ~ 9)[93], the electro-osmotic flow (EOF) is oriented in the same direction as polymer translocation resulting in an absorbing region around the nanopore comparable in size to R_g of the polymer. Within this absorbing region, the velocity gradient of the fluid is larger than the critical velocity gradient necessary for coil-stretching.[149] Molecules entering this region undergo coil-stretch transitions that help to elongate the molecule and reduce the entropic barrier associated with translocation, thereby allowing for fast translocations. The fast translocation events observed in these experiments are consistent with timescales ($\mu(t_D) \approx 162$ μs) associated with the transport of 6557 bp dsDNA through much larger ~10 nm SiO_2 nanopores.[27]

The longer time scale, t_2, is associated with DNA translocations involving significant interactions with the nanopore. We observed similar phenomena in small ~5 nm Al_2O_3 nanopores, characterized by a monoexponential decay in dwell time histograms with time constants consistent with t_2 timescales (1.97 ± 0.2 ms).[30] Polymer-pore interactions were also reported in

small 2.7 – 5 nm Si_3N_4 nanopores.[147] The origins of these interactions are hydrophobic and/or electrostatic in nature and are dependent partially on the material properties of the pore (stoichiometry, morphology and surface roughness). NED and EELS confirmed the formation of hetero-phase crystalline domains (in particular γ and α-phases) of varying bond lengths and co-ordinations in the nanopore region, resulting in non-uniform distributions of exposed Al-O groups at the pore surface. In a hydrated nanopore, these surface sites react with adsorbed water to form protonated hydroxyl groups at pH 7.5, resulting in a net positive, non-homogeneous surface charge density across the pore. The existence of crystalline domains of varying charge density is likely as α-Al_2O_3 and γ-Al_2O_3 both exhibit different points-of-zero-charge (pzc's), estimated at pH 9.1 and pH 8.5 in monovalent salt solution.[150, 151] In addition, the Zeta potentials of these materials measured in pH 7.5 electrolyte are ~50 mV and ~25 mV respectively,[152, 153] and thus these charged domains are expected to interact differently with anionic DNA. Alterations to pore stoichiometry due to the preferential desorption of O and the aggregation of Al is also expected to result in a distribution of equilibrium constants (pK's) for the protonizable chemical sites across the pore. The resulting electrostatic interactions/binding between the non-homogeneous, net positively charged nanopore surface and anionic DNA is one factor contributing to the slow translocation velocities observed in these experiments. Modeling results by Kejian et al. confirmed that polymer translocation velocities in a solid-state nanopore are heavily dependent on zeta potential and surface charge.[154] Furthermore, studies by Kim et al. on nanopores derivatized with aminopropyltriethoxysilane relied on electrostatic binding events between the positively charged aminated surface and the negatively charged DNA backbone to slow down DNA transport through the pore.[119]

The strong electrostatic binding observed in our experiments was not reported in SiO_2 and Si_3N_4, likely as these systems exhibit a net negatively charged surface at pH 7.5 resulting from the deprotonation of surface silanol groups.[87] Furthermore, a comparison of the surface charge density of Si_3N_4 and γ-Al_2O_3 surfaces at pH 7.5 (in monovalent salt solution at concentration $1x10^{-4}$ M) revealed a charge density that is approximately six times higher in γ-Al_2O_3 (50 mC/m^2) than in Si_3N_4 (8 mC/m^2) systems.[73, 150] Thus, polymer-pore interactions involving electrostatic binding events are expected to be more prominent in Al_2O_3 nanopores. Hydrophobic interactions between DNA bases and the pore surface may also be prevalent in Al_2O_3 nanopore systems.

Simulation work by Aksimentiev et al. reported on such a phenomena in Si_3N_4, resulting in biomolecule adhesion and even partial unzipping of dsDNA during transport leading to increased dwell times in the pore.[155] Such interactions may be enhanced in Al_2O_3 systems as the material undergoes significant surface roughening during e-beam irradiation as seen through irregular faceting and thickness variations across the pore region, thereby increasing the surface area available for hydrophobic polymer-pore interactions. Electron beam induced surface roughening during hole formation is particularly prominent in α-Al_2O_3 systems.[134] Given the hydrophobic/electrostatic interaction mechanisms described here and the comparability of t_Z and t_2 timescales, it is expected that t_2 translocation events likely involve surface dependent polymer-pore interactions, resulting in polymer relaxation and conformational change during translocation. Such polymer translocation events may be modeled as a series of thermally activated barrier hops over small energy barriers of varying height as opposed to single barrier crossing events.[147] Our results clearly suggest that Al_2O_3 nanopore sensors serve as highly functional platforms for single molecule DNA analysis with the capability to regulate the rate of DNA transport through complex surface interactions.

4.6 Al_2O_3 Nanopore Functionalization

An exciting prospect emerging from this work is the potential modification of nanocrystalline Al_2O_3 nanopores with various surface chemistries to further enhance the sensitivity and chemical specificity of these nano-scale sensors. Liquid-phase silane based chemistries are well characterized on Al_2O_3 surfaces, forming high density, mechanically stable, self-assembled monolayers (SAMs) and are commonly used to chemically modify anodic aluminum oxide (AAO) nanoporous arrays.[156-158] This functionalization strategy is also applicable to the chemical modification of individual nanocrystalline Al_2O_3 nanopore sensors. Preliminary studies on silanized ALD Al_2O_3 surfaces confirm the formation of stable SAMs, verified through x-ray photoelectron spectroscopy, contact angle and fluorescence measurements as shown in Figure 26.

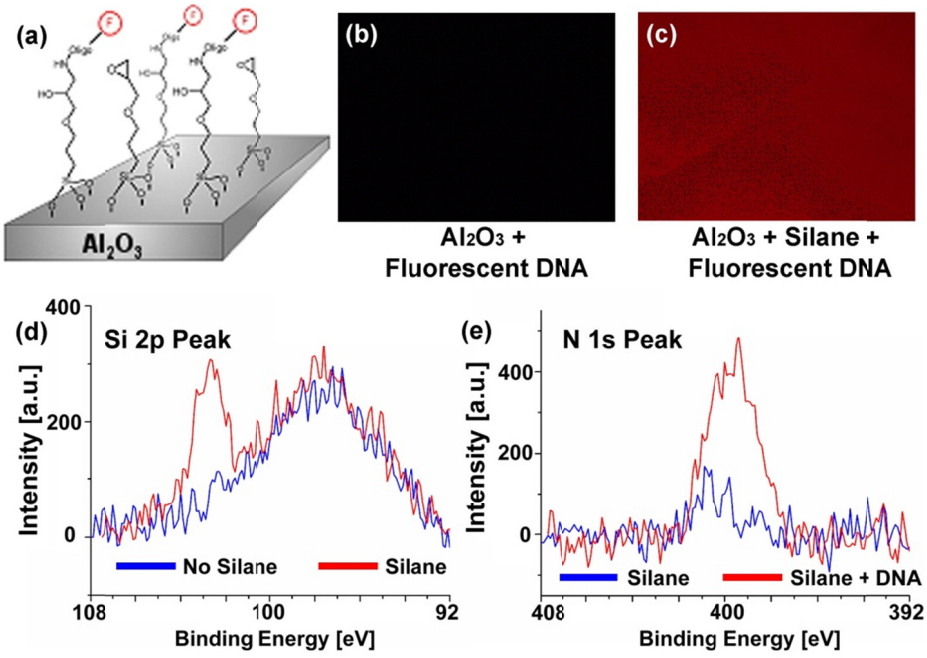

Figure 26 (a) Schematic of Al_2O_3 silane functionalization followed by the attachment of a fluorescent DNA probe. (b) Fluorescent DNA probe attachment without silane showing that non-specific binding is minimal. (c) DNA probe attachment with intermediate silane layer confirmed through fluorescence. (d) High resolution XPS confirms SAM formation on Al_2O_3 through increase in Si 2p peak intensity. (e) High resolution XPS confirms binding of DNA probe to silane layer through increase in N 1s peak intensity.

Note that care should be taken to fully oxidize the partially metalized nanopore surface after electron beam sputtering using an O_2 plasma, prior to any piranha treatment (3:1 H_2SO_4:H_2O_2) or surface functionalization procedures. Target-specific molecular recognition in these functionalized nanopore systems is achieved through the subsequent attachment of specific recognition sequences or tethered receptors to the silanized nanopore surface. This procedure has been successfully demonstrated in functionalized AAO nanoporous arrays, one specific example being the electrical detection of DNA hybridization reactions using AAO templates containing immobilized ssDNA probes. Using cyclic voltammetry methods, the authors were able to detect impedance shifts upon probe hybridization with complementary target ssDNA present in the solution phase.[159] Functionalized AAO nanoporous templates have also been successfully applied in DNA separation, sorting and sequence recognition applications.[160] These 'bulk' ensemble average methods, however, lack the single molecule sensitivity that is inherent to individual solid-state nanopores. Therefore, by combining the molecular specificity reported in

functionalized AAO template studies with the single molecule detection capabilities of single nanocrystalline Al_2O_3 nanopore sensors, a new family of highly sensitive, chemically selective nanopore sensors can be developed and tailored for specific bio-sensing applications. In drug screening and medicine, such technologies would provide a means to study the label-free, real-time kinetic analysis of biomolecular interactions at the single molecule level including protein-protein, protein-DNA and receptor-ligand interactions.

4.7 Chapter Summary

In summary, this chapter presented the development of nanocrystalline surface enhanced Al_2O_3 nanopore sensors for high throughput DNA analysis. Nanopore formation through electron beam based decompositional sputtering of amorphous Al_2O_3 transformed the local nanostructure and morphology of the pore from an amorphous, stoichiometric structure (O to Al ratio of 1.5) to a hetero-phase crystalline structure with O to Al ratio of ~0.6. Preferential phase transformations from γ, α, κ and δ-Al_2O_3 to purely γ and α-phases were observed with increasing electron dose. Dose-dependent control over phase transformations at the nanopore/fluid interface is highly desirable as it provides a novel method to engineer surface charge in the nanopore. The evolving nanostructure of the pore also affected nanopore expansion kinetics; rapid, abrupt mass loss observed in the amorphous state and steady material removal in the polycrystalline/metallic state, attributed to transitions from volume to surface dissociated sputtering mechanisms. In addition, sputtering induced the direct metallization of the pore region as confirmed through EELS and NED. This in-situ metallization process provides a potential means to create nano-scale metallic contacts in the pore region for manipulating surface charge and pore conductivity.

DNA transport studies revealed an order of magnitude reduction in translocation velocities (~1.4 nucleotides/μs) in comparison to Si_3N_4 and SiO_2 architectures, attributed to strong electrostatic binding events between anionic DNA and the positively charged nanopore surface. These complex surface interactions are enhanced in Al_2O_3 due to high surface charge density, the nucleation of α, γ-Al_2O_3 nanocrystallites and high surface roughness. The enhanced sensitivity and favorable surface characteristics of Al_2O_3 nanopore sensors suggest that this metal-oxide

platform may indeed prove to be a viable and functional alternative to conventional Si_3N_4 and SiO_2 based nanopore systems, ideal for the detection and analysis of ssDNA, dsDNA, RNA secondary structures and small proteins.

Lipid Bilayer Coated Al_2O_3 Nanopore Sensors 5

Solid-state nanopore sensors are highly versatile platforms for the rapid, label-free electrical detection and analysis of single molecules, applicable to next generation DNA sequencing. The versatility of this technology allows for both large scale device integration and interfacing with biological systems. In this chapter we report on the development of a hybrid biological solid-state nanopore platform that incorporates a highly mobile lipid bilayer on a single solid-state Al_2O_3 nanopore sensor, for the potential reconstitution of ion channels and biological nanopores. Such a system seeks to combine the superior electrical, thermal, and mechanical stability of Al_2O_3 solid-state nanopores with the chemical specificity of biological nanopores. Bilayers on Al_2O_3 exhibit higher diffusivity than those formed on TiO_2 and SiO_2 substrates, attributed to the presence of a thick hydration layer on Al_2O_3, a key requirement to preserving the biological functionality of reconstituted membrane proteins. Molecular dynamics simulations demonstrate that the electrostatic repulsion between the dipole of the DOPC headgroup and the positively charged Al_2O_3 surface may be responsible for the enhanced thickness of this hydration layer. Lipid bilayer coated Al_2O_3 nanopore sensors exhibit excellent electrical properties and enhanced mechanical stability (GΩ seals for over 50 hours), making this technology ideal for use in ion channel electrophysiology, the screening of ion channel active drugs and future integration with biological nanopores such as α-hemolysin and MspA for rapid single molecule DNA sequencing. This technology can find broad application in bio-nanotechnology.

5.1 Introduction to Lipid Bilayers

Biological membranes form the physical barrier between the interior of cells and their extracellular environments and play an important role in cellular structure and function. These membranes consist of a variety of integral and peripheral membrane proteins (receptors, transporters, ion channels, pumps, lipid metabolic enzymes, nuclear porins) and carbohydrates embedded in a fluid lipid bilayer matrix, the interactions of these membrane proteins with their environment facilitating vital cellular processes such as membrane trafficking and intracellular signaling. The ability of membrane proteins to regulate cellular activity also makes them an ideal

target for drug development, with cell membrane receptors, largely G protein-coupled receptors and enzymes, constituting over 70% of all current drug targets.[161] The functional role of membrane proteins is typically investigated using supported phospholipid bilayers (SPBs), an in-vitro analog to the biological cell membrane. SPBs are continuous lipid membranes formed on hydrophilic substrates containing a 10-20 Å trapped interfacial water layer, essential to preserving the long range fluidity and functionality of the bilayer.[162, 163] SPBs have been used to study cell-cell interactions, cell growth and adhesion, and multivalent receptor-ligand binding [8][8], for controlled drug release; as well as they also find application in electro-optical biosensors, drug discovery and biocatalysis.[164] In addition, these model biomimetic systems are mechanically more robust than freestanding black lipid membranes (BLMs) and can be integrated with surface-specific analytical techniques such as atomic force microscopy (AFM) and nuclear magnetic resonance (NMR).

The two most common techniques to form SPBs on hydrophilic substrates are the Langmuir-Blodgett transfer technique,[165] and the vesicle adsorption and rupture method.[166, 167] The latter is more versatile, allows for the incorporation of membrane proteins during vesicle preparation and has been traditionally used to form SPBs on quartz, glass, mica and metal oxides such as TiO_2 and $SrTiO_2$. The vesicle rupture process is highly dependent on surface electrostatics[168] and van der Waals forces.[169] High adhesion energies result in vesicle rupture, bilayer stiction and a loss of lateral fluidity, as seen with bilayers formed on chromium and indium tin oxide substrates,[170] making these SPBs incompatible with membrane protein integration. In contrast, low surface adhesion energy on substrates such as Al_2O_3 prevents vesicle rupture from occurring resulting in intact, stable, supported vesicle layers (SVLs).[171, 172] A variety of strategies have been used to increase surface adhesion energy to induce bilayer formation on Al_2O_3 including surface functionalization,[173] preparation of charged lipid compositions,[174] and the addition of fusigenic agents such as polyethylene glycol.[175] These strategies, however, require additional processing steps, chemically modify the surface characteristics of Al_2O_3 and potentially mask the desired optical and electrical properties of the substrate.

Here, we report the formation of highly fluid, defect-free lipid bilayers on unmodified Al_2O_3 surfaces through vesicle fusion and apply this technique to form high impedance, fluid lipid

bilayers on single Al_2O_3 nanopore sensors. Suspending fluid lipid bilayers on Al_2O_3 solid-state sensors opens up new possibilities, allowing for the reconstitution of single ion channels, the sensitive screening of ion channel active drugs, and the insertion of chemically selective biological nanopore channels such as α-hemolysin and MspA for DNA sequencing. Proteinaceous mutant α-hemolysin and MspA nanopores are currently capable of discriminating individual nucleotides, making way for a single molecule sequencing approach.[8, 11] The use of these biological nanopores as commercial diagnostic sensors, however, is limited by the lack of mechanical stability of the lipid membranes into which they are inserted. Biointerfacing highly sensitive, mechanically stable Al_2O_3 nanopores with fluid lipid bilayers for protein channel insertion provides a robust solution, an important first step in the development of hybrid biological solid-state nanopores, applicable to medical diagnostics, drug screening and DNA sequencing.

We demonstrate first the formation of fluid lipid bilayers on planar atomic layer deposited (ALD) Al_2O_3 surfaces, a material system previously deemed incompatible with bilayer formation. Vesicle rupture on Al_2O_3 occurs exclusively in the presence of high osmotic pressure and Ca^{2+}, resulting in bilayers that exhibit significantly higher lateral fluidity than those formed on planar SiO_2 and TiO_2 substrates. Molecular dynamics simulations show an association of the lateral fluidity with an enhanced separation between the DOPC bilayer and the Al_2O_3 surface, and furthermore attribute this phenomenon to electrostatic repulsion between the lipid headgroup and the positively charged Al_2O_3 surface. Bilayer formation on single Al_2O_3 nanopores successfully stopped the voltage driven transport of ions through the solid-state pore, resulting in a GΩ seal comparable in impedance to that of conventional BLMs. In addition, bilayer coated Al_2O_3 nanopores were stable in ionic solution for in excess of 50 hours, significantly more stable than BLMs (typical lifetime 6-10 hours). These results confirm that a positively charged Al_2O_3 solid-state nanopore interface is well suited for the formation of high impedance, highly mobile, mechanically stable lipid bilayers for potential biointegration with chemically sensitive protein channels.

5.2 Materials and Methods

5.2.1 Materials

The lipids used in these experiments were 1,2-di(cis-9-octadecenoyl)-*sn*-glycero-3-phosphocholine, 3-*sn*-phosphatidylcholine (DOPC) purchased, dissolved in chloroform, from Avanti Polar Lipids (Alabaster, AL) and Texas Red dihexadecanoyl-phosphoethanolamine (TR-DHPE), purchased from Invitrogen (California, USA) in the anhydrous power form. An alternative fluorescent lipid was also used in experiments, 1-palmitoyl-2-6-[(7-nitro-2-1,3-benzoxadiazol-4-yl)amino]hexanoyl-sn-glycero-3-phosphocholine (NBD-PC), also purchased, dissolved in chloroform, from Avanti Polar Lipids (Alabaster, AL). Unless otherwise noted, all experiments were conducted in buffer solutions consisting of 1 M KCl, 10 mM Tris-base, 5 mM $CaCl_2$ or 1 M KCl, 10 mM Tris-base, 5 mM EDTA adjusted to pH 8.0 using NaOH. High purity, deionized water (18 MΩ.cm) from a MilliPore MilliQ system (Bedford, MA) was used in all experiments.

5.2.2 Vesicle and Surface Preparation

Large unilamellar vesicles were prepared using the following protocol. Briefly, DOPC in chloroform was mixed with 1 mol % TR-DHPE and dried under a steady stream of N_2, followed by overnight desiccation under vacuum to remove any excess chloroform. Lipids were then hydrated in DI water at 4ºC to a final concentration of 1mg/ml. The large multilammelar vesicles obtained were extruded 31 times through a 400 nm pore size polycarbonate membrane filter (Avanti Mini-Extruder from Avanti Polar Lipids). Where stated, 1 mol % NBD-PC fluorescent lipid was substituted in place of 1 mol % TR-DHPE in certain vesicle preparations. Vesicles were generally used within 1-3 days of preparation.

Planar Al_2O_3 surfaces were prepared by first cleaning glass cover slips (Corning) in 1:1 H_2SO_4:H_2O_2 for 15 minutes followed by atomic layer deposition of 200 Å of Al_2O_3 using a

Cambridge Nanotech Savannah 200 reactor operated at 250°C. TiO_2 surfaces were prepared using the same cleaning process followed by deposition of 250 Å of TiO_2 using a Lesker PVD 75 sputter system at an RF power of 300W at 25°C. SiO_2 surfaces were used as is. The material composition of these surfaces was confirmed using X-ray photoelectron spectroscopy (XPS). Surface roughness and surface uniformity were studied using AFM.

5.2.3 Vesicle Fusion and Bilayer Formation

Prior to vesicle fusion, all surfaces were treated in a 100 W O_2 plasma for 1 minute to render the surfaces hydrophilic and immediately bonded to a PDMS microfluidic channel with a volume of 9 μl. Within 20 minutes of the O_2 surface treatment, vesicles were introduced into the microfluidic system and incubated on the various surfaces for 2 hours at room temperature. Following incubation, a 10 min DI rinse at a flow rate of 5 μl/min was used to remove any excess vesicles and surface debris resulting in the presence of high density SVLs on Al_2O_3 and TiO_2 surfaces. To transition SVLs on planar Al_2O_3 and TiO_2 to SPBs, a 10 min perfusion using 1 M KCl, 10 mM Tris, 5 mM $CaCl_2$, pH 8.0 buffer at a high flow rate of 10 μl/min was used resulting in the formation of highly fluid bilayers on all surfaces examined. Excess Ca^{2+} following bilayer formation was removed by rinsing with 1 M KCl, 10 mM Tris-base, 5 mM EDTA, pH 8.0. This same process was used to form fluid lipid bilayers on Al_2O_3 nanopore sensors.

5.2.4 Fluorescence Recovery After Photobleaching (FRAP)

Fluorescence imaging and FRAP measurements were conducted on a Zeiss LSM 710 Multiphoton Confocal Microscope equipped with a 561 nm 2 mW laser. Diffusion coefficients were determined by momentarily bleaching a spot of diameter ~50 μm containing fluorescently labeled lipids using a laser beam from a 2.5 W mixed gas Ar+/Kr+ laser (Stabilite 2018, Spectra Physics). Samples were irradiated at 568.2 nm with 100 mW of power for several seconds. The photobleached spot was measured as a function of time using time-lapse imaging and subsequently processed using Zen 2008 and ImageJ software. The fluorescence intensity of the bleached spot was determined after background subtraction and normalization. Using the method

of Kapitza with minor corrections for the finite bleach time,[176] the diffusion coefficients of the dye-labeled lipids on the various surfaces examined were determined.

5.2.5 Molecular Dynamics Simulations

Simulations of lipid–surface interactions:

Atomic-scale models of four solid-state membranes, having surface charge densities of –1, 0, +1, or +2 *e*/nm^2 and each containing a nanopore, were created by the methods described in the supplementary information. To neutralize the –1, +1, and +2 *e*/nm^2 surfaces, 280 K^+ ions, 280 Cl^- ions, and 560 Cl^- ions were added within 0.5 nm of the surfaces. Subsequently, a lipid bilayer consisting of 292 DOPC lipids was added to fill the *xy* plane above each of the four differently charged solid-state surfaces; the headgroups of the lipids in the nearest leaflet of bilayer were on average separated from the surfaces by 1.0 nm. The solid-state membrane and lipids were then immersed in water molecules and 1.0 M KCl solution to form complete systems of ~220,000 atoms, which each measured about 23.2 nm along the *z* axis after equilibration at 1 atm of pressure.

Following energy minimization, the four systems were then simulated using NAMD[177] with a 2 fs timestep, multiple timestepping, particle-mesh Ewald electrostatics,[178] and periodic boundary conditions along all three axes. The SETTLE algorithm[179] was used to enforce the rigidity of water molecules; the RATTLE algorithm[180] enforced rigidity of all other covalent bonds involving hydrogen atoms. Interactions among the lipids, water, and ions were computed using the CHARMM27 force field.[181] The interactions between atoms of the system and the silicon and oxygen atoms of the membrane were calculated using the force field of Cruz-Chu et al.,[182] except that the charges of some oxygen atoms were modified as discussed above. Lennard-Jones interactions and explicit pairwise electrostatic forces were computed with a smooth 0.7–0.8 nm cutoff. The pressure was maintained at 1 atm using a Nosé–Hoover Langevin piston pressure control[183]; the temperature was maintained at 295 K by applying a Langevin thermostat (damping constant of 1 ps^{-1}) to the atoms of the solid-state membrane only. To maintain the area of per lipid at 0.72 nm^2, the pressure control modified the system size only along the *z*

direction.[184] The generation of the solid-state membrane and lipid diffusivity calculations are described in the supplementary material.

5.3 Results and Discussion

5.3.1 Bilayer Formation on Al_2O_3 Surfaces

Lipid bilayers were formed on planar Al_2O_3 surfaces through the fusion and rupture of 400 nm extruded DOPC vesicles containing 1 mol % Texas Red DHPE fluorescently labeled lipid. Vesicles were formed by rehydration of a lipid cake in DI water as described in the experimental section. Figure 27a is a schematic of the microfluidic setup used in these experiments. Surfaces were O_2 plasma treated for 1 min at 100 W prior to vesicle incubation with surface hydrophilicity being confirmed through contact angle measurements (supplementary material). The incubation of vesicles on planar Al_2O_3 surfaces in the presence of DI water alone resulted in the formation of high density, immobile SVLs confirmed by the lack of fluorescence recovery seen in the photobleached spot (figure 27b) in fluorescence recovery after photobleaching (FRAP) experiments.[185] This result is consistent with previous reports that suggest Al_2O_3 is incompatible with bilayer formation due to low vesicle-substrate adhesion energy, resulting in the formation of intact, stable SVLs.[171, 172] To induce the formation of fluid lipid bilayers on Al_2O_3 following vesicle incubation, surfaces were perfused in a 1 M KCl, 10 mM Tris, 5 mM $CaCl_2$, pH 8.0 solution followed by a 1 M KCl, 10 mM Tris, 5 mM EDTA, pH 8.0 solution to remove any excess Ca^{2+} (flow rates of 10 μl/min). The presence of DI inside the vesicle versus high ionic strength solution outside (1 M KCl) induced an osmotic gradient across the vesicle membrane. Osmotic pressure and the presence of Ca^{2+} in turn induced the transition of a high density SVL on Al_2O_3 to a highly fluid lipid bilayer as shown in the line profiles of figure 27c. Ca^{2+} is known to bridge the negatively charged phosphate groups in DOPC,[186] while accelerating vesicle adsorption on metal oxide surfaces.[187] Osmotic pressure has also been reported to cause compressive stress and vesicle deformation, resulting in stress induced rupture and bilayer formation.[167] Fluorescence recovery as a function of time on Al_2O_3 is illustrated in figure 28a.

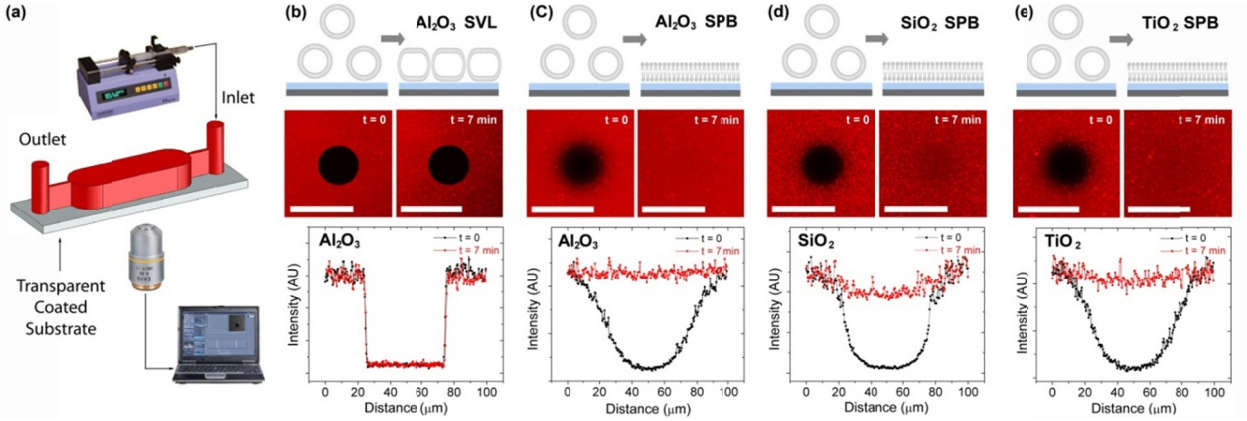

Figure 27 (a) Schematic of the experimental setup showing the microfluidic channel bonded to planar, coated, transparent substrates mounted on a confocal microscope. (b) Vesicle fusion on planar Al_2O_3 surfaces in the presence of DI water only. A 50 μm spot was photobleached and then reimaged 7 min later. The fluorescence intensity profile at t = 0 and t = 7 min shows no fluorescence recovery, consistent with the formation of an immobile SVL. (c) Vesicle rupture on planar Al_2O_3 surfaces in the presence of high salt (1M KCl, 10mM Tris, pH 8.0) and Ca^{2+}. Clear fluorescence recovery is observed in the photobleached region after 7 minutes confirming that osmotic pressure and Ca^{2+} induce the formation of a fluid, supported phospholipid bilayer (SPB) on Al_2O_3. (d) Fluorescence recovery on a control SiO_2 surface in the presence of high salt and Ca^{2+}. (e) Fluorescence recovery on a control TiO_2 surface in the presence of high salt and Ca^{2+}, again confirming the formation of a SPB. Scale bars in (b) – (e) are 100 μm.

To ensure that the transition from SVL to SPB on Al_2O_3 was not due to electrostatic interactions between Ca^{2+} and the net negatively charged fluorescent lipid used in these experiments (1% TR-DHPE in DOPC vesicles), we replaced TR-DHPE with a zwitterionic fluorescent lipid molecule (NBD-PC), and the formation of highly mobile lipid bilayers on Al_2O_3 was still observed as seen in figure 28b. The bilayer formation process reported here was also tested on planar SiO_2 and TiO_2 control surfaces as seen in figures 27d and 27e respectively, again resulting in the formation of highly fluid bilayers. These results confirm that although surface-lipid adhesion alone is insufficient to directly induce vesicle rupture on Al_2O_3, this material does indeed support fluid lipid bilayers in the presence of osmotic pressure and Ca^{2+}.

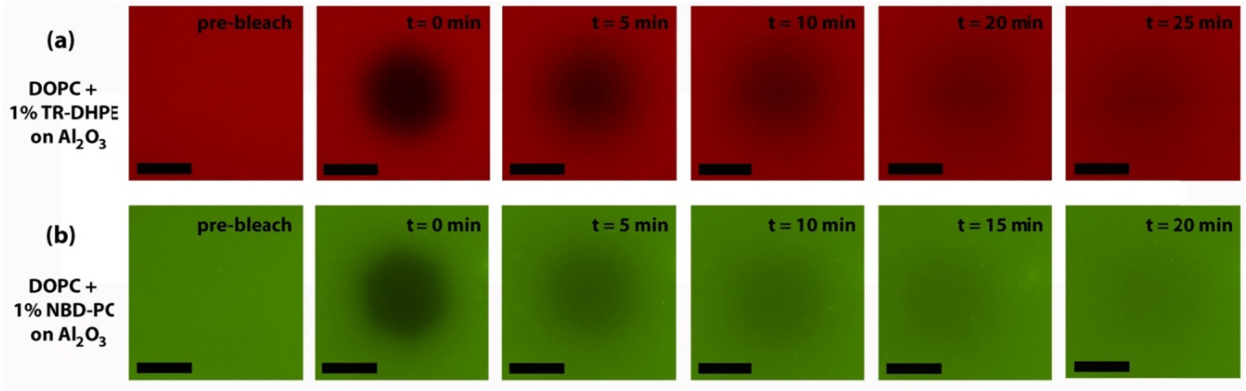

Figure 28 Qualitative FRAP results on Al_2O_3 (scale bar is 100 μm in all images). 400 nm extruded DOPC vesicles containing 1% fluorescent lipid were incubated and ruptured on the Al_2O_3 surface using osmotic pressure and Ca^{2+} to form fluid bilayers. (a) Negatively charged TR-DHPE fluorescent lipid; clear fluorescence recovery is seen in the photobleached region. (b) Zwitterionic (net neutrally charged) NBD-PC fluorescent lipid, clear fluorescence recovery is seen in the photobleached region. Results confirm that bilayer formation on Al_2O_3 is dependent on enhanced DOPC lipid-lipid interactions and DOPC-surface interactions in the presence of high salt and Ca^{2+} and is independent of the fluorescent lipid molecule used.

5.3.2 Lipid Diffusion Kinetics on Planar Surfaces

The diffusion kinetics of lipids in SPBs is a strong indicator of surface hydration. The presence of a 1-3 nm thick interfacial aqueous layer is essential to maintaining the functionality of membrane proteins, particularly transporters. For this reason, the kinetics of lipid diffusion on planar Al_2O_3, TiO_2, SiO_2 and PDMS surfaces was investigated using quantitative FRAP analysis. Figure 29a presents typical fluorescence recovery curves from DOPC bilayers formed on each surface, the fastest recovery being observed on Al_2O_3 and the slowest recovery on SiO_2. The diffusion coefficients of the dye-labeled lipid in each case were extracted by fitting a single exponential to each curve in accordance with the method of Kapitza (see materials and methods).[176] Lipid diffusion coefficients, fit error, rms surface roughness, and water contact angle were measured for each substrate and are summarized in table 5.1. The results of table 3 confirm that lipid diffusivity is highest on Al_2O_3, followed by TiO_2, PDMS and SiO_2. The measured diffusion coefficients of 2.4 $\mu m^2/s$ and 1.75 $\mu m^2/s$ for TiO_2 and SiO_2 respectively are consistent with reported values of 2.5 $\mu m^2/s$ on TiO_2[188] and 1.4-2.0 $\mu m^2/s$ on SiO_2.[171]

Interestingly, lipid diffusivity on Al_2O_3 was significantly higher. This enhanced diffusivity is likely dependent on a combination of factors including surface topography, material composition, surface hydration and surface electrostatics. These parameters were investigated systematically as shown in figure 30.

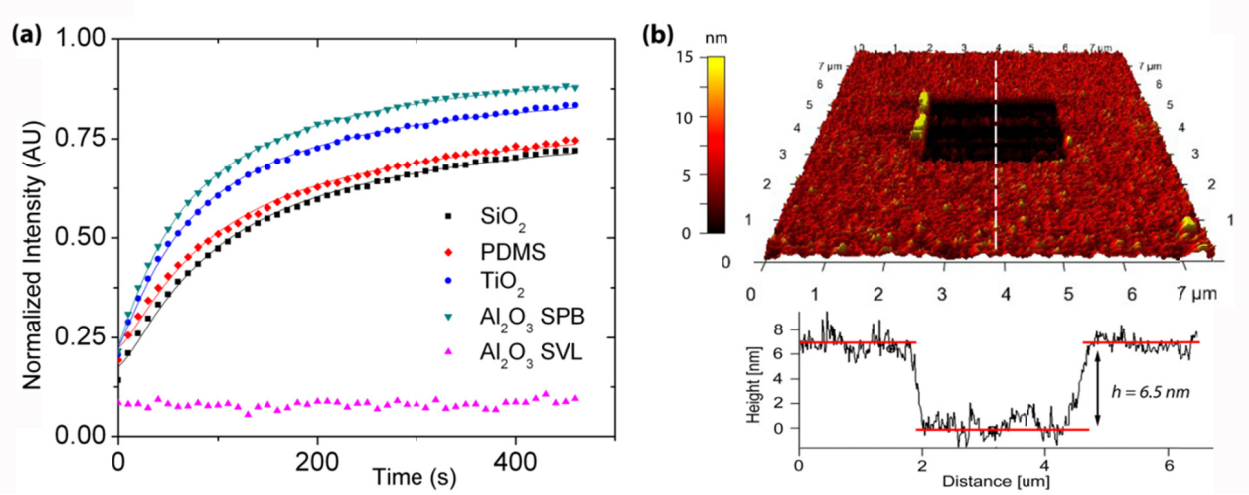

Figure 29 (a) Typical FRAP curves from DOPC bilayers formed on SiO_2, PDMS, TiO_2 and Al_2O_3 substrates in the presence of high salt and Ca^{2+}. Quantitative FRAP analysis shows faster recovery on Al_2O_3. Data is fitted using the theoretical Kapitza model (shown by the solid lines), with diffusion coefficients and fit residuals given in table 1. (b) Typical DOPC bilayer step height after bilayer formation on Al_2O_3, imaged using fluid AFM technique. A 2.5 x 2.5 µm region was scribed in the bilayer under high force (> 50 nN) using a SiN tip and then reimaged in tapping mode. Line profile through the scribed region gave a step height of 6.5 ± 1 nm, confirming the formation of a single DOPC bilayer.

Table 3 Summary of results showing the rms roughness and water contact angle, θ, on planar Al_2O_3, SiO_2, TiO_2 and PDMS surfaces. Also shown are the diffusion coefficients of TR-DHPE fluorescent lipid in DOPC bilayers formed on these surfaces. The method of Kapitza was used for data fitting with R^2 fit values as shown.

	Al_2O_3	**SiO_2**	**TiO_2**	**PDMS**
***rms* roughness (nm)**	241	152.2	941	-
θ (deg)	< 5°	< 5°	< 5°	< 5°
D (µm²/s)	2.7	1.75	2.4	1.8
R^2	0.999	0.996	0.998	0.996

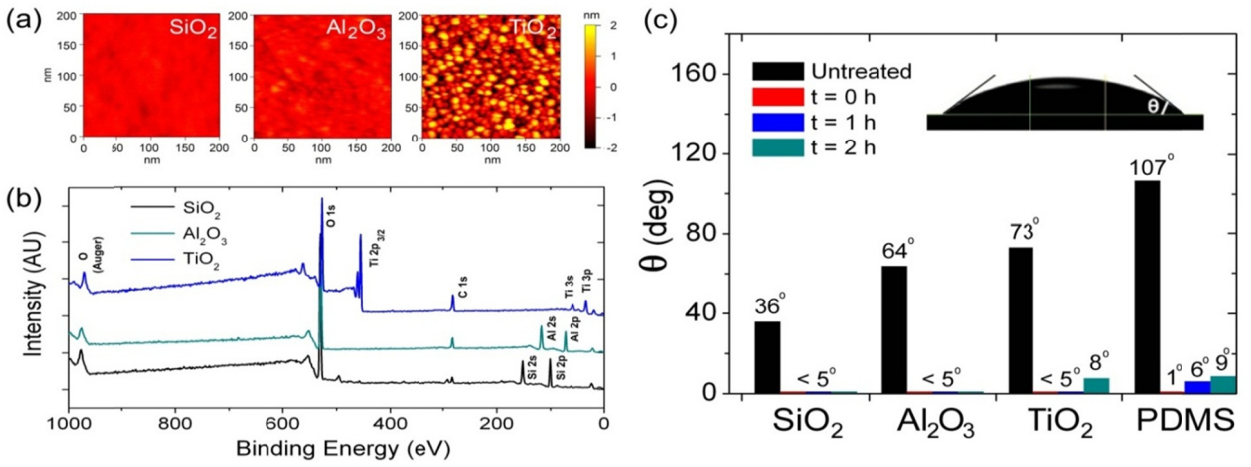

Figure 30 (a) AFM scans of SiO_2, ALD deposited Al_2O_3 and sputtered TiO_2 with rms roughnesses of 152 pm, 241 pm and 941 pm respectively. Lipid diffusion coefficients of 1.75 $\mu m^2/s$, 2.7 $\mu m^2/s$ and 2.4 $\mu m^2/s$ were extracted on these surfaces respectively suggesting that on the sub-nanometer scale, the chemical properties of the substrate are more important than surface topography. (b) XPS spectra from SiO_2, Al_2O_3 and TiO_2 coated substrates confirming the correct composition of each substrate prior to vesicle incubation and rupture. (c) Water contact angle measurements on SiO_2, Al_2O_3, TiO_2 and PDMS before and after surface treatment with 1 min O_2 plasma at 100 W. Al_2O_3 substrates remained hydrophilic (contact angle of < 5°) even 3 hours after treatment.

To examine the role of surface topography, AFM was conducted (figure 30a) on each surface and revealed a significantly higher rms surface roughness for TiO_2 versus Al_2O_3 and SiO_2 substrates. Little correlation between surface roughness and lipid diffusion kinetics was observed. The material composition of all surfaces was verified using x-ray photoelectron spectroscopy (XPS) as shown in figure 30b, thereby ruling out the influence of surface contamination on lipid diffusion dynamics. To examine macroscopic differences in surface hydration, water contact angle measurements were conducted on bare substrates after an O_2 plasma treatment (1 minute at 100 W). The hydrophilicity of each substrate was similar (< 5° in all cases as shown in figure 30c).

Microscopic differences in DOPC bilayer thickness on Al_2O_3 versus SiO_2 were probed using fluid AFM. After bilayer formation on Al_2O_3, a 2.5 μm square region in the bilayer was scribed

in contact mode under high force (> 50 nN), sufficient to scrape through the bilayer as demonstrated by Kumar and Hoh.[189] The area encapsulating the scribed region was then reimaged at low force in tapping mode resulting in the AFM scan shown in figure 29b. A line profile through the scribed region revealed a step height of 6.5 ± 1 nm, corresponding to the thickness of a single bilayer. DOPC bilayers formed on Si_3N_4 and mica typically exhibit thicknesses of 4.6 nm[190] and 5.6 nm respectively, confirmed through fluid AFM studies. The increased DOPC bilayer thickness on Al_2O_3 suggests the possible presence of a thicker hydration layer. NMR studies using phosphatidylcholine lipids in anodic aluminum oxide (AAO) templates confirmed the existence of a substantially thick, 3 nm trapped water layer between the bilayer and the alumina substrate,[191] in comparison to the 1 nm water hydration layer typically reported on SiO_2. It is likely that this thick hydration layer reduces lipid-substrate interactions, resulting in the enhanced bilayer fluidity observed on Al_2O_3. Note that these AFM height measurements also exclude the possibility of stacked bilayers on Al_2O_3 which typically result in step heights of >10 nm.[163]

5.3.3 The Influence of Surface Charge

To examine the role of surface electrostatics on surface hydration, a series of molecular dynamics simulations were carried out. The simulation protocols are described in detail in the experimental methods, the general methodology is reviewed by Aksimentiev et al. Briefly, an atomistic model of an amorphous solid-state membrane was created, which contained a nanopore to permit the passage of water and ions in and out of the interfacial water layer. Surfaces of differing charge densities (–1, 0, +1, and +2 e/nm^2) were generated by shifting the charge on oxygen atoms at the membrane surface. This ensured that the positions of atoms of the solid-state surface were identical in all simulations, thereby eliminating the effects of surface roughness while probing only electrostatic effects. The simulated charge densities were consistent with reported values for SiO_2 and Al_2O_3. Hydrated SiO_2 surfaces typically exhibit a surface charge density of –1 e/nm^2 at pH 8.0 due to the deprotonation of surface silanol groups, in contrast to ALD Al_2O_3 surfaces which have been shown to carry a positive charge under similar conditions with charge densities in excess of +1 e/nm^2. The four complete systems, each consisting of a

DOPC bilayer, water, ions, and a solid-state membrane containing a nanopore, were simulated to observe the evolution of both the DOPC bilayer and the interfacial water layer as a function of time.

Figure 31 illustrates the position of the DOPC bilayer relative to the solid-state membrane at various time points during the simulation for the negatively charged (–1 e/nm^2) and positively charged (+2 e/nm^2) surfaces. An initial lipid-surface separation of 1.0 nm was assumed at the start of each simulation. Within 15 ns, the DOPC bilayer was seen to make contact with the negatively charged (–1 e/nm^2) surface, followed by complete collapse of the bottom bilayer leaflet by t = 100 ns, leaving only scattered pockets of interfacial water with a density of ~14 molecules/nm^2. In contrast, the bilayer receded from the positively charged surface at t = 15 ns and continued receding through to t = 100 ns. Figure 31b plots the average separation between the DOPC bilayer and the substrate as a function of time for each simulated system. For charge densities of 0 and -1 e/nm^2, the average separation between the DOPC bilayer and the surface diminished rapidly in comparison to positively charged surfaces (+1 and +2 e/nm^2) which showed a slow increase in lipid–surface separation. The surface charge dependent motion of the bilayer on -1, 0 and +2 e/nm^2 surfaces is illustrated in the movies provided in the supplementary material.

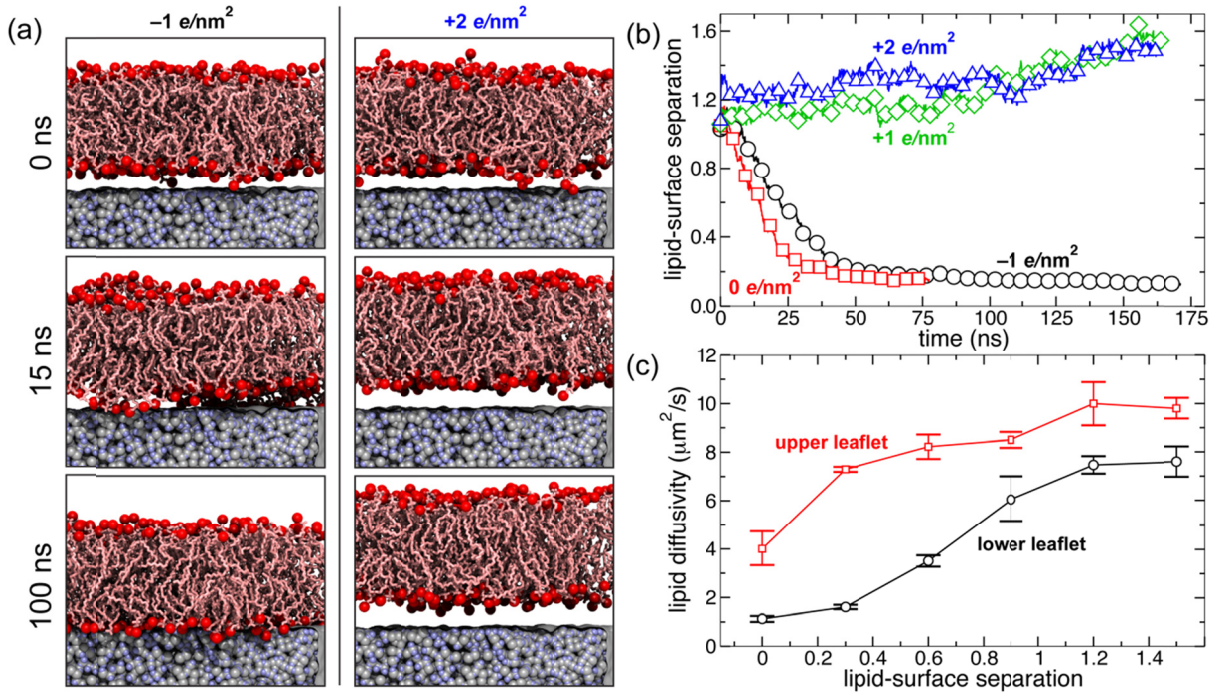

Figure 31 Molecular dynamics simulations of the interaction between a DOPC bilayer and solid-state surfaces of varying surface charge densities. (a) Snapshots illustrating the position of the DOPC bilayer over a negatively (left) and positively (right) charged surface at various time points during molecular dynamics simulations. The complete system contained a bilayer with a lateral area of 105 nm^2; only a portion is shown in these snapshots. The choline groups are shown as red spheres; the rest of the DOPC molecules are drawn as pink tubes. The atoms of the synthetic membrane are shown by gray and blue spheres. Water and ions are not shown. (b) The average separation between the DOPC lipid bilayer and the solid-state surface as a function of time. (c) Diffusivity of the DOPC lipids in the plane of the bilayer as a function of the separation between the lipid and the solid-state surface.

To verify that these results were robust, the simulations were repeated using different initial conditions, yielding similar results, as shown in figure 32a. Moreover, three additional simulations showed repulsion of the bilayer from the surface when the surface charge was instantaneously changed from either –1 e/nm^2 or 0 e/nm^2 to +2 e/nm^2 during simulations, as shown in figure 32b.

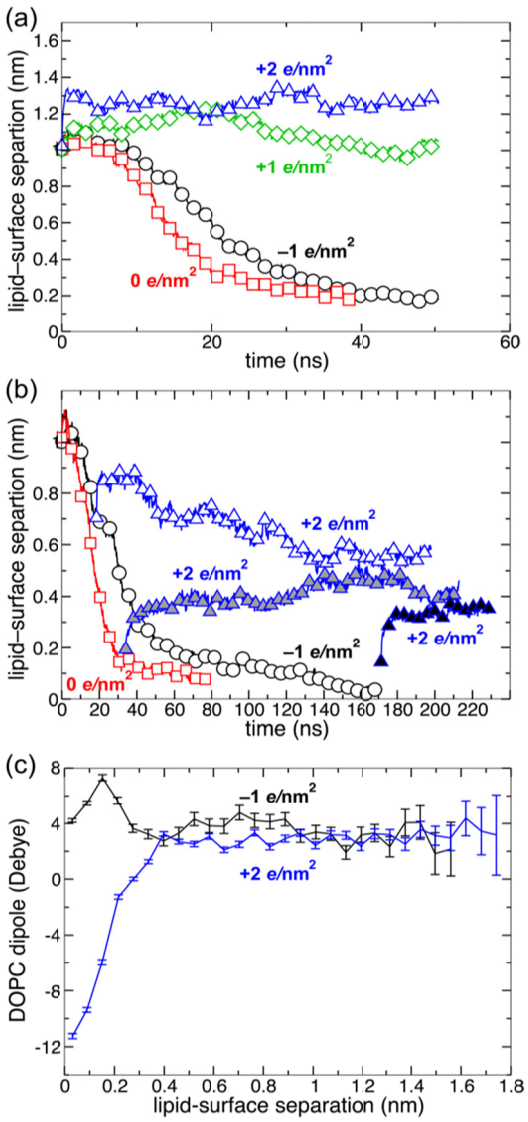

Figure 32 (a) The average separation between the DOPC lipid bilayer and the solid-state surface as a function of time for the four differently charged surfaces. The simulations characterized here were identical to those used to produce figure 5.4b, except that the atoms began with a different set of random velocities. (b) The average separation between the DOPC lipid bilayer and the solid-state surface as a function of time in three simulations in which the areal charge density of the membrane was changed to +2 e/nm^2 from an initial value of either –1 e/nm^2 or 0 e/nm^2 during the simulation. The original simulations from which the initial conditions were derived are also shown. The results seem to suggest electrostatic repulsion between the bilayer and the positively charged +2 e/nm^2 surface at close distances. (c) The component of the electric dipole moment of the DOPC headgroup perpendicular to the plane of the bilayer as a function of the distance between the lipids and the solid state surface. The data for two different surfaces are shown. The dipole points away from the bilayer when the bilayer is far from either surface. However, the dipole reverses direction when the bilayer is placed near the positive surface.

Our results suggest that the thickness of the hydration layer is dependent on electrostatic interactions between the surface and the DOPC head group. For an isolated DOPC bilayer, the headgroup of the lipid has an electric dipole moment pointing outward from the bilayer surface due to the equilibrium orientation of the positively charged choline group and negatively charged phosphate group.[184] We calculate a dipole moment of 2.9 ± 0.2 Debye normal to the surface for a DOPC headgroup in an isolated bilayer, in agreement with Siu et al.[184] Thus, the bilayer should be attracted to bare or negative surfaces, and repelled from positively charged surfaces, which is consistent with the bilayer motion seen in figure 31b. Figure 32c shows the average electric dipole of the DOPC headgroup along the direction normal to the bilayer. For bilayer-surface separations > 0.4 nm, this dipole maintained the isolated value of 2.9 ± 0.2 Debye. For smaller separations, the charge of the surface causes a change in the conformation of the headgroup moieties and, consequently, a change in the electric dipole moment of the headgroup. When the DOPC bilayer is forced < 0.3 nm from a positively charged surface, the dipole moment of the headgroup is reversed. This conformational change is likely not energetically favorable and explains the repulsion of the bilayer from the positively charged surface in charge reversal simulations. Interestingly, DOPC bilayers also showed an attraction to neutrally charged surfaces in our simulations. This is because annealing the model membranes results in the migration of negatively charged oxygen atoms to the surface, giving the neutral surface a negative surface dipole which in turn electrostatically attracts the bilayer. The simulated surfaces used in these studies do not serve as precise models of experimental SiO_2 and Al_2O_3 surfaces, which would be difficult to create given the lack of knowledge about the atomic structure of the surfaces and their interactions with DOPC lipids. The simulations were intended to show that differences in the surface charge properties of the two materials may be predominantly responsible for differences in hydration layer thickness. The equilibrium separation between an SiO_2 surface and a DOPC bilayer has been reported to be ~1.0 nm, while our simulations showed a much smaller equilibrium separation. This discrepancy could be due to topographic features of the surface such as surface roughness, affecting the measured separation. Furthermore, the relatively small size of the MD system (105 nm^2) may have suppressed long-range fluctuations of the lipid surface, which would also contribute to a larger measured separation in experiments.

We also investigated the effect of lipid-surface separation on the diffusion kinetics of the lipids in both the upper and lower (nearer to the surface) bilayer leaflets. The diffusivity values were calculated using a protocol similar to Siu et al.[184] Figure 31c shows that the lipid diffusivity in the plane of the bilayer increases with increasing lipid-surface separation in all simulations. Both leaflets showed this trend, although the diffusivity was observed to be considerably less in the lower leaflet. These results suggest that DOPC bilayers in equilibrium above a positively charged surface should show higher lipid diffusivities than those above negatively charged surfaces due to a larger lipid-surface separation. Diffusivities of 1.1 ± 0.2 and 6.4 ± 0.8 $\mu m^2/s$ for lower and upper leaflets were calculated respectively from simulations of the –1 e/nm^2 surface at times >50 ns. For the +2 e/nm^2 surface at times >50 ns, we obtained much larger values for these diffusivities: 7.2 ± 2.2 and 11.9 ± 2.5 e/nm^2 respectively. The diffusivity determined here for large lipid-surface separations agrees well with previous MD simulations.[184] Quantitative comparisons between the lipid diffusion coefficients calculated in simulations and those measured in our experiments are complicated by the fact that diffusivity was measured experimentally by observing the motion of TR-DHPE, whose bulky fluorophore likely reduced its diffusivity with respect to the DOPC lipids surrounding it. Differences in the surface roughness of the simulated and experimental surfaces, and the presence of the pore in simulations, could also contribute to differences in the measured and simulated diffusivities.

5.3.4 Al_2O_3 Nanopore Fabrication and Characterization

The solid-state nanopore fabrication process used herein builds on work from chapters 3 and 4. Briefly, a Si support chip containing a single low-stress, mechanically stable 45 ± 5-nm-thick amorphous Al_2O_3 membrane was fabricated using standard microfabrication processes as described in the materials and methods. A schematic of the nanopore chip is shown in figure 33a. TEM cross sectional analysis and energy dispersive X-ray spectroscopy (EDS) confirmed the thickness and composition (containing only Al and O) of free-standing membranes as shown in figure 33b. Nanopores of varying diameter were formed in these Al_2O_3 membranes using a focused electron beam from a JEOL JEM2010F field-emission TEM operated at 197 kV. Figure 33c shows a schematic of the pore formation process along with TEM phase contrast images of 5 nm, 7 nm and 9 nm diameter nanopores used in these experiments.

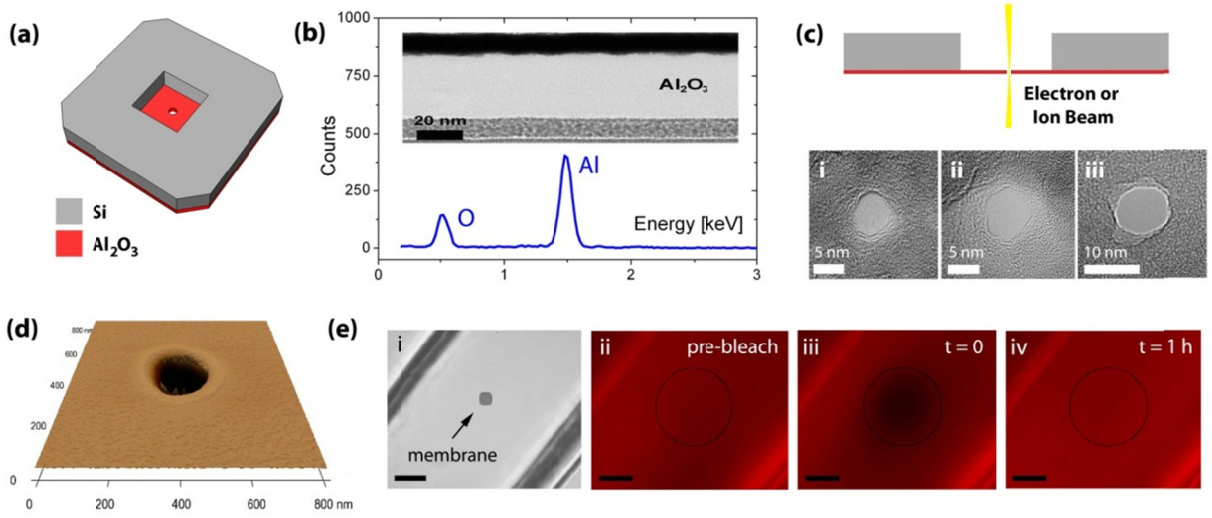

Figure 33 (a) Schematic of a nanopore chip from the backside; the 30 x 30 μm, 300 μm deep trench in the Si handle layer supports a free-standing Al_2O_3 membrane in which a nanopore is formed. (b) EDS spectrum from the free-standing membrane confirming the presence of only Al and O. (Inset) Cross sectional TEM image of the membrane showing a thickness of 45 ± 5 nm. (c) Schematic of the nanopore formation process using a convergent electron or ion beam. (i-iii) TEM phase contrast images of a 5 nm, 7 nm and 9 nm diameter Al_2O_3 nanopore formed using electron beam based decompositional sputtering. (d) AFM scan of a typical FIB 200 nm pore used in bilayer experiments. (e) Bilayer integration on solid-state nanopores (100 μm scalebar). (i) Bright field image of a 500 μm wide PDMS channel containing a membrane with a 200 nm nanopore. Fluorescence image after bilayer integration on the nanopore chip (ii) prior to photobleaching the circular target region, (iii) immediately after photobleaching, (iv) 1 hour after photobleaching, showing complete fluorescence recovery.

The shot noise in the pore region confirms that the electron beam has completely sputtered through the membrane with the pore quenching in size upon removal of the electron beam. Small Al_2O_3 nanopores formed using this process are well suited for single molecule DNA analysis. Larger nanopores were formed in free-standing Al_2O_3 membranes using a FEI DB235 focused ion beam tool.

Figure 33d is an AFM scan of a typical ~200 nm pore used in bilayer integration experiments. After fabrication, nanopore chips were O_2 plasma treated (100 W for 1 minute) to render the surface hydrophilic and immediately mounted into a PDMS flow cell into which vesicles were injected and incubated. Figure 33e (i) shows a bright field image of a 500 μm PDMS channel aligned and chemically bonded to an Al_2O_3 nanopore chip containing a single 200 nm nanopore,

centered on a 30 µm x 30 µm free-standing membrane. A complete cross-sectional view of the experimental setup is provided in figure 34a. After vesicle incubation, the surface was perfused using the previously described method (high salt, osmotic pressure and Ca^{2+}) to successfully form a fluid bilayer on the Al_2O_3 nanopore chip. Figure 33e (ii) – (iv) show qualitative FRAP results from the region containing the membrane/nanopore following the perfusion process. The fluorescence recovery observed in the photobleached region confirms the formation of a fluid lipid bilayer over the membrane/nanopore region, consistent with our results on planar Al_2O_3 surfaces. To determine the electrical characteristics of bilayer coated nanopores, ionic current through the pore was measured by placing Ag/AgCl electrodes in each reservoir, with the nanopore forming the only electrical/fluidic connection between the two reservoirs (figure 34a). The electrical characteristics are discussed in the following section.

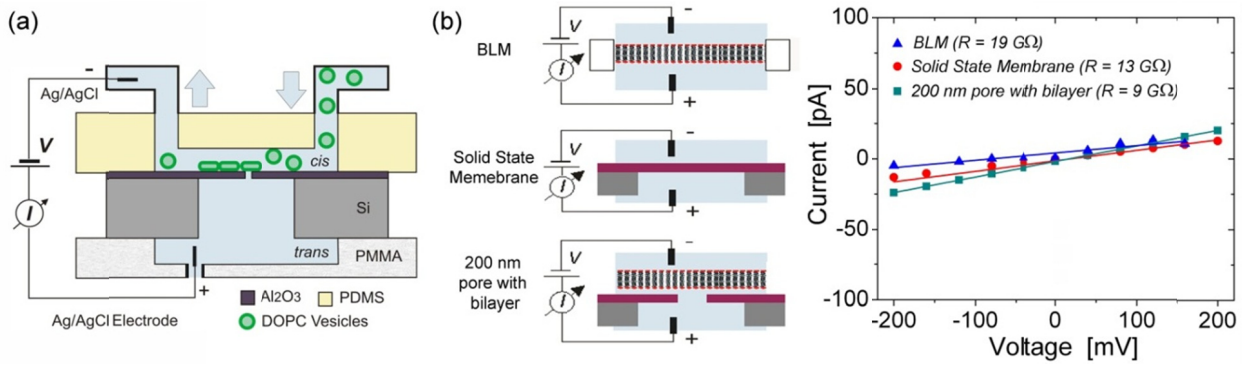

Figure 34 (a) Experimental setup used for typical electrical measurements integrating perfusion setup with nanopore chip. After vesicle incubation, DI perfusion followed by 1M KCl, 10 mM Tris, 5mM $CaCl_2$ pH 8.0 through this setup induced bilayer formation on Al_2O_3 nanopores. (b) Comparison of the electrical properties of a BLM formed in a Teflon aperture, solid-state membrane with no pore and a bilayer grafted Al_2O_3 nanopore. IV characteristics were fitted to extract a resistance that is comparable in all three cases, confirming that a GΩ seal is achieved using a bilayer grafted Al_2O_3 nanopore.

5.3.5 Lipid Bilayer Coated Al_2O_3 Nanopore Sensors

Monitoring single ion channel activity in lipid bilayers requires a membrane resistance that is in excess of 1GΩ. The electrical performance of DOPC bilayers grafted on Al_2O_3 nanopore substrates was characterized using AC impedance spectroscopy and DC current measurements as illustrated in figures 35a and 35b respectively. The impedance of a 200 nm nanopore prior to

vesicle fusion and rupture is shown by the black curve of figure 35a. Pore resistance in 1 M KCl, 10 mM Tris, pH 8.0 electrolyte is estimated at several hundred kΩ to 1 MΩ. Following vesicle fusion and rupture, the pore impedance significantly increases into the GΩ range consistent with the formation of a defect-free, pore spanning lipid bilayer. Figure 35a also compares the impedance of a bilayer grafted Al_2O_3 nanopore sensor with the impedance of traditional painted BLMs and solid state membranes containing no nanopore. The impedance of all three systems is comparable and in the GΩ range. DC measurements revealed a resistance of ~9 GΩ for bilayer grafted Al_2O_3 nanopores in comparison to BLM and solid-state membrane resistances of 19 GΩ and 13 GΩ respectively (figure 34b). These values are in good agreement with impedance spectra from DPhPC supported bilayers formed on AAO templates[192] and nano-BLMs formed using the painting method on functionalized gold coated AAO substrates.[193] An order of magnitude improvement in bilayer resistance is observed over bilayers formed through vesicle fusion on mercaptan coated gold surfaces.[194] The authors attribute the low bilayer resistance on mercaptan coated gold to incomplete surface coverage and bilayer defects during vesicle fusion. These defects were not observed in bilayers formed on Al_2O_3 at high vesicle concentrations, likely due to the formation of a high density SVL prior to the transition to a supported bilayer.

Figure 35b overlays the current-voltage (IV) characteristics of open 5 nm, 7 nm and 9 nm diameter Al_2O_3 solid-state nanopores (pore resistances of 104 MΩ, 62.5 MΩ and 29.4 MΩ respectively), with the IV characteristics of a 200 nm diameter Al_2O_3 nanopore supporting a fluid DOPC bilayer (resistance of 9 GΩ). The fluid DOPC bilayer prevents ion transport through the 200 nm diameter Al_2O_3 nanopore, resulting in an ionic current that is orders of magnitude less than that observed through even a small, 5 nm Al_2O_3 nanopore. Exclusively large ~ 200 nm pores were used in bilayer formation experiments for two reasons: (1) to rule out any possibility of pore clogging with lipid molecules (biomolecule clogging is observed during DNA or protein translocation experiments through very small Al_2O_3 nanopores) and, (2) to maximize the probability of membrane protein insertion in experiments seeking to incorporate α-hemolysin. Figure 35c illustrates a typical noise power spectrum from a ~7 nm nanopore showing strong low frequency 1/f noise characteristics. 1/f noise in solid state nanopores is attributed to two mechanisms: fluctuations in the total number of charge carriers (ions) through the nanopore and fluctuations in ion mobility due to electrostatic trapping at surface sites. As expected in the case

of a BLM, low frequency 1/f noise is not observed as the membrane is impermeable to ions. Interestingly, 1/f noise is also not observed in current measurements through a bilayer spanning Al_2O_3 nanopore. This is again due to negligible ion flow across the hybrid biological/solid-state membrane, further confirming the formation of a high impedance seal.

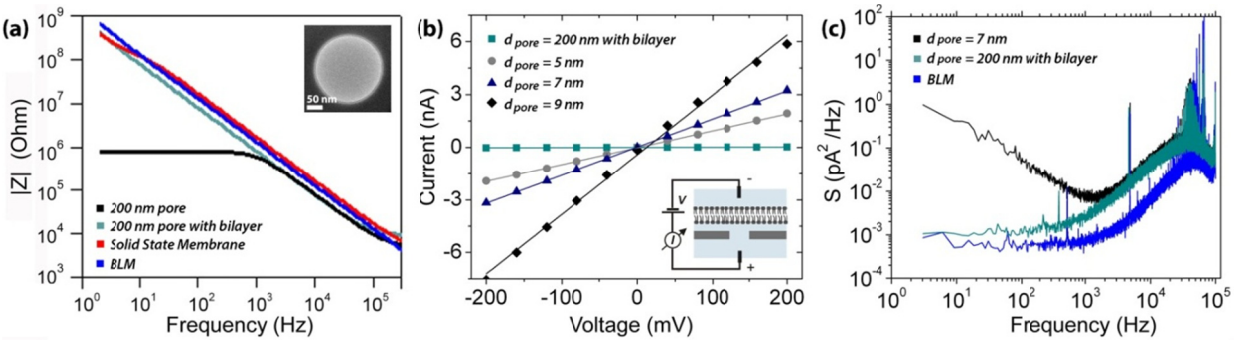

Figure 35 (a) Impedance spectra from a 200 nm Al_2O_3 nanopore before and after bilayer integration. Following bilayer formation, a GΩ seal is achieved comparable in magnitude to the impedance of a painted BLM and a solid-state membrane with no pore. (Inset) TEM image of the 200 nm pore prior to bilayer formation. (b) IV characteristics of a bilayer coated 200 nm Al_2O_3 nanopore (R = 9 GΩ), relative to uncoated 5 nm (R = 104 MΩ), 7 nm (R = 62.5 MΩ) and 9 nm (R = 29.4 MΩ) diameter nanopores. (Inset) Schematic of the DC measurement setup; bilayer formation blocks ion flow through the pore. (d) Noise power spectrum from a 7 nm solid-state nanopore showing strong 1/f noise at f < 1kHz. Overlaid are power spectra from a BLM and a bilayer coated Al_2O_3 nanopore. 1/f noise is not observed in either spectrum confirming negligible current flow through the bilayer coated nanopore.

5.3.6 Stability of Bilayer Coated Al_2O_3 Nanopores

The suitability of classical BLMs in biosensor applications is limited by their short lifetimes (typically 6-10 hours), beyond which membrane rupture occurs. BLMs are also highly susceptible to mechanical shock and thermal fluctuations. The need for robust BLMs is most evident in biological nanopore based DNA sequencing approaches that require substantial membrane stability to achieve long read lengths. The DOPC bilayers formed in these experiments on single Al_2O_3 nanopores show excellent bilayer stability as illustrated in figure 36. GΩ impedances are maintained for over 50 hours as verified by the magnitude and phase plots of figures 36a and 36b respectively.

Prior to bilayer formation on the nanopore (t = 0^- hr), we observe a pore resistance of ~ 800 kΩ and a phase of 0° for f < 1 kHz, corresponding to the typical resistive behavior of a nanopore. Following the vesicle fusion and rupture process on the Al_2O_3 nanopore, at t = 0^+ hr, a clear shift in the magnitude and phase spectra is seen. The GΩ impedance and -90° phase shift near DC signify capacitive behavior corresponding to the formation of an electrically insulating, fluid bilayer. This capacitive behavior is maintained for over 50 hours and is comparable to the state-of-the-art in supported bilayers, more specifically, nano-BLMs that are capable of maintaining GΩ seals for over 30 hours[193] and POPC supported bilayers formed on functionalized AAO templates that are stable for over 50 hours.[192]

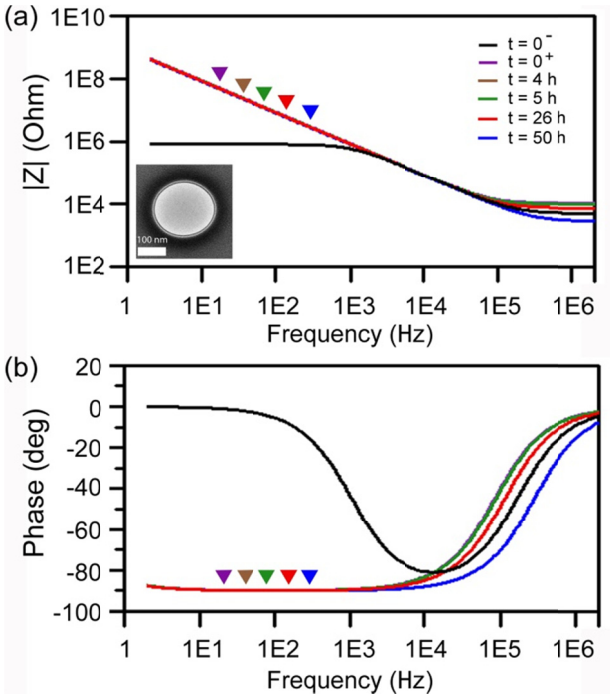

Figure 36 Stability of bilayer coated Al_2O_3 nanopores as a function of time. Impedance (a) magnitude and (b) phase. Prior to bilayer formation (t = 0^-), resistive behavior is observed (resistance of 800 kΩ and phase of 0°) at low frequencies, consistent with an open pore. Following bilayer formation (t = 0^+), capacitive behavior is observed (GΩ resistance and phase of -90° at low frequencies), confirming the formation of an electrically insulating bilayer membrane on the 200 nm nanopore. High pore impedance was maintained for over 50 hours, confirming the stability of this hybrid biological/ solid state membrane (Inset) TEM phase contrast image of a typical 200 nm pore used in bilayer integration experiments.

5.4 Chapter Summary

In summary, this chapter presents the formation of highly fluid, defect-free lipid bilayers on unmodified Al_2O_3 surfaces through vesicle fusion and applies this methodology to form high impedance, mobile bilayers on single Al_2O_3 nanopore sensors. Lipid bilayer formation on Al_2O_3 occurs exclusively in the presence of Ca^{2+} and high osmotic pressure, resulting in bilayers that exhibit significantly higher lateral fluidity than those formed on planar SiO_2 and TiO_2 substrates. Molecular dynamics simulations attribute the greater fluidity to a larger separation between the DOPC bilayer and the Al_2O_3 surface, which is in turn due to electrostatic repulsion between the headgroups of DOPC and the positively charged surface. AFM imaging has independently confirmed a 1.5–2.0 nm separation between the bilayer and Al_2O_3 surface. These results suggest that bilayer coated Al_2O_3 surfaces may be well suited for supporting membrane proteins, the thick interfacial water layer on Al_2O_3 permitting the integration of a broader range of membrane active peptides, while helping reduce protein immobilization and denaturation through surface contact. In the pharmaceutical and medical industries, such a platform would facilitate the screening of drugs specific to a broader range of membrane proteins in their native environment. Furthermore, lipid bilayers formed on Al_2O_3 nanopore sensors exhibit all the advantages of conventional BLMs and supported bilayers formed on SiO_2 (simple to form, GΩ electrical seals), but also exhibit enhanced mechanical stability (stable for over 50 hours) and increased fluidity relative to their supported bilayer counterparts. The bilayer integrated solid-state membrane platform reported in this work provides an important first step in the development of a hybrid biological solid-state nanopore. By integrating chemically selective ion channels and biological nanopores into this platform, this technology could find widespread use in medical diagnostics, drug screening and in next generation DNA sequencing.

Graphene-Al_2O_3 Nanopore Sensors 6

Graphene, an atomically thin sheet of carbon atoms densely packed into a two-dimensional honeycomb lattice, possesses remarkable mechanical, electrical and thermal properties.[58] The comparable thickness of a graphene monolayer to the 0.32-0.52 nm spacing between nucleotides in ssDNA makes this material particularly attractive for electronic DNA sequencing. The incorporation of graphene into nanopores was recently demonstrated by three groups.[59-61] In separate studies, the Golovchenko, Dekker, and Drndic labs reported on the electron-beam based fabrication of 5-25 nm diameter nanopores in suspended graphene films, prepared through either chemical vapor deposition (CVD) or exfoliation from graphite.[59-61] Nanopores were formed in as few as 1-2 monolayers of graphene, these membranes exhibiting remarkable durability and insulating properties in high ionic strength solution.[59]

In this chapter, we present the development of a novel, highly versatile graphene-Al_2O_3 nanopore platform for biomolecule sensing. These nanopores are highly robust, exhibit stable conductance values, show remarkable pH response and allow for the manipulation of ionic current through the nanopore via applied potentials at the graphene gate. This exciting graphene-Al_2O_3 nanopore platform can also be used to probe the sensitive transport of dsDNA, including DNA folding, and the detection of protein DNA complexes, specifically estrogen receptor α bound to its cognate DNA sequence. Many exciting possibilities are introduced in this chapter. In particular, a third electrode a few monolayers in thickness, positioned in the nanopore, not only allows for the manipulation of pore conductance, but may also serve to slow down or trap a DNA molecule in the pore, an exciting possibility that could help enable solid-state nanopore DNA sequencing. These new developments are discussed next.

6.1 Fabrication of Graphene-Al_2O_3 Nanopores

The fabrication of these novel structures is shown in figure 37. Graphene (g1 layer) was transferred onto a FIB milled 300 nm diameter aperture in an Al_2O_3 membrane. Graphene

growth was as follows: Graphene is grown on 1.4 mil copper foils using chemical vapor deposition (CVD).[195] After growth, graphene is transferred to receiving substrates by coating the graphene in a bilayer of PMMA (495K/950K), O_2 plasma etching of backside graphene, etching of the copper foil in 1M $FeCl_3$, rinsing the film in deionized water, and scooping it onto the substrate. PMMA is removed in a 1:1 solution of methylene chloride:methanol followed by a 400ºC anneal in an Ar/H2 environment.

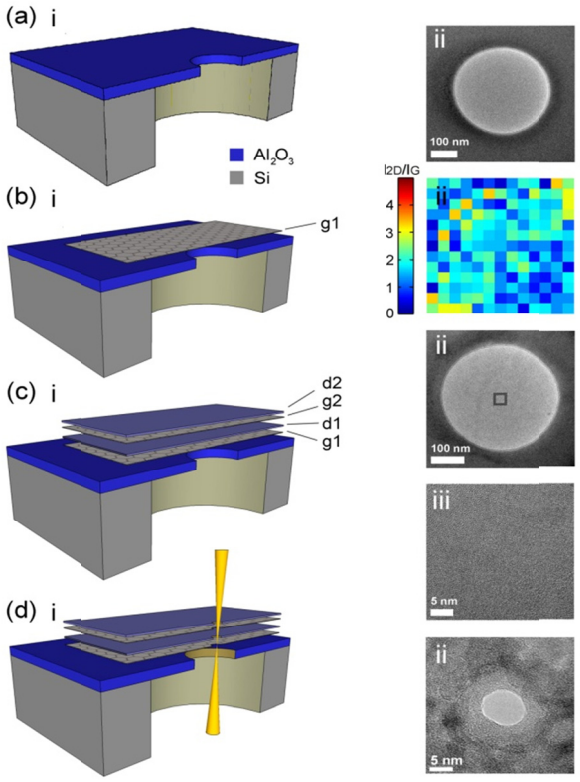

Figure 37 Graphene nanopore fabrication process. (a) Drill a 300 nm FIB hole in a 70 nm thick Al_2O_3 membrane. (b) Transfer CVD graphene to cover the aperture (3mm x 3mm graphene sheet - layer g1). (c) Evaporate < 2 nm Al as a seed layer and then deposit 6.5 nm of ALD Al_2O_3 (d1) on the chip. Transfer another graphene layer that extends to the edge of the chip for contacting (g2) and repeat Al/Al_2O_3 deposition (d2). (d) FEGTEM nanopore formation.

A small area graphene piece was transferred (3mm x 3mm) using this process so that it would not extend to the edge of the nanopore chip. Following the transfer process, Raman spectroscopy was used to confirm the presence of primarily monolayers on the substrate as expected using the CVD process on Cu.[195] Next a dielectric layer (d1) was deposited on g1 consisting of 2 nm evaporated Al as a seed layer, followed by 6.5 nm of ALD Al_2O_3. Graphene 1 (g1) provides a

robust structural support for d1. The second layer of graphene (g2) was next transferred using the above process, followed by another dielectric layer (d2) the same as d1. Graphene 2 (g2) forms the active or device layer that will be electronically biased and is thus insulated from the environment by sandwiching it between Al_2O_3 layers. Nanopores are formed in this gdgd stack using a focused electron beam as previously reported in chapters 3 and 4.

6.2 Electrical Characterization of Graphene-Al_2O_3 Nanopores

The current-voltage characteristics of graphene-Al_2O_3 nanopores are shown in figure 38a for pores of varying size in 1M KCl, 10mM Tris, 1mM EDTA, pH 8.

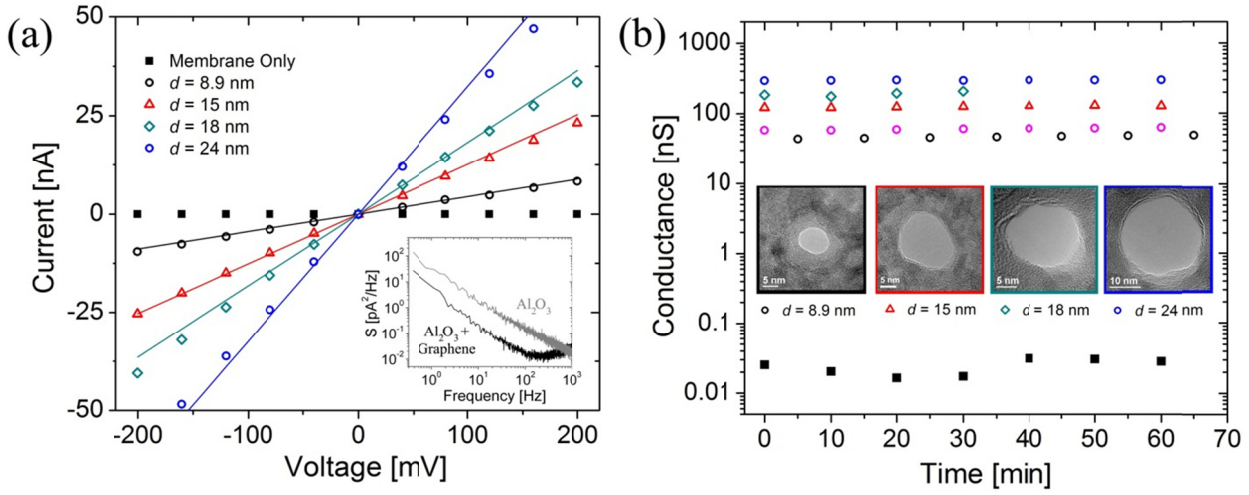

Figure 38 Graphene-Al_2O_3 nanopore electrical characterization. (a) IV characteristics of graphene-Al_2O_3 nanopores of varying size. Note that the membrane has near negligible conductance. Fitted data is numerically computed using above equations. (Inset) 1/f noise of graphene-Al_2O_3 nanopores is comparable to if not better than Al_2O_3 nanopores. (b) These membranes and nanopores give stable conductance values as shown.

Linear IV curves are generally observed suggesting a symmetric nanopore structure as previously reported for Al_2O_3 nanopores in chapters 3, 4 and 5. The IV characteristics of four pores of varying diameter are shown in figure 38a. Also shown are fits to the data constructed using numerical simulations. The mathematic model for ion transport through the pore involves

solving equations coupling ionic transport, electric potential and fluid flow. The details of this process are provided by Aluru et al. The total flux of the *ith* species (ion) is given by the following expression

$$\mathbf{\Gamma}_i = -D_i \nabla c_i - \Omega_i z_i F c_i \nabla \phi + c_i \mathbf{u} \tag{3}$$

where F is the Faraday's constant, z_i is the valence, D_i is the diffusion coefficient, Ω_i is the ionic mobility, $\mathbf{\Gamma}_i$ is the flux, c_i is the concentration of the ith species, $\mathbf{u}$ is the velocity vector of the fluid flow, and ϕ is the electrical potential. The three terms on the right-hand side of Eq. 2 define the fluxes due to diffusion, electromigration, and convection, respectively. The Nernst-Planck (NP) equation describes the transfer of each dissolved species and is given by:

$$\frac{\partial c_i}{\partial t} = -\nabla \cdot \mathbf{\Gamma}_i \tag{4}$$

The electrical potential distribution is governed by the Poisson equation:

$$\nabla \bullet (\varepsilon_r \nabla \phi) = -\frac{F \sum z_i c_i}{\varepsilon_0} \tag{5}$$

where ε_0 is the permittivity of vacuum and ε_r is the relative permittivity. The electric potential at the wall surface is governed by:

$$\frac{\partial \phi}{\partial n} = -\frac{\sigma_s}{\varepsilon_0 \varepsilon_r} \tag{6}$$

where is σ_s the surface charge density and n is the normal direction of the wall. The fluid flow is governed by the Navier-Stokes and continuity equations:

$$\rho\left(\frac{\partial \mathbf{u}}{\partial t} + \mathbf{u} \cdot \nabla \mathbf{u}\right) = -\nabla p + \mu \nabla^2 \mathbf{u} - \rho_e \nabla \phi \tag{7}$$

$$\nabla \cdot \mathbf{u} = 0 \tag{8}$$

where p is the hydrostatic pressure, μ is the fluid viscosity, and ρ_e is the space charge density. From solving the coupled Poisson-Nernst-Planck equations (PNP) and the Navier-Stokes equations, we can obtain the electric potential, ionic concentration, velocity, and pressure profiles in the nanopore. The current through the channel is calculated by integrating the ionic fluxes over the cross-sectional area of the channel (pore area extracted from TEM images), i.e.:

$$I = \int_S \sum_i z_i F \mathbf{\Gamma}_i \cdot \mathbf{n} dS \tag{9}$$

where S is the cross-sectional area of the pore. Figure 38b shows the conductance stability of these same pores as a function of time. Stable conductance values were obtained for over 60 minutes, confirming the stability of these pores in fluid. Conductance values after drilling a nanopore were several orders of magnitude higher than the conductance of a graphene-Al_2O_3 membrane with no pore.

6.3 Detection of dsDNA

To study the transport properties of graphene-Al_2O_3 nanopores, we performed experiments involving the translocation of λ-DNA, a 48.5 kbp long, dsDNA fragment extracted and purified from a plasmid. Given the relatively small persistence length of dsDNA (54 ± 2 nm)[196], λ-DNA is expected to assume the shape of a highly coiled ball in high salt solution with a radius of gyration, $R_g = \sqrt{2 l_p L} \approx 1.33$ μm as shown in figure 39a (i). Upon capture in the nanopore, the elongation and threading process occurs as shown in part (ii). Figure 39b illustrates the corresponding current blockades induced by λ-DNA as it translocates through an 11.3 nm diameter pore at an applied voltage of 400mV in 1M KCl, 10mM Tris, 1mM EDTA pH 10.4. The λ-DNA concentration used in these experiments was 100 ng/μl. High pH buffer was used to minimize electrostatic interactions between the bottom graphene surface of the nanopore and the negatively charged dsDNA molecule. Also, it is important to note that Al_2O_3 is negatively charged at this pH value (isoelectric point of Al_2O_3 is 8-9) and thus will not electrostatically bind

DNA as previously reported in chapter 4. Thus, these experimental conditions yielded repeatable DNA translocation through grahene-Al_2O_3 nanopores.

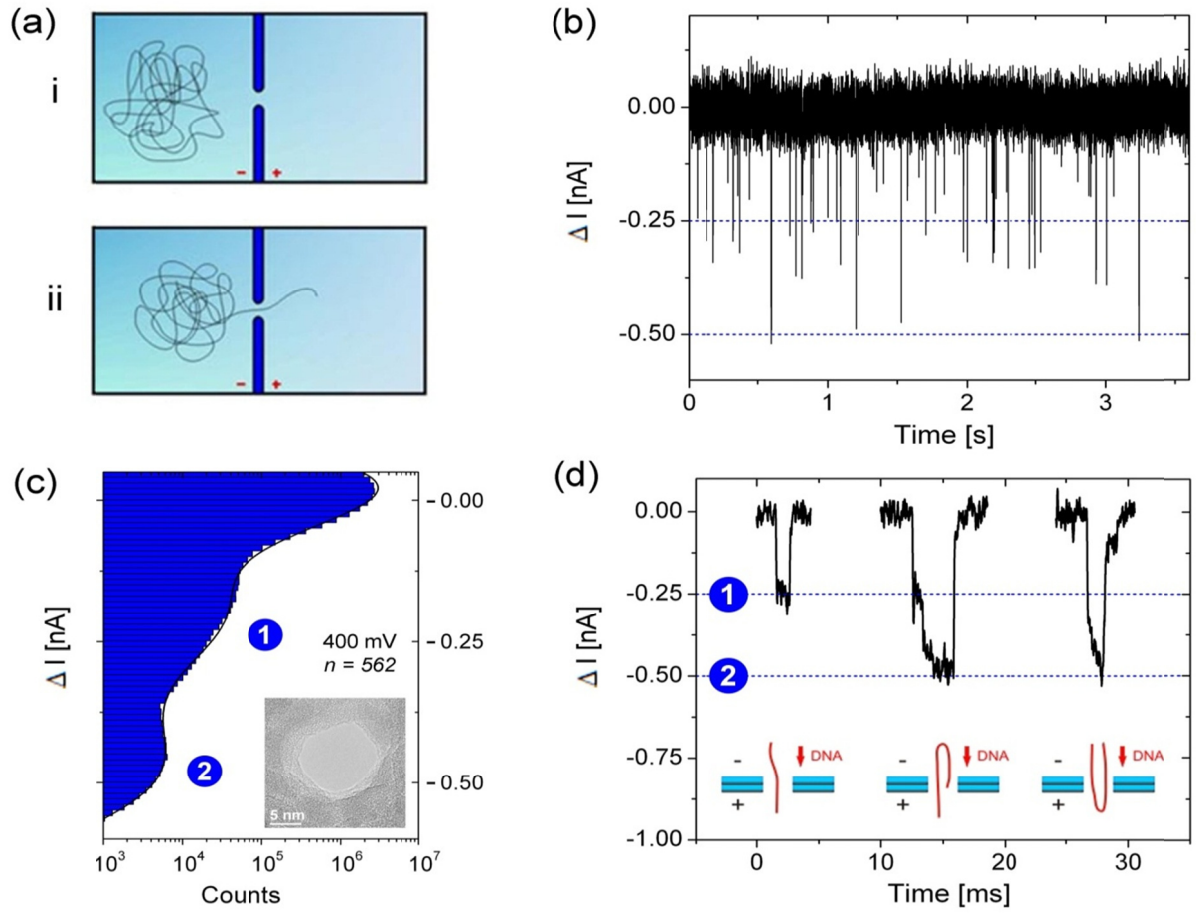

Figure 39 (a) Schematic showing transport of λ-DNA through a nanopore. λ-DNA has a radius of gyration of ~1.33μm and hence forms a large supercoiled ball in an electrolyte solution as shown. (ii) DNA threading process in a nanopore. (b) Characteristic translocation events of λ-DNA through a 11.3 nm graphene-Al_2O_3 nanopore. Clear downward blockades are observed. (c) Event current histogram constructed from 562 translocation events recorded at 400mV. Two distinct current peaks are observed; 1, representing linear dsDNA transport through the pore, and 2, representing folded DNA transport through the pore. This phenomenon is illustrated in more detail in (d).

Interestingly two distinct blockade levels were observed in λ-DNA translocation experiments, a shallow blockade corresponding to linear dsDNA transport, and a deeper blockade level corresponding to folded DNA transport as seen in figures 39b and the current blockage

histogram of 39c. Note that ΔI here represents the current blockage induced by dsDNA relative to the baseline current at a particular voltage (400 mV in this case). The current histogram of figure 39c was constructed from 562 individual DNA translocation events. The folded transport of λ-DNA through a nanopore comes as no surprise given prior literature demonstrating such a phenomenon in large 20 nm SiN and graphene nanopores.[26, 61]

To confirm that these events are indeed due to DNA translocation and not simply interactions with the pore surface, we probed the effect of voltage on translocation time. Voltage dependent DNA transport through an Al_2O_3 nanopore was previously demonstrated in chapter 4, translocation times decreasing with increasing voltage, corresponding to an increased electrophoretic driving force. A similar trend was observed in these experiments, $t_D = 1.81 \pm 2.77$ ms at 400 mV and $t_D = 2.66 \pm 4.08$ ms at 250 mV. The broad distribution of translocation times is again representative of translocations involving significant interactions with the pore surface.

The λ-DNA translocation experiments reported here are tremendously exciting as they prove that the graphene-Al_2O_3 nanopore is highly sensitive to detecting not only the presence of a single molecule, but also discriminating its subtle secondary structure (folded or unfolded). Indeed, this system could prove useful in reading the topographic structure of protein bound DNA fragments and or secondary structures that form in ssRNA. In the following section, we show proof-of-principle protein-DNA binding experiments involving estrogen receptor α to its cognate binding sequence.

6.4 Detection of Estrogen Receptor α and ERE Complexes

Estrogen receptor α (ERα) is a ligand-activated transcription factor that, upon binding a hormone, interacts with specific recognition sequences in DNA. This recognition sequence is referred to as an estrogen response element (ERE). Schematics of the binding process and the ERE sequence are shown in figures 40a and 40b respectively. DNA-bound ERα primarily serves as a nucleating factor for the recruitment of protein complexes and is involved in key biological processes including the oxidative stress response, DNA repair, and transcription regulation.[197]

ERα is a 599 amino acid long, 66.9 kDa protein with an isoelectric point of 8.3. Given all of our experiments were done at pH 8, we expect ERα to be positively charged under these experimental conditions. The ERα/ERE binding assay was performed in 80 mM KCl, 15 mM Tris, 0.2 mM EDTA, pH 8 containing 40% glycerol. The concentration of the dsDNA 50-mer containing the ERE sequence was 6.5 μg/ml; the final amount of the ERα protein added to the mixture was between 5-10 fmoles.

The binding of ERα to its ERE sequence was confirmed using gel shift assays as shown in figure 40c. Binding was only observed at low salt concentrations below 640 mM as shown by the protein-DNA band, with binding efficiency decreasing with increasing KCl concentration. As a result, all nanopore sensing experiments with the ERα/ERE complex were performed in 80 mM KCl to maintain the integrity of the complex. Figure 40d shows the transport of the complex through a 14.3 nm graphene-Al_2O_3 pore. Clear current amplification events were observed as the complex transited through the pore (illustrated as upward pulses rather than the customary downward pulses that are typically observed in nanopore experiments). Current amplification induced by DNA transport through large 15-20 nm nanopores had previously been reported by Smeets and Chang at low salt concentrations (≤ 100 mM).[73, 96] These amplifications were reported to be the result of counterion (K+) condensation on the DNA backbone which locally enhanced the conductance of the nanopore during DNA translocation events in low salt. This phenomenon may explain the results observed in our experiments as well. K+ condensation on the 50-mer probe sequence and Cl- condensation on the net positively charged ERα may cause such upward events. Interestingly, the durations of the events observed here are significantly longer than dsDNA events relating to very-long λ-DNA fragments. Thus, these events could not be attributed to the 50-mer sequence alone. These studies confirm that a DNA-protein complex can indeed be detected using a solid-state nanopore.

The detection of ERα/ERE also serves as a model system and these principles can be extended to the detection of a variety of other DNA-protein complexes with very useful diagnostic applications. One such protein-DNA system will be presented in the next chapter.

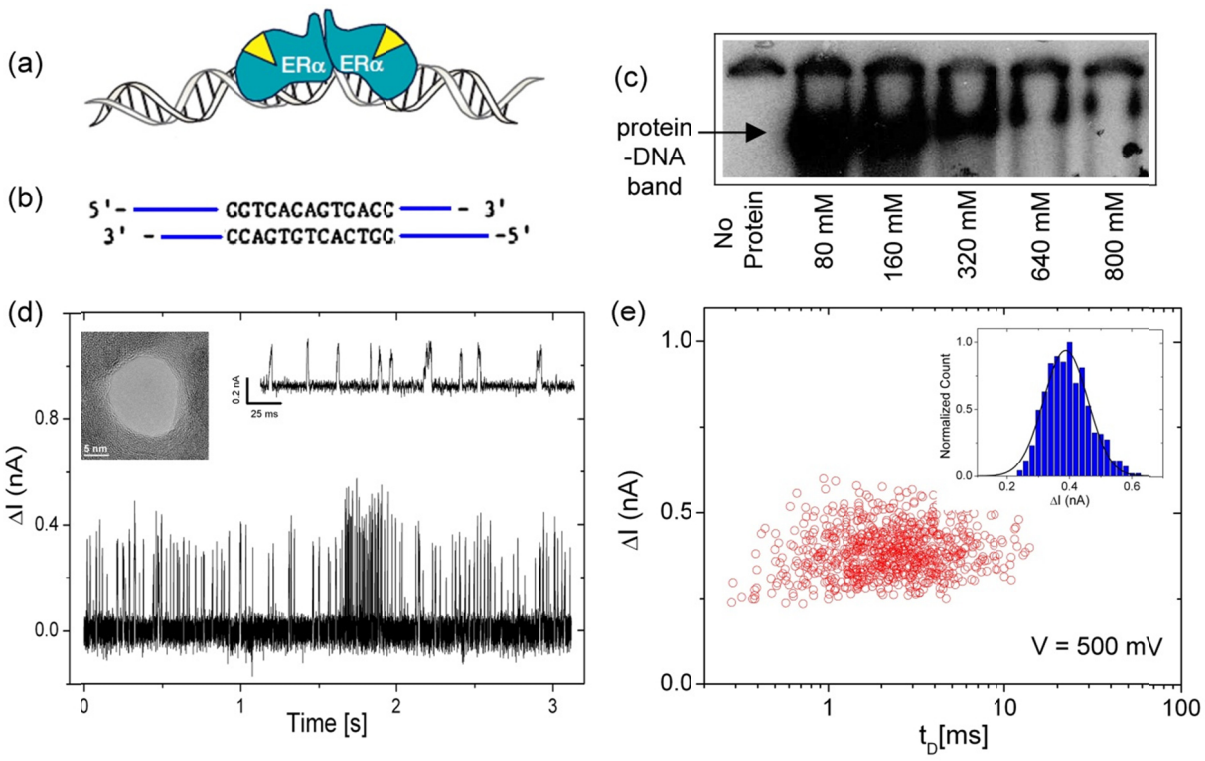

Figure 40 (a) Schematic showing the binding of ERα to dsDNA. (b) The binding sequence of ERα known as the estrogen response element (ERE). (c) Gel shift assay showing the formation of the ER/ERE complex exclusively at low KCl concentrations. High KCl concentrations ≥ 640 mM prevented the formation of the complex. (d) The transport of ER/ERE complex through a 14.3 nm pore in 80 mM KCl, pH 8. Distinct upward events were observed at 500 mV as shown. (e) Current enhancement (ΔI) vs. translocation time (t_D) histogram for the ER/ERE complex at 500 mV. Mean t_D = 3.2 ms. (Inset) ΔI histogram shows a Gaussian distribution centered at ΔI = 0.39 nA.

The voltage dependent transport of the complex is illustrated in figure 41a and voltage dependent translocation times are shown in figure 41b.

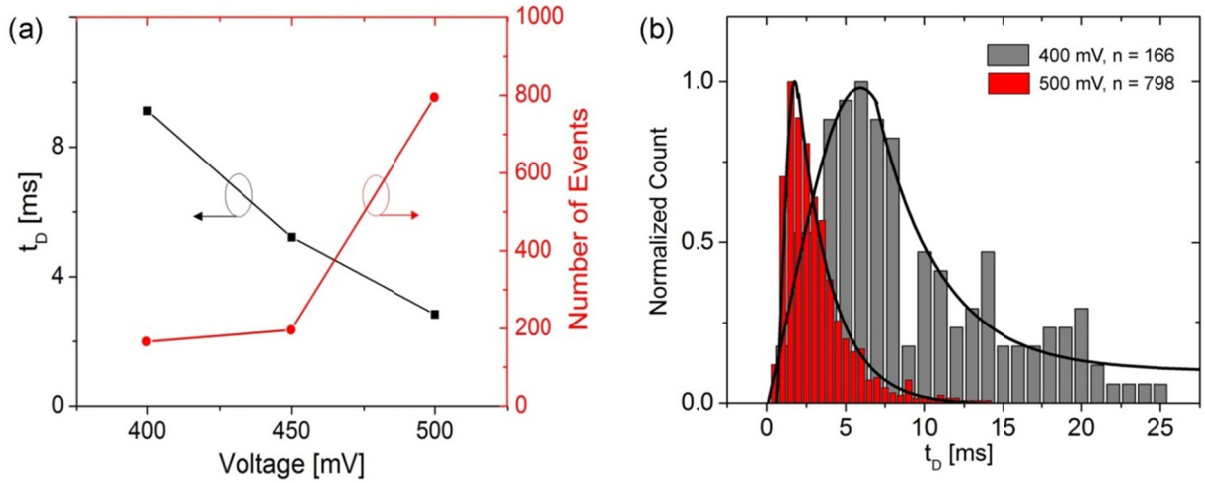

Figure 41 (a) Voltage dependent transport of ERα/ERE complex through a 14.3 nm graphene-Al_2O_3 nanopore. Event flux increased with increasing voltage, and translocation time (t_D) decreased with increasing voltage. (b) Translocation time histogram at 400mV and 500mV applied biases. Peaks corresponding to the most probable translocation time of the ERα/ERE complex are located at 6 ms and 1.6 ms respectively.

6.5 pH Dependent Response of Graphene-Al_2O_3 Nanopores

Because of the high surface-to-volume ratio in nanopores, surfaces potentially have a very large effect on pore conductance at low salt concentrations. Here we discuss the surface charge characteristics and pH response of graphene-Al_2O_3 nanopores. At high salt concentrations, charge carriers in the solution dominate the ionic current through the pore. The conductance scales linearly with the number of charge carriers, as observed experimentally, and surface charge has negligible effect. At low KCl concentrations, however, the total current through the nanopore is a combination of the contributions of the bulk concentration of ions in solution and the counterions shielding the surface charge (electroosmotic flow). Above the isoelectric point of Al_2O_3 (~pH 8-9), the surface charge in the pore is negative resulting in a double layer of condensed K ions, and below the isoelectric point, the surface charge is positive resulting in a double layer of condensed Cl counterions as shown in figure 42a.

Pore conductance, *G*, can therefore be written as:

$$G_{pore} = \frac{\pi}{4}\frac{{d_{pore}}^2}{L_{pore}}\left[(\mu_K + \mu_{Cl})n_{KCl}e + \mu_K \frac{4|\sigma|}{d_{pore}}\right] \quad (10)$$

where d_{pore} represents the diameter, L_{pore} is the length of a cylindrical nanopore, n_{KCl} is the number density of potassium or chloride ions, e is the elementary charge, σ is the surface charge density in the nanopore, and μ_K and μ_{Cl} are the electrophoretic mobilities of potassium and chloride ions, respectively. We use values of μ_K = 7.616 x 10^{-8} m^2/Vs and μ_{Cl} = 7.909 x 10^{-8} m^2/Vs. The first term in the equation 9 represents the bulk conductance, and the surface charge contribution to the conductance in the nanopore is given by the second term. At KCl concentrations higher than $n_{KCl} >> 2\sigma/d_{\text{pore}}e$, the first term in the formula dominates the conductance and bulk behavior is observed. Deviations from bulk behavior start to occur when the first and the second terms in equation 9 are comparable. As n_{KCl} is lowered further, surface effects govern the nanopore conductance. The above model assumes constant surface charge. However, our results suggest that surface charge may in fact also depend on ion concentration. This follows from the chemical reactivity of the Al_2O_3 surface given by:

$$AlOH \leftrightarrow AlO^- + H^+ \quad (11)$$

Assuming thermodynamic equilibrium, the concentration of H^+ ions near the surface is set by the local electrostatic potential. Behrends and Grier derived a relationship between the potential at the no-slip plane (ζ potential) and the surface charge density, σ, taking into account surface reactivity:

$$\zeta(\sigma) = \frac{k_B T}{e}\ln\left(\frac{-\sigma}{e\Gamma+\sigma}\right) + \frac{k_B T \ln(10)}{e}(pK - pH) - \frac{\sigma}{C} \quad (12)$$

where k_BT represents the thermal energy, Γ is the surface density of chargeable sites, pK is the equilibrium constant, and C is the capacitance of the Stern layer. An additional relationship between Γ and σ is given by the Grahame equation, which couples the electrostatic potential and the charge in the diffusion layer:

$$\sigma(\zeta) = \frac{2\varepsilon\varepsilon_o k_B T\kappa}{e} sinh\left(\frac{e\zeta}{2k_B T}\right) \quad (13)$$

where $\varepsilon\varepsilon_o$ denotes the permittivity of the solution and κ^{-1} is the Debye screening length. Combining equations 11 and 12 yields the surface charge as a function of the potassium chloride concentration. The varying surface charge obtained can be substituted into equation 9 to determine the salt-dependent conductance of the nanopore.

Pore conductance as a function of KCl concentration and pH is shown in figures 42b and 42c respectively for 18 ± 1 nm diameter and 8 ± 0.5 nm diameter graphene-Al_2O_3 nanopores.

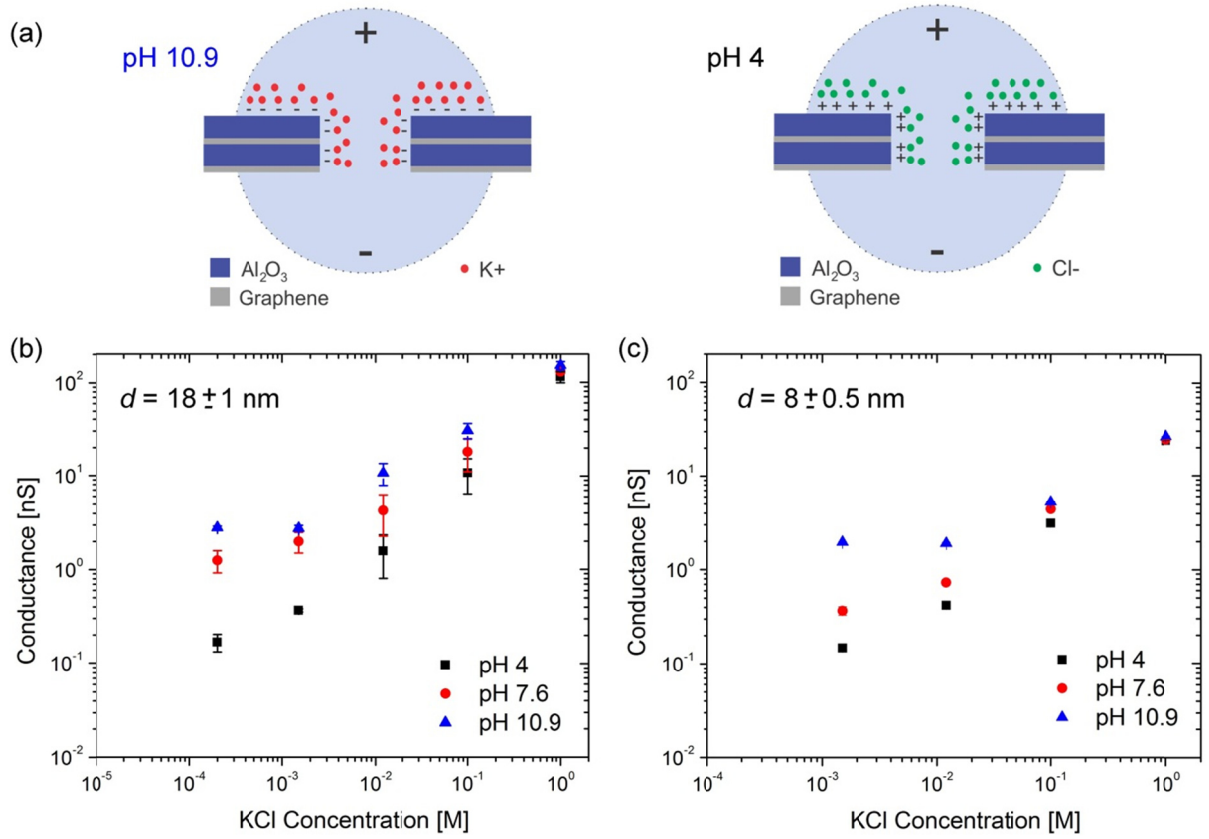

Figure 42 (a) Schematics showing counterion condensation on the pore surface at both high pH and low pH assuming an isoelectric point of the nanopore is in the pH range of 5-7. (b) pH response of a 18 ± 1nm diameter graphene-Al_2O_3 pore as a function of KCl concentration and solution pH. (c) The effect of pore size: pH response of a 8 ± 0.5 nm diameter graphene-Al_2O_3 pore as a function of KCl concentration and solution pH.

Conductance saturation was clearly observed at pH 10.9 as salt concentration was reduced, suggesting the presence of a highly charged, negative pore surface under these high pH conditions. In contrast, conductance saturation was not observed at pH 4 even at very low KCl concentrations (figure 42b), suggesting that the pore is only weakly charged at this pH. The pH 4 response more closely resembles bulk behavior where the effects of surface charge on channel conductance are minimal (i.e. second term in equation 9 is almost negligible). These results suggest that the isoelectric point of a graphene-Al_2O_3 nanopore is close to pH 4, where the pore surface exhibits near negligible surface charge. This is surprising as planar Al_2O_3 surfaces deposited by ALD exhibit an isoelectric point of 8-9. The deviation from this bulk behavior may be attributed to multiple factors. Firstly, TEM fabrication dramatically changes the local composition of the nanopore relative to the bulk material. This was observed in chapter 4 via the preferential sputtering of O in Al_2O_3 during TEM pore formation. The result was an Al rich nanopore surface, closer to $AlO_{0.6}$ in composition versus Al_2O_3 in the bulk. Secondly, TEM pore formation in nanolaminates is known to cause material mixing. For example, the formation of nanopores in SiO_2/SiN/SiO_2 stacks showed that O atoms can be dragged by a 200keV electron beam from the SiO_2 layer into the SiN layer. Such liquid-like behavior in turn leads to mixing of O and N over the electron irradiated volume.[78, 116] Note that Si rich particles were also observed in the pore vicinity in SiO_2/SiN/SiO_2 systems, attributed to the preferential sputtering of O and N. It is therefore plausible that the material composition of our graphene-Al_2O_3 nanopore is a combination of C, Al, and O fused together. The pH response, isoelectric point and surface charge density of this melded material system will likely deviate significantly from bulk ALD Al_2O_3 or pure graphene response due to changes in bond lengths, co-ordinations and material composition in the sputtered system.

Another contributing factor to the pH response observed in these experiments may have to do with the exposed graphene sheet on the bottom side of the nanopore. Previous studies have shown that the electrochemical double layer at the graphene/electrolyte interface is very sensitive to solution pH in both graphene FETs (GFETs) and multi-walled CNTs.[198-200] In fact, higher carrier mobilities and a shift in the Dirac point to more positive potentials are typically observed with increasing pH, which is indicative of increasing *p*-doping of the graphene sheet by the

adsorption of OH- ions. Studies have also shown that the application of negative gate potentials in GFETs (resulting in accumulation of OH- ions at the surface) produces a larger increase in conductivity when compared to positive gate potentials (accumulation of H_3O+). Measured threshold voltage shifts with pH at negative gate biases yielded a value of 98 mV/pH unit for 1-2 layers of graphene and 99 mV/pH for 3-4 layers of graphene at constant V_{ds} of -1 V.[198] Both values are higher than the theoretical maximum predicted by the Nernst limit (59.2 mV/pH unit). This supra-Nernstian pH sensitivity was observed only at negative gate voltages, suggesting that the mechanism of pH sensitivity may involve an interplay between surface potential modulation by ion adsorption and the attachment of amphoteric OH- groups. The attachment of OH- groups was also observed in MWCNTs, thereby disrupting the local sp^2 hybridization at exclusively high pH and resulting in an increase in conductance.[199] This pH dependent surface charge on the graphene layer could affect nanopore conductance.

Figure 42c illustrates the pH response of a smaller 8 ± 0.5 nm diameter pore. Similar trends are seen as in figure 42b with lower pore conductance being observed at lower pH. Interestingly, saturation/plateauing in the conductance at pH 10.9 were observed at KCl concentrations starting at 10 mM, an order of magnitude higher than in figure 42b. This result is expected as Debye layer overlap and surface effects will begin to dominate at higher salt concentrations in smaller pores. The Debye screening length given by κ^{-1} (where $\kappa^2 = 2e^2 n_{KCl}/k_B T \varepsilon \varepsilon_o$) is approximately 3 nm in 10 mM KCl and thus is comparable to the 8 nm diameter of the pore in figure 42c. Thus surface charge effects are expected to be significant at this relatively high salt concentration.

The pH response of graphene-Al_2O_3 nanopores is significantly more pronounced than the pH response of SiN[84] and TiO_2[82] nanopores as well as SiO_2 nanochannels.[201] This may in part be due to the presence of graphene as discussed earlier, in conjunction with the high surface charge density of Al_2O_3. Numerical simulations and fitting of the analytical equations 9-12 should enable the extraction of this charge density (currently under way) and should allow for quantitative comparison with SiN and TiO_2 nanopore platforms.

These studies confirm that modulating the surface potential of the nanopore using solution pH can indeed modulate the conductance of the pore. Next we investigate the effect of modulating nanopore surface potential using a gate electrode.

6.6 Graphene Gated Nanopores

The concept of an electrically gated solid-state nanopore has been widely discussed, but the implementation of such a system has proven challenging. A third electrode embedded in the nanopore is particularly attractive as it can be used to modify the electric fields in the pore and could potentially act to slow down or capture a translocating DNA molecule, a key step in enabling nanopore sequencing. The effects of an insulated third electrode on the conductances of both nanochannels and nanopores were previously shown.[82, 202] In the referenced nanopore study, however, the third electrode was a 30 nm thick TiN layer. Here we discuss the possibility of using graphene, of thickness only a few monolayers, as a nanopore electrode. The realization of such a structure involved simple modifications to the architecture shown in figure 37. These modifications include the contact of graphene layer 2 (g2) in figure 37 with a 250 nm evaporated Ti/Au pad prior to atomic layer deposition of dielectric 2 (d2), as shown in figure 43a. The nanopore is next drilled in the contacted stack. After drilling the pore, the nanopore chip is epoxied (Kwikcast from World Precision Instruments) to a custom designed PCB and the Ti/Au pads contacting the graphene gate are connected using indium wires to external PCB pads (1 and 2) as shown in figure 43b. The resistance across pads 1 and 2 after connecting the chip was in the range of 5-15 kΩ typically, confirming the presence of a conductive graphene sheet on the nanopore chip after fabrication. The PCB mounted nanopore chip was next inserted into a custom designed fluidic setup as shown in figure 43c. Care was taken to ensure that the Ti/Au pads were isolated from the fluid to prevent leakage currents.

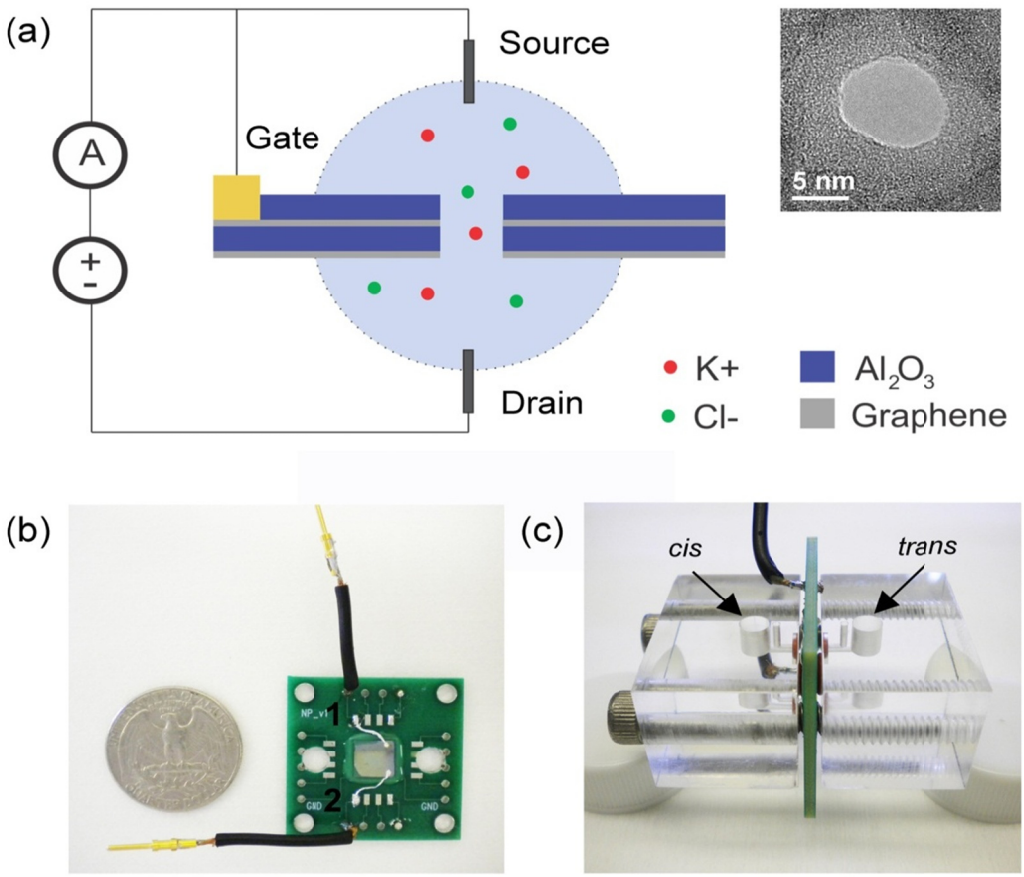

Figure 43 (a) Graphene gated nanopore measurement setup. Graphene layer 2 (g2) is contacted using a 250 nm Ti/Au pad at the edge of the nanopore chip. Gate and source are tied together in all current measurements. (b) Nanopore chip is mounted on a PCB and the Ti/Au pads are contacted using In wires. The resistance across terminals 1 and 2 is typically ≤ 15 kΩ confirming the presence of a conducting graphene sheet after fabrication. (c) PCB with a nanopore chip is mounted in a fluidic setup as shown, which isolates the metal contact pads from the conductive solution.

Nanopore measurements with the graphene gate were conducted by tying the gate node to the source electrode, as shown in the schematic of figure 43a. The source and gate were tied to prevent leakage currents from flowing between the source and gate nodes. Even though graphene technically should act as a non-Faradaic electrode with very little electron exchange occurring in an ionic solution under low applied biases, the presence of defects and grain boundaries, characteristic of CVD grown graphene, likely give rise to such a leakage current. These currents are non-negligible but are understandable given the fluid contact area on the nanopore chip is

~19.6 mm^2 with an insulating layer of Al_2O_3 that is only 7-8 nm thick. To check the magnitude of this leakage current, independent leakage current measurements were conducted using Al_2O_3 coated graphene sheets on planar SiO_2 surfaces. A schematic of the setup is shown in figure 44a and the corresponding leakage current is shown in figure 44b.

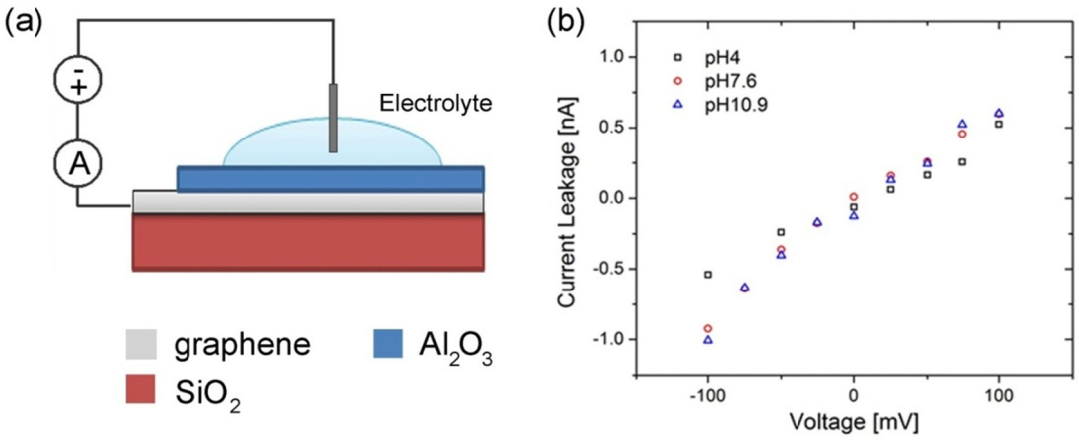

Figure 44 (a) Current leakage measurement setup: CVD graphene is first transferred to a glass slide. Next, 2 nm of Al is evaporated on the graphene as an adhesion layer followed by the deposition of a 6.5 nm Al_2O_3 insulating layer via ALD. Leakage current is measured by applying a potential across the graphene and a Ag/AgCl reference electrode immersed in a 1M KCl, 10mM Tris, 1mM EDTA electrolyte solution of varying pH. Note that the fluid contact area is 19.6 mm^2 in these experiments, the same as in nanopore measurements. Leakage currents at pH values of 4, 7.6 and 10.9 are shown in (b).

The electrolyte solutions used in these experiments were 1M KCl, 10 mM Tris, 1mM EDTA of varying pH. The fluidic contact area was kept consistent with the contact area on the nanopore chip (~19.6 mm^2). The electrolyte was insulated from the graphene by only 2 nm of evaporated Al which oxidizes followed by 68 cycles ALD Al_2O_3 (~ 6.5 nm), also consistent with our nanopore chips. Leakage currents showed weak pH dependence and were less than 1 nA in magnitude in this high salt environment for all voltages probed. Applied voltages across the gate-source were ≤ 100 mV corresponding to an electric field of 0.15 MV/cm, well below the critical breakdown field of Al_2O_3 (4-5 MV/cm). This leakage current could be further reduced by decreasing the fluid contact area, operating in a lower salt environment or by coating the surface

with another ALD material such as HfO_2 to form an Al_2O_3 /HfO_2 nanolaminate. Figure 45 illustrates the effect of connecting the graphene gate (tied gate-source) in graphene-Al_2O_3 nanopores versus leaving the gate floating, under a variety of salt conditions and pH values.

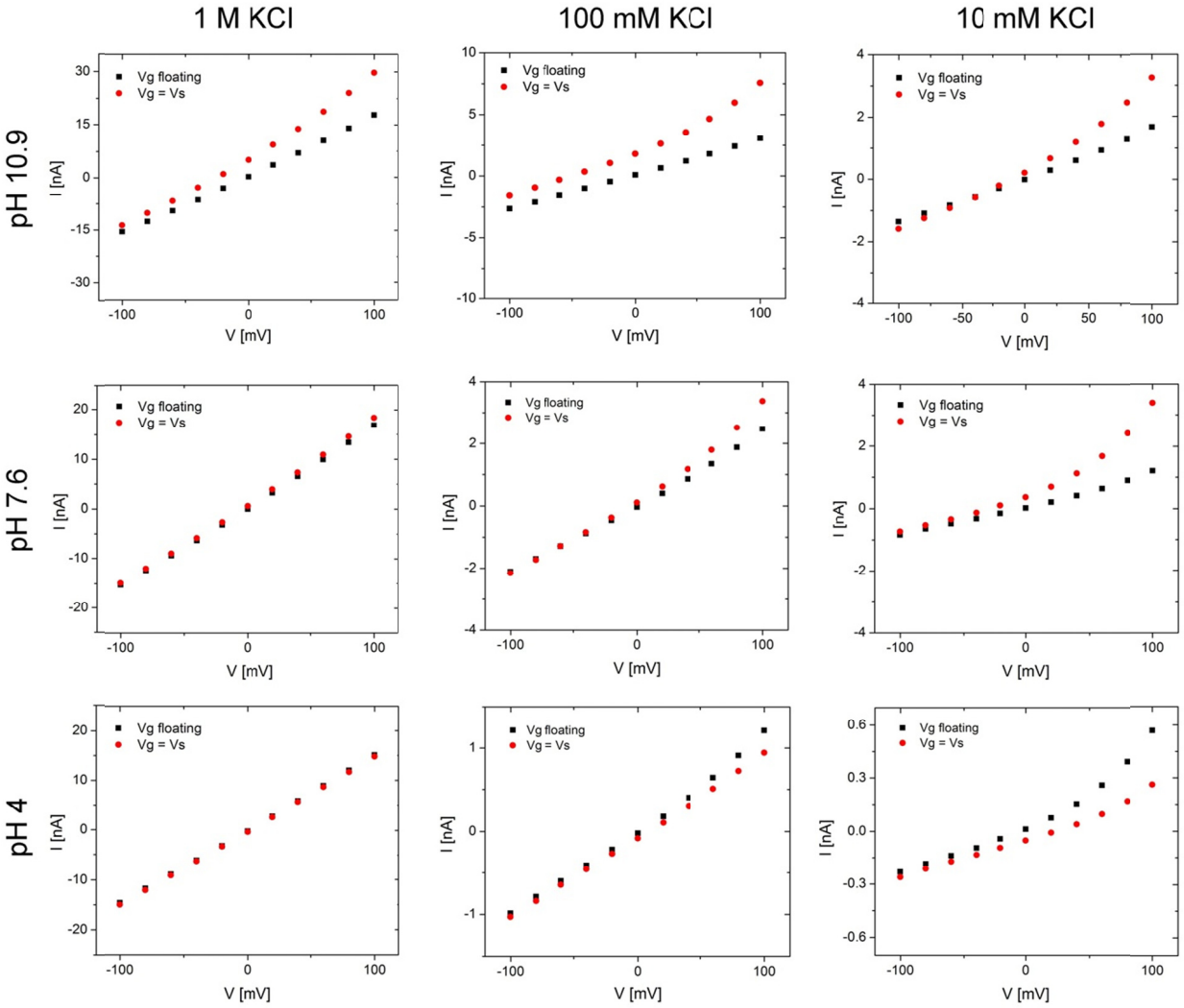

Figure 45 Current-voltage (I-V) characteristics of a 19 nm diameter graphene-Al_2O_3 nanopore with gate (graphene layer 2) tied to the source and the gate left floating. The three rows represent I-V measurements taken at fixed pH values of 10.9, 7.6 and 4 and the three columns represent I-V measurements taken at fixed KCl concentrations of 1 M, 100 mM and 10 mM. Significant current rectification was observed at pH 10.9 at all salt concentrations probed. This effect was dramatically reduced at pH 4.

A higher conductance level is seen at pH 10.9 and pH 7.6 with the gate connected relative to the floating case. In contrast, lower conductance is observed at pH 4 with the gate connected relative to the floating gate case. Though this current enhancement and reduction is more pronounced as the salt concentration is reduced suggesting an electrostatic effect, this result cannot be attributed solely to an electrostatic modulation of the field in the pore. It is likely that there are also electrochemical currents flowing through the contacted g2 layer, which are more pronounced at higher pH. This potentially explains the significant current amplification observed at 1M KCl, pH 10.9 conditions even though the Debye screening length at this concentration is only ~ 0.3 nm. This is consistent with the notion that at high pH, OH- can disrupt the sp^2 bonding of graphene resulting in charge transfer at the graphene fluid interface. This effect does not occur at low pH values, consistent with the lack of current enhancement observed in our experiments. The current modulation through the pore with the gate connected also cannot be attributed solely to leakage currents. Figure 44 shows little variation in leakage current as a function of pH in the voltage range (-100 mV to 100 mV), identical to what was probed in gated nanopore measurements. Further experiments are needed to understand the exact mechanism governing the gate response, but initial results show significant promise. Our results also suggest that the g2 layer may in fact be used as a *trans* electrode in the pore given the significant current transfer that is observed at this interface. This layer could serve as a sensitive electrode in future DNA translocation experiments. The application of local potentials in the pore via this third electrode may also be useful in slowing or trapping DNA molecules in the pore. The viability of these concepts needs to be explored through further experiments.

6.7 HfO_2 Coated Nanopores

Coating graphene-Al_2O_3 nanopores with an ALD HfO_2 layer could not only help passivate the surface of the nanopore and help reduce leakage currents, but could also alter pH response as the isoelectric point of HfO_2 is 7[203] and allow for surface functionalization with organosilanes. ALD HFO_2 deposition in a preformed nanopore, however, is not trivial. Given the high surface area, confined volume, high defect density/surface roughness and varying material composition in a nanopore, the deposition follows a highly nonlinear process and resembles a chemical vapor

deposition process as opposed to a self-limiting ALD process. Figure 46 shows HfO_2 deposition rates are 3-4 times faster in a nanopore than on planar hydroxylated Si surfaces.

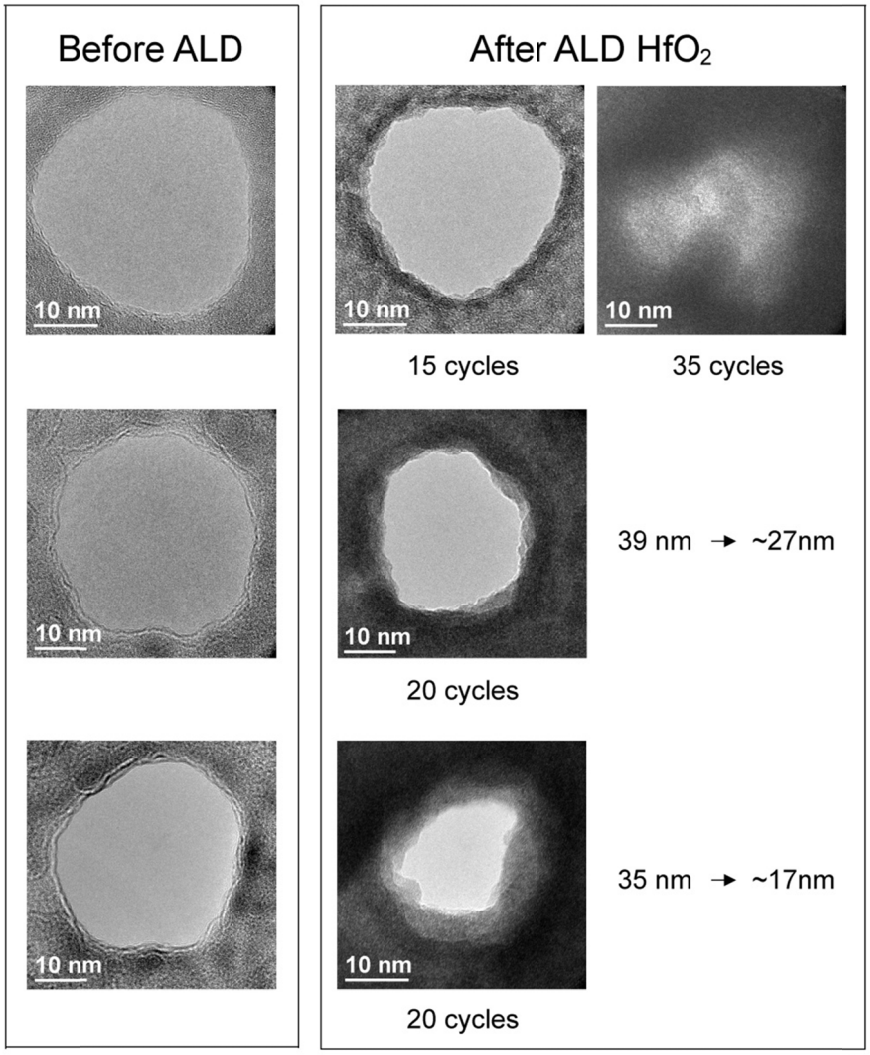

Figure 46 (Left Column) TEM phase contrast images of nanopores formed in graphene-Al_2O_3 stacks prior to ALD HfO_2 deposition. (Right Column) Following ALD HfO_2 deposition in the pore. HfO_2 deposition rate is ~1.3 Å on planar surfaces at 120ºC using this deposition recipe, however, the deposition rate in a nanopore is significantly faster and is non-linear. We approximate a deposition rate of between 3 and 4.5Å/cycle inside the pore for the first 20 cycles. This rate increases with the number of cycles.

This non-linear deposition may be due to several factors. The surface of the nanopore post e-beam fabrication may not be completely hydrophilic and may also contain defect sites and exposed graphene edges that serve as nucleation sites. ALD deposition on H terminated Si surfaces is known to be problematic. The lack of uniform nucleation on H-Si can produce island growth as described by a Volmer-Weber growth mechanism.[204] After multiple ALD cycles, these islands may grow together and form a continuous film. However, in the ultrathin film regime, the ALD films are rough and not conformal to the initial substrate. Nucleation difficulties are also encountered during atomic layer deposition of Al_2O_3 and HFO_2 on carbon nanotubes and graphene. This is typically because CNT/graphene surfaces are inert and do not contain chemical species (OH groups) that allow for the reaction of either $Al(CH_3)_3$ or H_2O during deposition. As a result, Al_2O_3 ALD on single-walled and multi-walled CNTs yields only the growth of isolated Al_2O_3 nanospheres originating from specific defect sites on the surface of the CNTs. Similarly, Al_2O_3 and HfO_2 ALD have resulted in the growth of nanoribbons only along the step edges of graphene surfaces.[204] These issues likely complicate the deposition of a highly conformal HfO_2 coating inside the nanopore.

Despite these challenges, we were able to form HfO_2 coatings inside the pore by limiting the total number of ALD cycles to ≤ 20. The pH response of these HfO_2 coated pores was also examined and is shown in figure 47. Surprisingly pore conductance at high pH (10.4) did not saturate, suggesting that the density of exposed –OH groups on the HfO_2 coated surface is significantly less than in Al_2O_3 case. This does not come as a surprise given the pH response of HfO_2 is only 49 mV/pH unit, relative to the near Nernst like response of thin Al_2O_3 layers (59 mV/pH unit).[205] Figure 47 also suggests that the isoelectric point of HfO_2 is between 4 and 7.6 given the close to bulk-like conductance behavior observed at these pHs.

DNA translocation through HfO_2 coated nanopores was also observed. Though events were sparsely populated, characteristic downward blockades were observed in 1M KCl, 10 mM Tris, 1 mM EDTA, pH 10.4. Further experiments need to be conducted to determine the translocation dynamics of λ-DNA through a HfO_2 nanopore.

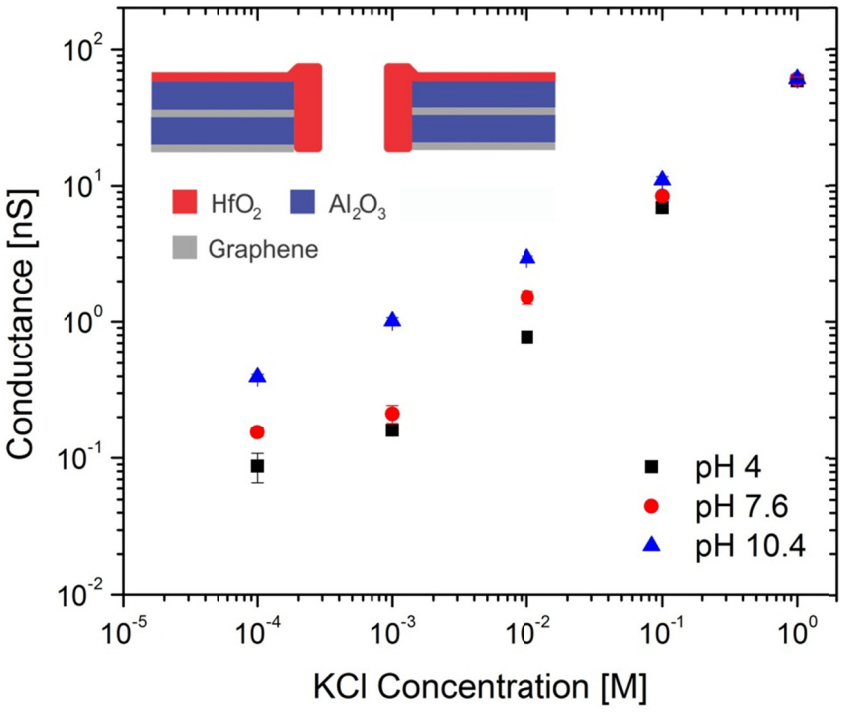

Figure 47 pH response of an 18 nm diameter HfO_2 coated nanopore. Conductance saturation is not observed at any of the pH values tested with minimum conductance obtained between pH 4 and 7.6. These results suggest that the isoelectric point of a HfO_2 pore is likely between 4 and 7.6. Also note that at high pH (10.4), the conductance does not saturate, suggesting that the surface charge density is significantly less in magnitude than in graphene-Al_2O_3 nanopores.

6.8 Chapter Summary

This chapter summarized the development of a novel, highly versatile graphene-Al_2O_3 nanopore platform for biomolecule sensing. These nanopores are highly robust, exhibit stable conductance values, show remarkable pH response and allow for the manipulation of ionic current through the nanopore by applying potentials to the graphene gate. Future studies will reveal whether the graphene gate could help slow down or trap a translocating DNA molecule in the pore, an exciting prospect that could help enable nanopore based DNA sequencing. This novel platform could also be useful in medical diagnostics as presented in the next chapter.

Future Work 7

We propose using the graphene-Al_2O_3 nanopore sensors discussed in chapter 6 for the detection of robust cancer biomarkers (specifically DNA methylation patterns) at ultra-low concentrations in human serum samples. Nanopore technology is well suited for gene based methylation analysis and is capable of screening small panels of hypermethylation markers specific to a variety of cancers. Nanopore sensors, therefore, could potentially play an important role in early cancer detection, risk assessment, disease monitoring, chemoprediction and patient prognosis.

The majority of methylation detection techniques conduct analysis at specific loci or groups of genes where CpG hypermethylation is known to correlate with cancer. Standard analytical techniques such as PCR, however, erase methylation information leaving the investigator oblivious to the epigenetic content of the original genomic DNA sequence. To overcome such limitations, new clinical techniques have been developed and are summarized below. The sequence of steps associated with each technique is illustrated in figure 48.

7.1 Conventional Methylation Detection Assays

Bisulfite Genomic Sequencing (BGS): The gold standard in DNA methylation analysis is bisulfite genomic sequencing which involves (1) sodium bisulfite conversion of DNA, (2) PCR of the target fragment, and (3) DNA sequencing.[206] Sodium bisulfite efficiently converts cytosine to uracil (C→U) without affecting 5-methylcytosine (5mC→5mC) and is used to preserve epigenetic information during PCR. Methylation status is derived by sequencing the bisulfite converted, PCR amplified, target sequence using Sanger bisulfite sequencing or pyrosequencing methods.[207] Although the bisulfite conversion process is a powerful method for the identification of 5-methylcytosine, it presents some major drawbacks. During conversion, DNA is exposed to a tremendously harsh environment resulting in significant DNA degradation (approaching 85% to 95% after 4 hours at 55 °C).[208] As a result, relatively large amounts of

human genomic DNA are required prior to bisulfite treatment to ensure enough template DNA is available for PCR. This requirement cannot always be met in clinical settings as methylated DNA shed by tumor cells in serum is usually only available at relatively low concentrations.

Additional drawbacks include the relatively low PCR amplification efficiency of bisulfite converted DNA relative to normal genomic DNA [209] and the instability of bisulfite converted DNA during long-term storage. The combination of bisulfite DNA conversion, PCR and DNA sequencing processes makes BGS a labor intensive, time consuming and expensive technique that is not readily extensible to high-throughput DNA analysis.[207]

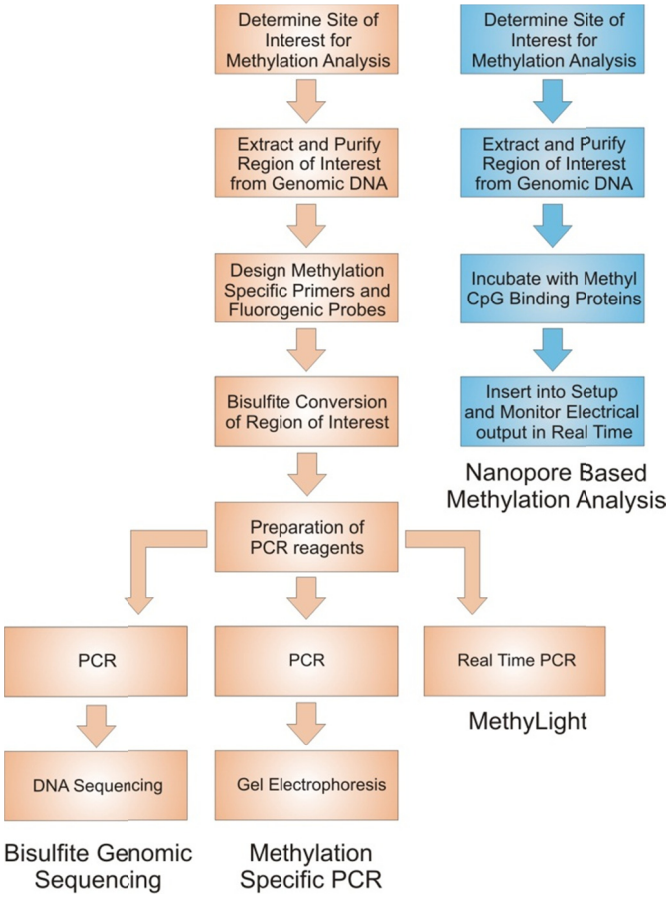

Figure 48 Sequence of steps associated with conventional methylation detection techniques such as BGS, MSP and MethyLight (Orange). Sequence of steps associated with nanopore based methylation analysis (Blue).

Methylation-Specific PCR (MSP): Methylation-specific PCR overcomes the need for sequencing. This process also relies on the initial bisulfite conversion of DNA, but in contrast to the bisulfite genomic sequencing technique, methylation discrimination is achieved at the PCR stage itself. In MSP, different primer sets covering CpG dinucleotides are designed for the methylated and unmethylated versions of the region of interest. The two amplification reactions are run in parallel, and qualitative conclusions regarding the methylation status of the original sequence are drawn from the presence or absence of a resulting PCR product in the two reactions.[209] This technique again requires complex primer design, PCR reagent preparation steps, PCR and manual gel-electrophoresis, making it both time intensive and laborious.[209]

MethyLight: The MethyLight assay combines the strengths of MSP with quantitative, fluorescence-based, real-time PCR for improved sensitivity and throughput.[210, 211] Again bisulfite treatment is required prior to PCR. MethyLight incorporates a methylation-specific FRET probe that binds selectively to the template strand and allows for accurate quantification of MSP reactions and enhanced methylation detection.[209] Though this technique is faster than MSP, a drawback of the MethyLight implementation is that it is limited to detecting only specific, predicted methylation patterns, resulting in low throughput.[209] To detect methylation in a target sequence containing two CpG dinucleotides, 4 separate reactions or 4 differently labeled probes would be needed, adding complexity and cost. In addition, the MethyLight assay suffers from PCR related artifacts and plate-to-plate variations.[209]

Large Scale Methylation Analysis Methods: Techniques also exist for large scale genome wide methylation analysis. Two such methods include restriction landmark genomic scanning (RLGS) and DNA microarrays. A detailed description of these techniques is available in the literature.[212-214] Applications of RLGS include determining global methylation changes in chronic lymphocytic leukemia and studying the effects of genome wide hypomethylation.[213] Microarray techniques have been used to detect methylation aberrations associated with a variety of cancers, including breast cancer.[214] Though these techniques allow for genome-wide analysis in a highly parallelized manner, they still require bisulfite treatment or methylation-sensitive

restriction enzyme digestion prior to screening. In addition, large sample volumes and significant downstream analysis are needed, especially in the case of RLGS.[213] Low resolution and cross hybridization in microarray analysis[213] also limit the utility of this approach.

7.2 Nanopore Based Methylation Analysis

Current methods for gene based methylation analysis are highly labor intensive, require large sample volumes, suffer from high per run cost and in most cases lack the sensitivity needed to derive useful clinical outcomes. In contrast, a nanopore based approach to methylation analysis for early cancer detection, though a radical departure from current clinical paradigms, may deliver the sensitivity and speed needed in extracting useful clinical information, relevant to patient outcome. Nanopore based techniques are well suited for gene based methylation analysis due to their ability to (1) detect target molecules at extremely low concentrations from minute sample volumes, (2) detect a combination of methylation aberrations across a variety of genes (important in monitoring disease progression and prognosis), (3) detect subtle variations in methylation patterns across alleles that would not be detected using bulk ensemble averaging methods such as PCR and gel-electrophoresis, (4) perform rapid methylation analysis (hundreds of copies of the same gene analyzed in minutes), (5) reduce cost (small reagent volumes needed), (6) simplify experimental and analysis steps by eliminating cumbersome PCR, DNA sequencing and bisulfite conversion steps as shown in figure 29.

Analysis of MBD2 bound Methylated DNA using Electrical Current Spectroscopy

The nanopore based methylation analysis process is illustrated in figure 49. First, commercially available, fully methylated, short (~100-200 bp) control DNA molecules (collaboration with Mayo clinic) will be combined with methyl-CpG binding proteins to form protein bound DNA complexes (figures 49b and 49c). The methyl-CpG-binding protein family consists of five proteins, MeCP2, MBD1, MBD2, MBD3 and MBD4, each containing a methyl-CpG-binding domain (MBD) that allows them to bind to methylated DNA.

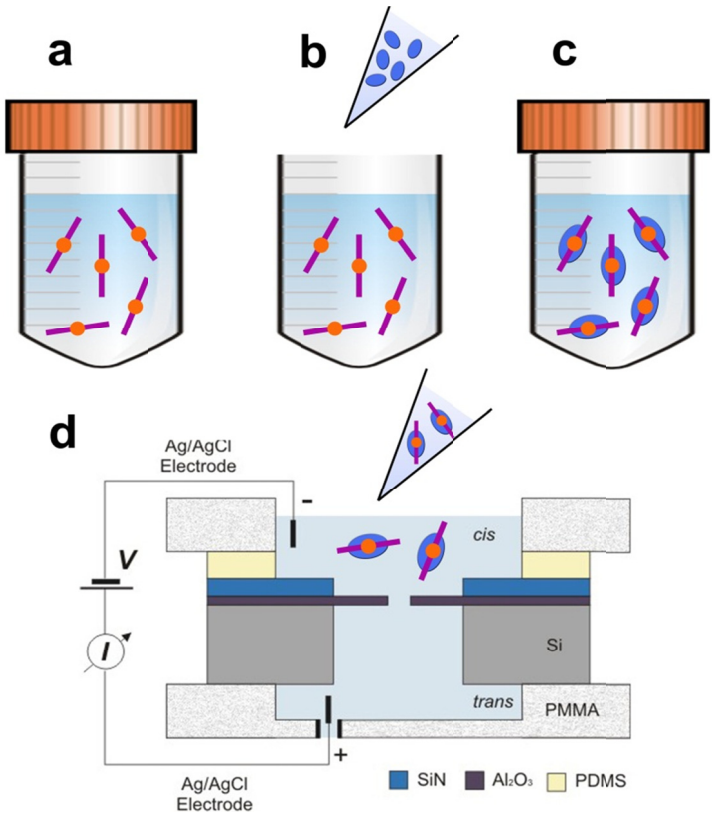

Figure 49 (a) Start with enzyme methylated DNA fragments. (b) Add MBD2 to methylated DNA samples. (c) 15 minute incubation step to form stable MBD2 bound DNA complexes. (d) Introduction of MBD2-DNA complex into the *cis* chamber of the nanopore fluidic setup.

MBD2 was selected for our preliminary work as it binds specifically and exclusively to a single methylated CpG dinucleotide in vitro,[215, 216] and has been identified as a critical component in transcriptional repression of the hypermethylated GSTP1 gene associated with prostate cancer.[217] MBD2 has two isoforms, the larger MBD2a (43.5 kDa) protein and the smaller MBD2b (29.1 kDa),[218] the latter of which shows a 10–100 fold affinity to methylated CpG nucleotides over unmethylated CpG dinucleotides.[219] Due to its high specificity, MBD2 proteins coupled to magnetic beads are frequently used in methylated DNA enrichment kits (EpiXplore by Clontech, MethylCollector Kit by Active Motif), to bind and separate methylated fragments from genomic DNA. We will use the specificity of MBD2 to label methylation sites along a methylated DNA molecule. A one hour incubation step in low salt concentration buffer is sufficient to bind these proteins to methylated DNA (figure 49c). The MBD2 protein we are

currently using has been expressed in bacteria by our collaborator (Nardulli lab at University of Illinois) and the binding of this protein to methylated DNA has been confirmed through gel shift assays.

The MBD2-DNA complex will next be introduced into the cis chamber of the nanopore fluidic setup as shown in figure 49d. Under an applied potential, these short, MBD2 bound, methylated DNA fragments will translocate through the pore resulting in characteristic current blockades, representative of the methylation status of the molecule.

Methylation Determination: We expect to be able to distinguish a single methylated DNA molecule from an unmethylated DNA fragment of equal length using nanopore based current spectroscopy methods (figure 50). The passage of unmethylated DNA through the pore will produce only a slight deviation in the baseline current as seen in figure 50a. A single, shallow blockade level is expected after removing all folded DNA translocation events.[25] The passage of an MBD2 bound DNA fragment through the pore, however, will result in a very different current signature (figure 50b). As the drop in pore current is related to the cross section of the translocating molecule, deeper blockades will be observed when the large, bound protein traverses the pore. Two distinct blockade levels are expected, the first corresponding to regions of DNA that do not contain bound proteins (I_{DNA}), and the second corresponding to regions containing the MBD2 bound protein (I_{MBD2}). Studies by Kowalczyk on RecA bound DNA through large ~30nm nanopores confirmed the detection of two distinct blockade levels corresponding to regions of RecA coated DNA and uncoated DNA.[220, 221] RecA has a molecular weight (~38 kDa) and cross sectional diameter (~7 nm) that is similar to MBD2. Thus, distinct current signatures from MBD2 bound DNA are expected relative to native DNA in ~15 nm Al_2O_3 nanopores.

The electrophoretic transport of MBD2 bound DNA molecules has been previously demonstrated using electrophoretic mobility shift assays and polyacrylamide gel electrophoresis.[216, 222] Interestingly, fragments with multiple bound MBD proteins corresponding to multiple methylated CpG dinucleotides migrated slower through the gel and could be resolved with single protein resolution.[216] Furthermore, each additional bound protein

significantly reduced the mobility of the complex in the gel. This was attributed to two factors; (1) the high molecular weight of MBD2 relative to the short DNA fragments, (2) the positive charge of MBD2 in pH 8.0 buffer (isoelectric point of 9.1).[219] Thus, under normal pore operating conditions (pH 7–8), MBD2 bound DNA translocation is expected. Free MBD2 translocation events are not expected as MBD2's positive charge will induce electrostatic repulsion at the pore when inserted into the *cis* chamber.

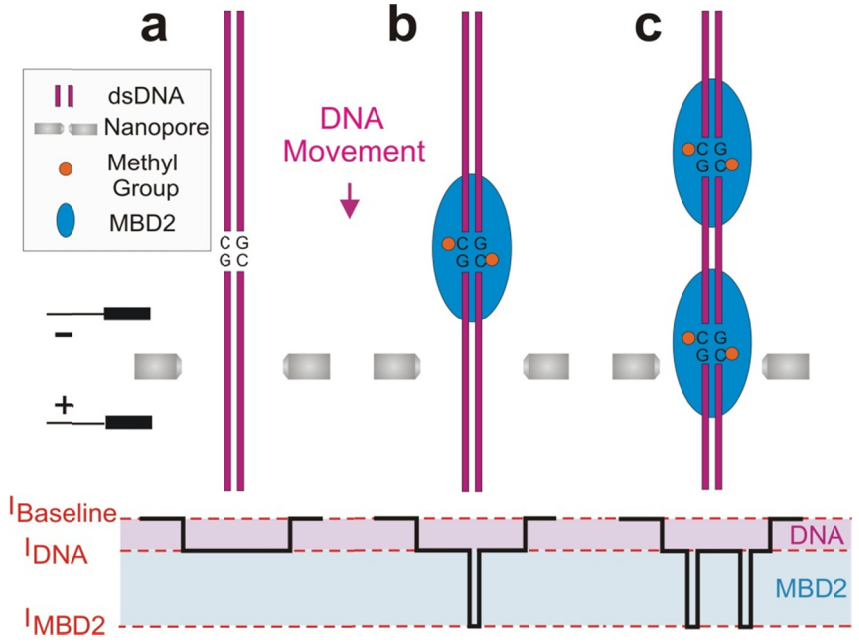

Figure 50 (a) Passage of unmethylated DNA; shallow current blockades are seen. (b) Passage of DNA with MBD2 bound to a single methylated CpG dinucleotide. Two blockade levels are seen: shallow blockade due to DNA, deep blockade due to MBD2. (c) Passage of DNA with multiple bound MBD2 proteins. Current signature permits methylation quantification and mapping of methylation sites along a single molecule.

Methylation Quantification and Mapping: Current spectroscopy should also allow us to map methylation sites along a specific DNA fragment and quantify its overall level of methylation. The process is illustrated in figure 50c. The presence of multiple fully methylated CpG dinucleotides along a single DNA molecule facilitates the binding of multiple MBD2 proteins per DNA, each of which produces a deep current blockade during translocation. The

translocation of fragments with multiple bound proteins will result in an electrical readout as shown in figure 50c that resembles the spatial distribution of proteins along that fragment. This can then be used to determine the distribution of methylated CpG dinucleotides along the interrogated DNA fragment. The current signature can also be used to quantify the extent of methylation based on the number of deep current blockades per event.

This raises the question as to what the spatial resolution of this technique is. DNase I footprinting confirmed that the MBD of MeCP2 protects a total of 12-14 nucleotides surrounding a single methylated CpG pair.[216] As the MBD of MeCP2 and MBD2 are homologous, we expect that MBD2 will cover approximately 12-14 bp of DNA upon binding also. Additional methyl CpG dinucleotides within this 12-14 bp domain are not available to bind to other MBD2 molecules, thereby limiting the spatial resolution of this technique.[216] Kowalczyk reported a spatial resolution of about 15 bp in RecA bound DNA translocation experiments through solid-state nanopores.[220] This is remarkable given that RecA carries a net negative charge[221] at pH 8.0. However, the net positive charge on MBD2 at pH 8.0 may help reduce the velocity of protein bound-DNA transport through the pore, translating to superior spatial resolution, perhaps exceeding that observed in RecA coated DNA experiments. We therefore expect to be able to resolve individual MBD2 molecules positioned along a single DNA strand with good resolution given the high signal-to-noise ratio of our nanopore platform.[30] The detection of individual bound MBD2 proteins in a nanopore is further supported by nanopore protein studies that detected individual BSA,[223] RecA,[221] and fibrinogen.[223] The length-wise topographic reading process reported here will allow us to quantify methylation levels and map methylation distributions along a single DNA fragment, and can be extended to the analysis of specific genes.

This highly sensitive nanopore based methylation analysis technique may prove very useful in medical diagnostics.

Conclusions 8

Solid-state nanopores offer immense potential as tools to replicate and understand the biophysics of single molecule transport through ion channels. We successfully demonstrated the development of a new solid-state, Al_2O_3 nanopore sensor with enhanced surface properties for the real-time, label-free detection and analysis of individual DNA molecules. The versatility of this technology allows for large scale VLSI integration promising reliable, affordable, mass producible single molecule sensors. Initial steps towards the development of hybrid nanopores, combining the stability and top down fabrication of solid-state technology with the chemical selectivity of biological nanopores, were also presented. Finally, the development of novel, highly versatile graphene-Al_2O_3 nanopores was presented. These platforms are highly robust, exhibit stable conductance values, show remarkable pH response and allow for the manipulation of ionic current through the nanopore by applying potentials to the graphene gate. Future studies will reveal whether the graphene gate could help slow down or trap a translocating DNA molecule in the pore, an exciting prospect that could help enable nanopore based DNA sequencing.

The application of this technology, however, extends well beyond DNA sequencing alone. Point-of-care diagnostic tests employing nanopore technology could be used to detect and monitor infectious diseases like influenza, making them effective tools in public health strategies. In defense, solid-state nanopores can be used for the rapid detection of high priority agents such as Bacillus anthracis (anthrax) at ultra-low concentrations. In drug screening, solid-state nanopores provide a means for label-free, real-time kinetic analysis of biomolecular interactions at the single molecule level including protein-protein, protein-DNA and receptor-ligand interactions. In medicine, nanopores could play an important role in diagnostics, risk assessment, disease monitoring, chemoprediction and patient prognosis. This technology may also serve as a base to provide further insight into the mechanisms driving biological processes, including cell signaling

and regulation using gated, selective ion channels, RNA translation using nuclear membrane pores, protein secretion across cellular membranes, and viral infection by phages. Needless to say, the future for nanopore technology is indeed very promising.

Appendix

Fabrication of Al_2O_3 Nanopores

The fabrication process starts with double-sided polished <100> silicon wafers from Silicon Quest International thinned down to a final thickness of 300±10μm. Wafers were piranha cleaned (1:1 H_2SO_4:H_2O_2) for 15 minutes prior to introduction into the ALD flow reactor (Cambridge NanoTech Inc) to remove organics and to promote the formation of reactive hydroxyl surface groups. The resulting interfacial SiO_2 layer also promotes film adhesion and helps achieve low leakage current through the dielectric film. ALD was used to deposit 700 Å of Al_2O_3 at an average deposition rate of 0.96 Å/cycle. Deposition of Al_2O_3 was done at a platen temperature of 300˚C using tetramethylaluminum (TMA) as the metal-precursor and water vapor as the oxygen precursor. One reaction cycle consisted of 0.05 s pulse of TMA, followed by 10 s evacuation of the reactor, 0.05 s pulse of water vapor followed by another 10 s reactor evacuation to remove gaseous byproducts, primarily CH_4 and any unreacted species. Water vapor supplied the oxygen forming Al-O-Al bonds while continually passivating the surface with Al-OH groups. Thermal annealing was next performed. During the low temperature anneal step, temperatures were ramped from 25˚C to 500˚C and film stress was monitored in-situ. Stress was reduced to 50 MPa at 500˚C but returned upon cooling to room temperature, suggesting that the inherent stress is likely due to mismatches in thermal expansion coefficients of the Al_2O_3 film and Si substrate. The mechanical stress of the deposited thin film was calculated using an optical film stress measurement tool (FSM 500TC) from Frontier Semiconductor.

Next, low stress silicon nitride was deposited (STS Mesc PECVD System) using a mixed frequency recipe consisting of alternating high frequency and low frequency deposition steps using process gases of SiH_4 and NH_3 at flow rates of 40 sccm and 55 sccm respectively at a platen temperature of 300˚C. High frequency (HF: 6 s at 13.56 MHz, platen power 20 W) and low frequency (LF: 2 s at 380 kHz, platen power 60 W) deposition steps resulted in stacked

tensile and compressively stressed layers. Process optimization resulted in the formation of 500 nm thick SiN films with a net tensile stress of < 80 MPa. Pattern transfer required the use of RIE (PlasmaLab) and this dry etch process was conducted at a power of 90 W and chamber pressure of 35 mT using CF_4 as the precursor at a flow rate of 60 sccm. An etch rate of 625 Å/min was characterized for this recipe. Next, backside lithography was used to pattern 30 x 30 μm square openings on the wafer backside, aligned with the openings on the front side using AZ9260 photoresist and a Quintel Q7000 IR Backside Mask Aligner. The patterned photoresist layer defined the mask for the following backside deep trench etch. Native oxide was removed from the backside of the device wafer using a short dry etch (1 min in RIE using CF_4) before mounting the wafer in the STS inductively coupled plasma deep reactive ion etching system (STS Mesc Multiplex Advanced Silicon Etcher). Deep silicon etching and polymer stripping were done for 12 s at a chamber pressure of 37 mT and platen power of 12 W with SF_6 and O_2 flow rates of 130 sccm and 13 sccm respectively per cycle. C_4F_8 sidewall passivation followed the etch step and was done at a chamber pressure of 18 mT for 8 s at a flow rate of 78 sccm. 495 such etch/passivation cycles were required to etch completely through the 300 μm thick Si handle layer and to stop on the 60 nm thick Al_2O_3 membrane layer. TEM sputtering was done using beam currents estimated between 10^8-10^9 e-nm^{-2}. The electron beam was focused to a 1.6 nm spot size in convergent beam diffraction mode and used to decompositionally sputter the Al_2O_3 membrane. Si_3N_4 pores were formed in commercially available DuraSiN^{TM} Si_3N_4 membranes from Protochips Inc.

Experimental Procedures

Post fabrication, nanopore chips were solvent cleaned with acetone/methanol/deionized water (Millipore 18.2 MΩ-cm) and treated with oxygen plasma for 1 minute at 90 W to remove any organic contaminants. Polydimethylsiloxane (PDMS) gaskets were bonded to each side of the chip to form gigaohm seals, thereby reducing fluidic leakage and improving electrical isolation between the reservoirs. A subsequent plasma treatment was done on the chip to enhance the hydrophilicity and wettability of the pore. The treated pores were immediately mounted between two chambers of a poly(methyl methacrylate) (PMMA) flow cell. The flow cell was designed to allow complete rinsing and interchange of the ionic solution in each reservoir without

dismantling the setup. 1 M KCl with 10 mM Tris-HCl buffering agent was introduced into both reservoirs and immediate wetting and ionic conduction through the pore was observed. The pH of the ionic solution was 7.5, adjusted using dilute KOH solution and aqueous H_2SO_4. The ionic solution was filtered using a 0.2 μm lure lock filter to remove any large particulate contamination. Current was measured by placing newly chlorided Ag/AgCl electrodes in each reservoir with the nanopore forming the only electrical/fluidic connection between the two compartments of the flow cell. The entire setup was housed in a double Faraday cage with a dedicated low noise ground connection mounted on a vibration isolation table. The current signal was measured using the Axopatch 200B low noise current amplifier (Axon Instruments, USA) operated in resistive feedback mode with $\beta = 1$. Data was low-pass filtered at 100 kHz (effective bandwidth of 70 kHz) using the built-in 8 pole Bessel filter. The output signal was sent to a Digidata 1440A data acquisition module (Axon Instruments, USA) and was digitized at 200 kHz and recorded using pClamp 10.2 software. Open pore current was recorded prior to the insertion of dsDNA. DNA translocation studies involved the use of 5 kbp dsDNA (NoLimits^{TM}) from Fermantas Inc. with dsDNA being inserted into the *cis* chamber at a final concentration of 6 nM.

Capacitance Measurements

The capacitance of Al_2O_3 membranes, $C_{mem,}$ was measured using two techniques. The first technique used a small signal AC voltage (5 mV, 1 kHz square wave) from a standard signal generator to measure the $R_{electrolyte}C_{mem}$ time constant of the membrane structure. The equivalent electrical circuit for the nanopore is shown in Figure 51(a). The electrolyte resistance (1M KCl) given the geometry of the PMMA flow cell was measured at 50 kΩ, in good agreement with geometric calculations. A membrane capacitance of 19 pF was extracted using this method. The typical membrane response to a square wave input is illustrated in Figure 51(b). The second method used an LCR meter (Agilent 4284A Precision LCR Meter, 20 Hz to 1 MHz) to measure the complex impedance of an Al_2O_3 nanopore as a function of frequency (Figure S.1(c)). The frequency was swept from 100 Hz to 100 kHz, corresponding to the bandwidth of interest in nanopore measurements. Fitting the simplified circuit model to the measured data, a membrane capacitance of 21 pF was extracted. C_{mem} was seen to dominate the complex impedance at high

frequencies as seen in the phase plot of Figure 51(c). The capacitances of all nanopore membrane structures measured were 20 ± 5 pF.

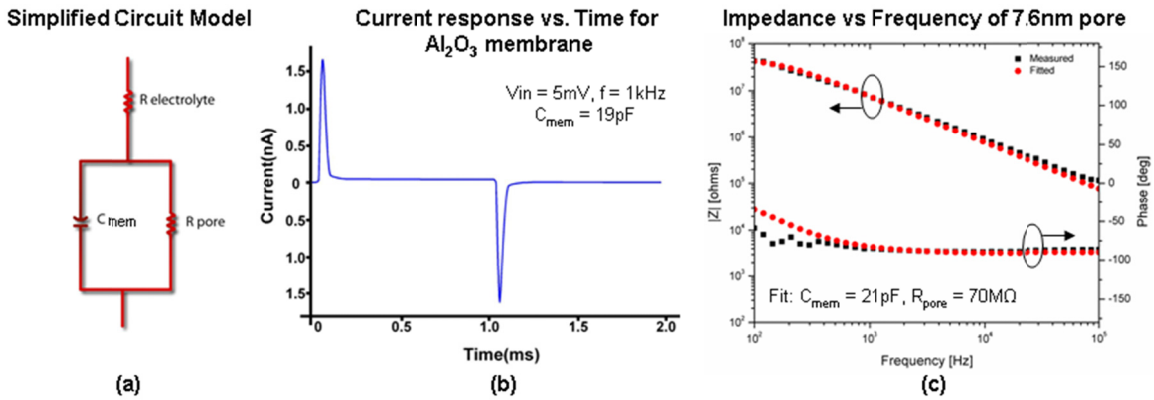

Figure 51 (a) Simplified circuit model of a nanopore. (b) Current response of an Al_2O_3 membrane to a square wave input (5 mV, 1 kHz). Fitted C_{mem} = 19 pF. (c) Complex impedance of a 7.6 nm Al_2O_3 nanopore as a function of frequency. At high frequencies (f >10 kHz), C_{mem} dominates impedance. C_{mem} = 21 pF using this method.

References

[1] P. D. Thomas, A. Kejariwal, *Proceedings of the National Academy of Sciences of the United States of America* **2004**, *101*, 15398.

[2] The International HapMap Consortium, *Nature* **2005**, *437*, 1299.

[3] E. R. Mardis, *Annual Review of Genomics & Human Genetics* **2008**, *9*, 387.

[4] M. L. Metzker, *Nature Reviews: Genetics* **2010**, *11*, 31.

[5] D. Branton, et al., *Nature Biotechnology* **2008**, *26*, 1146.

[6] X. S. Ling, B. Bready, A. Pertsinidis, *US Patent 2007 0190542*, **2007**.

[7] Y. Astier, O. Braha, H. Bayley, *Journal of the American Chemical Society* **2006**, *128*, 1705.

[8] J. Clarke, H. C. Wu, L. Jayasinghe, A. Patel, S. Reid, H. Bayley, *Nature Nanotechnology* **2009**, *4*, 265.

[9] S. L. Cockroft, J. Chu, M. Amorin, M. R. Ghadiri, *Journal of the American Chemical Society* **2008**, *130*, 818.

[10] F. Olasagasti, K. R. Lieberman, S. Benner, G. M. Cherf, J. M. Dahl, D. W. Deamer, M. Akeson, *Nature Nanotechnology* **2010**, *5*, 798.

[11] I. M. Derrington, T. Z. Butler, M. D. Collins, E. Manrao, M. Pavlenok, M. Niederweis, J. H. Gundlach, *Proceedings of the National Academy of Sciences of the United States of America* **2010**, *107*, 16060.

[12] B. McNally, A. Singer, Z. Yu, Y. Sun, Z. Weng, A. Meller, *Nano Letters* **2010**, *10*, 2237.

[13] A. P. Ivanov, E. Instuli, C. M. McGilvery, G. Baldwin, D. W. McComb, T. Albrecht, J. B. Edel, *Nano Letters* **2010**, *11*, 279.

[14] J. Lagerqvist, M. Zwolak, M. Di Ventra, *Nano Letters* **2006**, *6*, 779.

[15] J. B. Heng, A. Aksimentiev, C. Ho, V. Dimitrov, T. W. Sorsch, J. F. Miner, W. M. Mansfield, K. Schulten, G. Timp, *Bell Labs Technical Journal* **2005**, *10*, 5.

[16] M. E. Gracheva, A. Xiong, A. Aksimentiev, K. Schulten, G. Timp, J.-P. Leburton, *Nanotechnology* **2006**, *17*, 622.

[17] G. Sigalov, J. Comer, G. Timp, A. Aksimentiev, *Nano Letters* **2007**, *8*, 56.

[18] J. J. Kasianowicz, E. Brandin, D. Branton, D. W. Deamer, *Proceedings of the National Academy of Sciences of the United States of America* **1996**, *93*, 13770.

[19] M. Akeson, D. Branton, J. J. Kasianowicz, E. Brandin, D. W. Deamer, *Biophysical Journal* **1999**, *77*, 3227.

[20] A. Meller, L. Nivon, E. Brandin, J. Golovchenko, D. Branton, *Proceedings of the National Academy of Sciences of the United States of America* **2000**, *97*, 1079.

[21] S. Howorka, S. Cheley, H. Bayley, *Nature Biotechnology* **2001**, *19*, 636.

[22] M. Bates, M. Burns, A. Meller, *Biophysical Journal* **2003**, *84*, 2366.

[23] V. Borsenberger, N. Mitchell, S. Howorka, *Journal of the American Chemical Society* **2009**, *131*, 7530.

[24] J. Li, M. Gershow, D. Stein, E. Brandin, J. A. Golovchenko, *Nature Materials* **2003**, *2*, 611.

[25] P. Chen, J. Gu, E. Brandin, Y. R. Kim, Q. Wang, D. Branton, *Nano Letters* **2004**, *4*, 2293.

[26] A. J. Storm, J. H. Chen, H. W. Zandbergen, C. Dekker, *Physical Review E* **2005**, *71*, 051903.

[27] A. J. Storm, C. Storm, J. Chen, H. Zandbergen, J.-F. Joanny, C. Dekker, *Nano Letters* **2005**, *5*, 1193.

[28] D. Fologea, J. Uplinger, B. Thomas, D. S. McNabb, J. Li, *Nano Letters* **2005**, *5*, 1734.

[29] M. Wanunu, J. Sutin, B. McNally, A. Chow, A. Meller, *Biophysical Journal* **2008**, *95*, 4716.

[30] B. M. Venkatesan, B. Dorvel, S. Yemenicioglu, N. Watkins, I. Petrov, R. Bashir, *Advanced Materials* **2009**, *21*, 2771.

[31] B. M. Venkatesan, A. B. Shah, J. M. Zuo, R. Bashir, *Advanced Functional Materials* **2010**, *20*, 1266.

[32] Z. Chen, Y. Jiang, D. R. Dunphy, D. P. Adams, C. Hodges, N. Liu, N. Zhang, G. Xomeritakis, X. Jin, N. R. Aluru, S. J. Gaik, H. W. Hillhouse, C. Jeffrey Brinker, *Nature Materials* **2010**, *9*, 667.

[33] M. Wanunu, T. Dadosh, V. Ray, J. M. Jin, L. McReynolds, M. Drndic, *Nature Nanotechnology* **2010**, *5*, 807.

[34] M. Wanunu, W. Morrison, Y. Rabin, A. Y. Grosberg, A. Meller, *Nature Nanotechnology* **2010**, *5*, 160.

[35] P. W. Laird, *Nature Reviews: Cancer* **2003**, *3*, 253.

[36] P. M. Das, R. Singal, *Journal of Clinical Oncology* **2004**, *22*, 4632.

[37] P. W. Laird, R. Jaenisch, *Annual Review of Genetics* **1996**, *30*, 441.

[38] G. Strathdee, R. Brown, *Expert Reviews in Molecular Medicine* **2002**, *4*, 1.

[39] D. K. Vanaja, M. Ehrich, D. Van den Boom, J. C. Cheville, R. J. Karnes, D. J. Tindall, C. R. Cantor, C. Y. F. Young, *Cancer Investigation* **2009**, *27*, 549.

[40] C. Dekker, *Nature Nanotechnology* **2007**, *2*, 209.

[41] S. Bhakdi, J. Tranum-Jensen, *Microbiology and Molecular Biology Reviews* **1991**, *55*, 733.

[42] D. Jonas, I. Walev, T. Berger, M. Liebetrau, M. Palmer, S. Bhakdi, *Infection and Immunity* **1994**, *62*, 1304.

[43] S. Winters-Hilt, *BMC Bioinformatics* **2007**, *8*, S9.

[44] J. J. Kasianowicz, E. Brandin, D. Branton, D. W. Deamer, *Proceedings of the National Academy of Sciences of the United States of America* **1996**, *93*, 13770.

[45] A. Meller, L. Nivon, D. Branton, *Physical Review Letters* **2001**, *86*, 3435.

[46] J. Mathe, A. Aksimentiev, D. R. Nelson, K. Schulten, A. Meller, *Proceedings of the National Academy of Sciences of the United States of America* **2005**, *102*, 12377.

[47] A. Meller, D. Branton, *Electrophoresis* **2002**, *23*, 2583.

[48] J. Nakane, M. Akeson, A. Marziali, *Electrophoresis* **2002**, *23*, 2592.

[49] L. Brun, M. Pastoriza-Gallego, G. Oukhaled, J. Mathe, L. Bacri, L. Auvray, J. Pelta, *Physical Review Letters* **2008**, *100*.

[50] S. E. Henrickson, M. Misakian, B. Robertson, J. J. Kasianowicz, *Physical Review Letters* **2000**, *85*, 3057.

[51] W. Vercoutere, S. Winters-Hilt, H. Olsen, D. Deamer, D. Haussler, M. Akeson, *Nature Biotechnology* **2001**, *19*, 248.

[52] D. Stoddart, A. J. Heron, E. Mikhailova, G. Maglia, H. Bayley, *Proceedings of the National Academy of Sciences of the United States of America* **2009**, *106*, 7702.
[53] N. Mitchell, S. Howorka, *Angewandte Chemie International Edition* **2008**, *47*, 5565.

[54] D. Wendell, P. Jing, J. Geng, V. Subramaniam, T. J. Lee, C. Montemagno, P. Guo, *Nature Nanotechnology* **2009**, *4*, 765.

[55] Y. Xiang, M. C. Morais, A. J. Battisti, S. Grimes, P. J. Jardine, D. L. Anderson, M. G. Rossmann, *European Molecular Biology Organization Journal* **2006**, *25*, 5229.

[56] J. Li, D. Stein, C. McMullan, D. Branton, M. J. Aziz, J. A. Golovchenko, *Nature* **2001**, *412*, 166.

[57] I. G. Salisbury, R. S. Timsit, S. D. Berger, C. J. Humphreys, *Applied Physics Letters* **1984**, *45*, 1289.

[58] A. K. Geim, *Science* **2009**, *324*, 1530.

[59] S. Garaj, W. Hubbard, A. Reina, J. Kong, D. Branton, J. A. Golovchenko, *Nature* **2010**, *467*, 190.

[60] C. A. Merchant, K. Healy, M. Wanunu, V. Ray, N. Peterman, J. Bartel, M. D. Fischbein, K. Venta, Z. T. Luo, A. T. C. Johnson, M. Drndic, *Nano Letters* **2010**, *10*, 2915.

[61] G. G. F. Schneider, S. W. Kowalczyk, V. E. Calado, G. G. Pandraud, H. W. Zandbergen, L. M. K. Vandersypen, C. Dekker, *Nano Letters* **2010**, *10*, 3163.

[62] C. J. Lo, T. Aref, A. Bezryadin, *Nanotechnology* **2006**, *17*, 3264.

[63] S. Wu, S. R. Park, X. S. Ling, *Nano Letters* **2006**, *6*, 2571.

[64] M. Yu, H.-S. Kim, R. H. Blick, *Optics Express* **2009**, *17*, 10044.

[65] A. J. Storm, J. H. Chen, X. S. Ling, H. W. Zandbergen, C. Dekker, *Nature Materials* **2003**, *2*, 537.

[66] T. Schenkel, V. Radmilovic, E. A. Stach, S. J. Park, A. Persaud, *Journal of Vacuum Science & Technology B: Microelectronics and Nanometer Structures* **2003**, *21*, 2720.

[67] C. C. Harrell, Z. S. Siwy, C. R. Martin, *Small* **2006**, *2*, 194.

[68] Z. Siwy, E. Heins, C. C. Harrell, P. Kohli, C. R. Martin, *Journal of the American Chemical Society* **2004**, *126*, 10850.

[69] Z. Siwy, D. Dobrev, R. Neumann, C. Trautmann, K. Voss, *Applied Physics A: Materials Science & Processing* **2003**, *76*, 781.

[70] M. J. Kim, B. McNally, K. Murata, A. Meller, *Nanotechnology* **2007** *20*, 205302

[71] M. J. Kim, M. Wanunu, D. C. Bell, A. Meller, *Advanced Materials* **2006**, *18*, 3149.

[72] J. B. Heng, C. Ho, T. Kim, R. Timp, A. Aksimentiev, Y. V. Grinkova, S. Sligar, K. Schulten, G. Timp, *Biophysical Journal* **2004**, *87*, 2905.

[73] R. M. M. Smeets, U. F. Keyser, D. Krapf, M.-Y. Wu, N. H. Dekker, C. Dekker, *Nano Letters* **2006**, *6*, 89.

[74] R. E. Gyurcsányi, *TRAC Trends in Analytical Chemistry* **2008**, *27*, 627.

[75] J.-M. Moon, D. Akin, Y. Xuan, P. Ye, P. Guo, R. Bashir, *Biomedical Microdevices* **2009**, *11*, 135.

[76] L. Petrossian, S. J. Wilk, P. Joshi, S. Hihath, S. M. Goodnick, T. J. Thornton, *Microelectromechanical Systems, Journal of* **2007**, *16*, 1419.

[77] J.-M. Moon, D. Akin, Y. Xuan, P. Ye, P. Guo, R. Bashir, *Biomedical Microdevices* **2009**, *11*.

[78] M. Y. Wu, R. M. M. Smeets, M. Zandbergen, U. Ziese, D. Krapf, P. E. Batson, N. H. Dekker, C. Dekker, H. W. Zandbergen, *Nano Letters* **2009**, *9*, 479.

[79] Z. Siwy, A. Fulinski, *American Journal of Physics* **2004**, *72*, 567.

[80] Z. S. Siwy, *Advanced Functional Materials* **2006**, *16*, 735.

[81] C. Ho, R. Qiao, J. B. Heng, A. Chatterjee, R. J. Timp, N. R. Aluru, G. Timp, *Proceedings of the National Academy of Sciences of the United States of America* **2005**, *102*, 10445.

[82] S.-W. Nam, M. J. Rooks, K.-B. Kim, S. M. Rossnagel, *Nano Letters* **2009**, *9*, 2044.

[83] G. A. Parks, *Chemical Reviews* **2002**, *65*, 177.

[84] M. Wanunu, A. Meller, *Nano Letters* **2007**, *7*, 1580.

[85] E. B. Kalman, O. Sudre, Z. S. Siwy, *Biophysical Journal* **2009**, *96*, 648a.

[86] P. Chen, K. D. Gillis, *Biophysical Journal* **2000**, *79*, 2162.

[87] D. P. Hoogerheide, S. Garaj, J. A. Golovchenko, *Physical Review Letters* **2009**, *102*.

[88] R. M. M. Smeets, N. H. Dekker, C. Dekker, *Nanotechnology* **2009**, *20*, 095501.

[89] R. M. M. Smeets, U. F. Keyser, N. H. Dekker, C. Dekker, *Proceedings of the National Academy of Sciences of the United States of America* **2008**, *105*, 417.

[90] V. Tabard-Cossa, D. Trivedi, M. Wiggin, N. N. Jetha, A. Marziali, *Nanotechnology* **2007**, *18*, 305505.

[91] J. D. Uram, K. Ke, M. Mayer, *ACS Nano* **2008**, *2*, 857.

[92] M. S. Keshner, *Proceedings of the Institute of Electrical and Electronic Engineers* **1982**, *70*, 212.

[93] P. Chen, T. Mitsui, D. B. Farmer, J. Golovchenko, R. G. Gordon, D. Branton, *Nano Letters* **2004**, *4*, 1333.

[94] J. B. Heng, A. Aksimentiev, C. Ho, P. Marks, Y. V. Grinkova, S. Sligar, K. Schulten, G. Timp, *Biophysical Journal* **2006**, *90*, 1098.

[95] J. Comer, V. Dimitrov, Q. Zhao, G. Timp, A. Aksimentiev, *Biophysical Journal* **2009**, *96*, 593.

[96] H. Chang, F. Kosari, G. Andreadakis, M. A. Alam, G. Vasmatzis, R. Bashir, *Nano Letters* **2004**, *4*, 1551.

[97] S. Benner, R. J. A. Chen, N. A. Wilson, R. Abu-Shumays, N. Hurt, K. R. Lieberman, D. W. Deamer, W. B. Dunbar, M. Akeson, *Nature Nanotechnology* **2007**, *2*, 718.

[98] D. K. Lubensky, D. R. Nelson, *Biophysical Journal* **1999**, *77*, 1824.

[99] G. A. Calin, C. M. Croce, *Nature Reviews: Cancer* **2006**, *6*, 857.

[100] S. Volinia, G. A. Calin, C.-G. Liu, S. Ambs, A. Cimmino, F. Petrocca, R. Visone, M. Iorio, C. Roldo, M. Ferracin, R. L. Prueitt, N. Yanaihara, G. Lanza, A. Scarpa, A. Vecchione, M. Negrini, C. C. Harris, C. M. Croce, *Proceedings of the National Academy of Sciences of the United States of America* **2006**, *103*, 2257.

[101] W. H. Lee, W. B. Isaacs, G. S. Bova, W. G. Nelson, *Cancer Epidemiology Biomarkers and Prevention* **1997**, *6*, 443.

[102] U. Mirsaidov, W. Timp, X. Zou, V. Dimitrov, K. Schulten, A. P. Feinberg, G. Timp, *Biophysical Journal* **2009**, *96*, L32.

[103] M. Wanunu, D. Cohen-Karni, R. R. Johnson, L. Fields, J. Benner, N. Peterman, Y. Zheng, M. L. Klein, M. Drndic, *Journal of the American Chemical Society* **2010**, *133*, 486.

[104] D. Botstein, N. Risch, *Nature Genetics* **2003**, *33*, 228.

[105] Q. Zhao, G. Sigalov, V. Dimitrov, B. Dorvel, U. Mirsaidov, S. Sligar, A. Aksimentiev, G. Timp, *Nano Letters* **2007**, *7*, 1680.

[106] A. Singer, M. Wanunu, W. Morrison, H. Kuhn, M. Frank-Kamenetskii, A. Meller, *Nano Letters* **2010**, *10*, 738.

[107] K. B. Jirage, J. C. Hulteen, C. R. Martin, *Science* **1997**, *278*, 655.

[108] K.-Y. Chun, P. Stroeve, *Langmuir* **2002**, *18*, 4653.

[109] K. B. Jirage, J. C. Hulteen, C. R. Martin, *Analytical Chemistry* **1999**, *71*, 4913.

[110] S. B. Lee, D. T. Mitchell, L. Trofin, T. K. Nevanen, H. Soderlund, C. R. Martin, *Science* **2002**, *296*, 2198.

[111] T. Jovanovic-Talisman, J. Tetenbaum-Novatt, A. S. McKenney, A. Zilman, R. Peters, M. P. Rout, B. T. Chait, *Nature* **2009**, *457*, 1023.

[112] R. Peters, *Traffic* **2005**, *6*, 421.

[113] P. Kohli, C. C. Harrell, Z. Cao, R. Gasparac, W. Tan, C. R. Martin, *Science* **2004**, *305*, 984.

[114] J. C. Love, L. A. Estroff, J. K. Kriebel, R. G. Nuzzo, G. M. Whitesides, *Chemical Reviews* **2005**, *105*, 1103.

[115] J. Nilsson, J. R. I. Lee, T. V. Ratto, S. E. Létant, *Advanced Materials* **2006**, *18*, 427.

[116] M. Y. Wu, D. Krapf, M. Zandbergen, H. W. Zandbergen, P. E. Batson, *Applied Physics Letters* **2005**, *87*, 113106.

[117] G. Jagerszki, R. E. Gyurcsanyi, L. Hofler, E. Pretsch, *Nano Letters* **2007**, *7*, 1609.

[118] L. Höfler, Róbert E. Gyurcsányi, *Electroanalysis* **2008**, *20*, 301.

[119] Y. R. Kim, J. Min, I. H. Lee, S. Kim, A. G. Kim, K. Kim, K. Namkoong, C. Ko, *Biosensors and Bioelectronics* **2007**, *22*, 2926.

[120] Z. Siwy, S. Howorka, *Chemical Society Reviews* **2009**, *39*, 1115.

[121] S. M. Iqbal, D. Akin, R. Bashir, *Nature Nanotechnology* **2007**, *2*, 243.

[122] E. C. Yusko, J. M. Johnson, S. Majd, P. Prangkio, R. C. Rollings, J. Li, J. Yang, M. Mayer, *Nature Nanotechnology* **2011**, *6*, 253.

[123] B. M. Venkatesan, J. Polans, J. Comer, S. Sridhar, D. Wendell, A. Aksimentiev, R. Bashir, *Biomedical Microdevices* **2011**, in press.

[124] A. R. Hall, A. Scott, D. Rotem, K. K. Mehta, H. Bayley, C. Dekker, *Nature Nanotechnology* **2010**, *5*, 874.

[125] J. T. Fitch, C. H. Bjorkman, G. Lucovsky, F. H. Pollak, X. Yin, *Journal of Vacuum Science & Technology B* **1989**, *7*, 775.

[126] W.-K. Kim, W.-H. Nam, S.-H. Kim, S.-W. Rhee, *Journal of Chemical Engineering of Japan* **2005**, *38*, 578.

[127] S. Jensen, A. D. Yalcinkaya, S. Jacobsen, T. Rasmussen, F. E. Rasmussen, O. Hansen, *Physica Scripta* **2004**, *T114*, 188.

[128] K. R. Williams, R. S. Muller, *Journal of Microelectromechanical Systems* **1996**, *5*, 256.

[129] A. J. Storm, J. H. Chen, X. S. Ling, H. W. Zandbergen, C. Dekker, *Nature Materials* **2003**, *2*, 537.

[130] G. Krautheim, T. Hecht, S. Jakschik, U. Schröder, W. Zahn, *Applied Surface Science* **2005**, *252*, 200.

[131] H. Fischer, M. Hemelik, R. Telle, R. Marx, *Dental Materials* **2005**, *21*, 671.

[132] R. Katamreddy, R. Inman, G. Jursich, A. Soulet, A. Nicholls, C. Takoudis, *Thin Solid Films* **2007**, *515*, 6931.

[133] S. D. Berger, I. G. Salisbury, R. H. Milne, D. Imeson, C. J. Humphreys, *Philosophical Magazine Part B* **1987**, *55*, 341

[134] J. E. Bonevich, L. D. Marks, *Ultramicroscopy* **1991**, *35*, 161.

[135] M. Kundu, N. Miyata, M. Ichikawa, *Applied Physics Letters* **2001**, *79*, 842.

[136] O. Zywitzki, K. Goedicke, H. Morgner, *Surface and Coatings Technology* **2002**, *151-152*, 14.

[137] D. R. G. Mitchell, X. Wang, R. A. Caruso, *Micron* **2008**, *39*, 344.

[138] J. C. Pivin, *Journal of Materials Science* **1983**, *18*, 1267.

[139] A. J. Bourdillon, S. M. El-mashri, A. J. Forty, *Philosophical Magazine A* **1984**, *49*, 341

[140] D. Bouchet, C. Colliex, *Ultramicroscopy* **2003**, *96*, 139.

[141] I. Stará, D. Zeze, V. Matolín, J. Pavluch, B. Gruzza, *Applied Surface Science* **1997**, *115*, 46.

[142] R. F. Egerton, *Electron Energy-Loss Spectroscopy in the Electron Microscope*, Plenum Press, New York, **1996**.

[143] G. S. Chen, C. B. Boothroyd, C. J. Humphreys, *Philosophical Magazine A* **1998**, *78*, 491.

[144] M. S. M. Saifullah, K. Kurihara, C. J. Humphreys, *Journal of Vacuum Science & Technology B: Microelectronics and Nanometer Structures* **2000**, *18*, 2737.

[145] M. E. Mochel, C. J. Humphreys, J. A. Eades, J. M. Mochel, A. M. Petford, *Applied Physics Letters* **1983**, *42*, 392.

[146] D. K. N. Lubensky, D. R. , *Biophysical Journal* **1999**, *77*, 1824

[147] M. Wanunu, J. Sutin, B. McNally, A. Chow, A. Meller, *Biophysical Journal* **2008**, biophysj.108.140475.

[148] A. M. Berezhkovskii, I. V. Gopich, *Biophysical Journal* **2003**, *84*, 787.

[149] C. T. A. Wong, M. Muthukumar, *The Journal of Chemical Physics* **2007**, *126*, 164903.

[150] S. Alami-Younssi, A. Larbot, M. Persin, J. Sarrazin, L. Cot, *Journal of Membrane Science* **1995**, *102*, 123.

[151] S. Veeramasuneni, M. R. Yalamanchili, J. D. Miller, *Journal of Colloid and Interface Science* **1996**, *184*, 594.

[152] P. Bowen, C. Carry, D. Luxembourg, H. Hofmann, *Powder Technology* **2005**, *157*, 100.

[153] G. V. Franks, L. Meagher, *Colloids and Surfaces A: Physicochemical and Engineering Aspects* **2003**, *214*, 99.

[154] D. Kejian, S. Weimin, Z. Haiyan, P. Xianglei, H. Honggang, *Applied Physics Letters* **2009**, *94*, 014101.

[155] A. Aksimentiev, J. B. Heng, G. Timp, K. Schulten, *Biophysical Journal* **2004**, *87*, 2086.

[156] S. W. Lee, H. Shang, R. T. Haasch, V. Petrova, G. U. Lee, *Nanotechnology* **2005**, *16*, 1335.

[157] S. Penumetcha, R. Kona, J. Hardin, A. Molder, E. Steinle, *Sensors* **2007**, *7*, 2942.

[158] V. Szczepanski, I. Vlassiouk, S. Smirnov, *Journal of Membrane Science* **2006**, *281*, 587.

[159] I. Vlassiouk, P. Takmakov, S. Smirnov, *Langmuir* **2005**, *21*, 4776.

[160] I. Vlassiouk, A. Krasnoslobodtsev, S. Smirnov, M. Germann, *Langmuir* **2004**, *20*, 9913.

[161] J. Drews, *Science* **2000**, *287*, 1960.

[162] E. Castellana, P. Cremer, *Surface Science Reports* **2006**, *61*, 429.

[163] B. W. Koenig, S. Krueger, W. J. Orts, C. F. Majkrzak, N. F. Berk, J. V. Silverton, K. Gawrisch, *Langmuir* **1996**, *12*, 1343.

[164] E. Sackmann, *Science* **1996**, *271*, 43.

[165] J. M. Solletti, M. Botreau, F. Sommer, W. L. Brunat, S. Kasas, T. M. Duc, M. R. Celio, *Langmuir* **1996**, *12*, 5379.

[166] P. S. Cremer, S. G. Boxer, *The Journal of Physical Chemistry B* **1999**, *103*, 2554.

[167] E. Reimhult, F. Hook, B. Kasemo, *Langmuir* **2003**, *19*, 1681.

[168] T. Cha, A. Guo, X. Y. Zhu, *Biophysical Journal* **2006**, *90*, 1270.

[169] E. Reimhult, F. Hook, B. Kasemo, *Journal of Chemical Physics* **2002**, *117*, 7401.

[170] J. T. Groves, N. Ulman, P. S. Cremer, S. G. Boxer, *Langmuir* **1998**, *14*, 3347.

[171] M. D. Mager, B. Almquist, N. A. Melosh, *Langmuir* **2008**, *24*, 12734.

[172] P. Nollert, H. Kiefer, F. Jahnig, *Biophysical Journal* **1995**, *69*, 1447.

[173] R. F. Roskamp, I. K. Vockenroth, N. Eisenmenger, J. Braunagel, I. Koper, *Chemphyschem* **2008**, *9*, 1920.

[174] J. Drexler, C. Steinem, *Journal of Physical Chemistry B* **2003**, *107*, 11245.

[175] A. Berquand, P. E. Mazeran, J. Pantigny, V. Proux-Delrouyre, J. M. Laval, C. Bourdillon, *Langmuir* **2003**, *19*, 1700.

[176] H. G. Kapitza, G. Mcgregor, K. A. Jacobson, *Proceedings of the National Academy of Sciences of the United States of America* **1985**, *82*, 4122.

[177] J. C. Phillips, R. Braun, W. Wang, J. Gumbart, E. Tajkhorshid, E. Villa, C. Chipot, R. D. Skeel, L. Kalé, K. Schulten, *Journal of Computational Chemistry* **2005**, *26*, 1781.

[178] P. F. Batcho, D. A. Case, T. Schlick, *The Journal of Chemical Physics* **2001**, *115*, 4003.

[179] S. Miyamoto, P. A. Kollman, *Journal of Computational Chemistry* **1992**, *13*, 952.

[180] H. C. Andersen, *Journal of Computational Physics* **1983**, *52*, 24.

[181] A. D. MacKerell, D. Bashford, M. Bellott, R. L. Dunbrack, J. D. Evanseck, M. J. Field, S. Fischer, J. Gao, H. Guo, S. Ha, D. Joseph-McCarthy, L. Kuchnir, K. Kuczera, F. T. K. Lau, C. Mattos, S. Michnick, T. Ngo, D. T. Nguyen, B. Prodhom, W. E. Reiher, B. Roux, M. Schlenkrich, J. C. Smith, R. Stote, J. Straub, M. Watanabe, J. Wiorkiewicz-Kuczera, D. Yin, M. Karplus, *The Journal of Physical Chemistry B* **1998**, *102*, 3586.

[182] E. R. Cruz-Chu, A. Aksimentiev, K. Schulten, *The Journal of Physical Chemistry B* **2006**, *110*, 21497.

[183] G. J. Martyna, D. J. Tobias, M. L. Klein, *The Journal of Physical Chemistry* **1994**, *101*, 4177.

[184] S. W. I. Siu, R. Vacha, P. Jungwirth, R. A. Bockmann, *The Journal of Chemical Physics* **2008**, *128*, 125103.

[185] D. Axelrod, D. E. Koppel, J. Schlessinger, E. Elson, W. W. Webb, *Biophysical Journal* **1976**, *16*, 1055.

[186] R. Richter, A. Mukhopadhyay, A. Brisson, *Biophysical Journal* **2003**, *85*, 3035.

[187] G. Csucs, J. J. Ramsden, *Biochimica Et Biophysica Acta-Biomembranes* **1998**, *1369*, 61.

[188] T. E. Starr, N. L. Thompson, *Langmuir* **2000**, *16*, 10301.

[189] S. Kumar, J. H. Hoh, *Langmuir* **2000**, *16*, 9936.

[190] C. Kataoka-Hamai, H. Inoue, Y. Miyahara, *Langmuir* **2008**, *24*, 9916.

[191] H. C. Gaede, K. M. Luckett, I. V. Polozov, K. Gawrisch, *Langmuir* **2004**, *20*, 7711.

[192] X. J. Han, A. Studer, H. Sehr, I. Geissbuhler, M. Di Berardino, F. K. Winkler, L. X. Tiefenauer, *Advanced Materials* **2007**, *19*, 4466.

[193] W. Romer, C. Steinem, *Biophysical Journal* **2004**, *86*, 955.

[194] M. Stelzle, G. Weissmuller, E. Sackmann, *Journal of Physical Chemistry* **1993**, *97*, 2974.

[195] X. Li, W. Cai, J. An, S. Kim, J. Nah, D. Yang, R. Piner, A. Velamakanni, I. Jung, E. Tutuc, S. K. Banerjee, L. Colombo, R. S. Ruoff, *Science* **2009**, *324*, 1312.

[196] J. A. Abels, F. Moreno-Herrero, T. van der Heijden, C. Dekker, N. H. Dekker, *Biophysical Journal* **2005**, *88*, 2737.

[197] J. R. Schultz-Norton, Y. S. Ziegler, A. M. Nardulli, *Trends in Endocrinology & Metabolism* **2011**, *22*, 124.
[198] P. K. Ang, W. Chen, A. T. S. Wee, K. P. Loh, *Journal of the American Chemical Society* **2008**, *130*, 14392.

[199] K. Lee, J.-H. Kwon, S.-l. Moon, W.-S. Cho, B.-K. Ju, Y.-H. Lee, *Materials Letters* **2007**, *61*, 3201.

[200] Y. Ohno, K. Maehashi, Y. Yamashiro, K. Matsumoto, *Nano Letters* **2009**, *9*, 3318.

[201] D. Stein, M. Kruithof, C. Dekker, *Physical Review Letters* **2004**, *93*, 035901.

[202] R. Karnik, R. Fan, M. Yue, D. Li, P. Yang, A. Majumdar, *Nano Letters* **2005**, *5*, 943.

[203] Y. W. Chen, M. Liu, T. Kaneko, P. C. McIntyre, *Electrochemical and Solid-State Letters*, *13*, G29.

[204] S. M. George, *Chemical Reviews* **2009**, *110*, 111.

[205] S. Chen, J. G. Bomer, E. T. Carlen, A. van den Berg, *Nano Letters* **2011**, *11*, 2334.

[206] A. Murrell, V. K. Rakyan, S. Beck, *Human Molecular Genetics* **2005**, *14*, R3.

[207] W. B. Coleman, A. G. Rivenbark, *Journal of Molecular Diagnostics* **2006**, *8*, 152.

[208] C. Grunau, S. J. Clark, A. Rosenthal, *Nucleic Acids Research* **2001**, *29*, e65.

[209] B. N. Trinh, T. I. Long, P. W. Laird, *Methods* **2001**, *25*, 456.

[210] M. Campan, D. J. Weisenberger, B. Trinh, P. W. Laird, in *DNA Methylation*, **2009**, 325.

[211] C. A. Eads, K. D. Danenberg, K. Kawakami, L. B. Saltz, C. Blake, D. Shibata, P. V. Danenberg, P. W. Laird, *Nucleic Acids Research* **2000**, *28*, e32.

[212] Y. Ando, Y. Hayashizaki, *Nature Protocols* **2006**, *1*, 2774.

[213] E. A. Moskalyov, A. T. Eprintsev, J. D. Hoheisel, *Molecular Biology* **2007**, *41*, 723.

[214] P. S. Yan, M. R. Perry, D. E. Laux, A. L. Asare, C. W. Caldwell, T. H. M. Huang, *Clinical Cancer Research* **2000**, *6*, 1432.

[215] H. F. Jørgensen, A. Bird, *Mental Retardation and Developmental Disabilities Research Reviews* **2002**, *8*, 87.

[216] X. Nan, R. R. Meehan, A. Bird, *Nucleic Acids Research* **1993**, *21*, 4886.

[217] M. Nakayama, M. L. Gonzalgo, S. Yegnasubramanian, X. H. Lin, A. M. De Marzo, W. G. Nelson, *Journal of Cellular Biochemistry* **2004**, *91*, 540.

[218] E. Ballestar, A. P. Wolffe, *European Journal of Biochemistry* **2001**, *268*, 1.

[219] A. P. Wolffe, P. L. Jones, P. A. Wade, *Proceedings of the National Academy of Sciences of the United States of America* **1999**, *96*, 5894.

[220] S. W. Kowalczyk, A. R. Hall, C. Dekker, *Nano Letters* **2009**, *10*, 324.

[221] R. M. M. Smeets, S. W. Kowalczyk, A. R. Hall, N. H. Dekker, C. Dekker, *Nano Letters* **2008**.

[222] K.-i. Tatematsu, T. Yamazaki, F. Ishikawa, *Genes to Cells* **2000**, *5*, 677.

[223] D. Fologea, B. Ledden, D. S. McNabb, J. L. Li, *Applied Physics Letters* **2007**, *91*.